Turbulent Transport in Complex, Alpine Environments

THÈSE N^{O} 6594 (2015)

PRÉSENTÉE LE 1ER MAI JANVIER 2015

À LA FACULTÉ DE L'ENVIRONNEMENT NATUREL, ARCHITECTURAL ET CONSTRUIT
LABORATOIRE DE MÉCANIQUE DES FLUIDES DE L'ENVIRONNEMENT
PROGRAMME DOCTORAL EN GÉNIE CIVIL ET ENVIRONNEMENT

ÉCOLE POLYTECHNIQUE FÉDÉRALE DE LAUSANNE

POUR L'OBTENTION DU GRADE DE DOCTEUR ÈS SCIENCES

PAR

Holly Jayne OLDROYD

acceptée sur proposition du jury:

Prof. S. Takahama, président du jury
Prof. M. Parlange, directeur de thèse
Prof. E. Pardyjak, rapporteur
Prof. C. Higgins, rapporteur
Prof. F. Gallaire, rapporteur

ÉCOLE POLYTECHNIQUE
FÉDÉRALE DE LAUSANNE

Suisse
2015

Katabatic $_{adj}$. /ka-tə-'ba-tik/ descending.
—Greek: *katabatos*, derived from
$\kappa\alpha\tau\varepsilon\beta\acute{\alpha}\nu\omega$ or *katabainein*
bainein: to go +
kata: down

To Mom

Acknowledgements

katabatic shares an etymological root with *katabasis*, which in literary and mythological texts refers to human's *descent* into hell and return to Earth. Some may say this is an apt description of a PhD. Others may say a PhD makes you into an expert on a small bit of a particular topic that most people don't care about. Still, others might say a PhD is the 'best time of your life' or that doing a PhD just makes you less sensitive (less of a sissy). In my experience, perhaps all of these hold a bit of truth to one degree or another, and I think I am definitely less of a sissy. However, I would say that doing a PhD introduced me to a lifetime's worth of fascinating questions about the world around us, and allowed me get my toes wet before jumping into the sea. There are many who have helped me to accomplish this work and to shape this experience. You are too many to name, and I wish I could thank you all, personally.

First, I would like to acknowledge my thesis jury: Satoshi Takahama, Marc B. Parlange, Eric R. Pardyjak, Chad W. Higgins, and François Gallaire and thank them for participating in a very important day for me. I know that some of you have made pretty big sacrifices to participate, so know this is greatly appreciated. Second, I would like to thank my supervisor, Marc Parlange, for allowing me such a wonderful opportunity to come to Lausanne and work with the EFLUM lab. Marc has shown me a great deal of trust, generosity and independence to explore my personal scientific interest. He has also taught me much about life as well as hydrology and meteorology, and has introduced me with compliments to many of the leading scientists in the field. Thank you, Marc. I am forever indebted.

Marc has also created an amazing atmosphere in the EFLUM lab, full of teamwork, laughs, sports, the opportunity and resources to do ground-breaking fieldwork, and the chance to collaborate with incredible visiting professors, who I would also like to acknowledge for their interest, time and insights into my work: Wilfried Brutsaert, John Selker, Gaby Katul, Charles Meneveau, and Andreas Christen. Many many thanks to the EFLUM lab members who have been a pleasure to see everyday over the past four years and who have helped me in so many ways with fieldwork, proofing drafts, and scientific chats. Special thanks to Raphaël Mutzner who was with me from day one to the end, and who helped extensively in the field (especially to communicate with the farmers). Particular field work thanks also go to Marc Diebold and Marc Calaf, who offered great collaborations on field campaigns and who agreed to climb the 10 m tower so that I would not have to die, and to Elena Gianelli who I had the pleasure to help advise during her MS work here and who was, by far, the most enthusiastic fieldworker

(she even carried car batteries up the slope at the end of the day even though she was the smallest person there). Special thanks also to Hendrik Huwald, Chad Higgins and Daniel Nadeau who really helped me to hit the ground running in my first 6 months here. Thanks to Francesco Ciocca for being a great office mate and one of the first people in Switzerland who I considered to be a friend. To Marie-Jo Pellaud and Natalie Ceperley whose help with Switzerland and EPFL really saved me on several occasions. To Michi Lehning, Jessica Ferrante Ritzi, Batrice Raball and the CRYOS lab group who help us maintain the lab environment in the waning days of EFLUM. Thanks also to Chad Higgins, Marc Calaf, Nikki Vercauteren, Marco Giometto and Varun Sharma for the many chats we've had about our respective work. These chats really helped me to shape my own ideas and I learned something new every time. They were invaluable to me and I hope they continue.

Prior to my time here, many others have been important examples and mentors in my life and I don't think I would have made it here without them. To my many k-12 teachers who never told me that I should not like math and science, and especially to Mrs. Draper and Mrs, Turley who spent the extra time to prepare the 'hard math' homework for me in elementary school. To my many sports coaches who kept me out of trouble in my younger days. To Joe Klewicki for his enthusiasm in my Intro to Fluids course; that was the first time in my undergrad that I felt intrinsically motivated to study. To Eric Pardyjak for his guidance, mentorship, enthusiasm and especially confidence in me over the many years. He is also responsible for convincing me that I am 'absolutely grad-school material', and subsequently for saving me from staring at the same spreadsheet for 30 years in an industry job.

On a more personal note, my deepest gratitude to my family and friends from home and from Switzerland. Your friendship, love and support during these four years was essential to my successes, happiness and personal growth. Thank you for all of the great memories, as well. To my brothers, David, Jonathan, and Matthew for setting the bar high so that I would have to jump even higher to out-do them, and to my father Thomas Oldroyd for being my loudest cheerleader. To my grandmother, Elsie Macbeth, for encouraging me to go and find my Swiss roots. Finally, to my mother Jaylynn Macbeth Oldroyd, thank you for the extreme support you gave me in my formative years, especially in terms of education. I love and miss you dearly.

One of my most vivid childhood memories is of my mom wrapping me in a blanket and putting me on her lap to watch the thunderstorms from the front porch when I was too frightened to sleep. In recollection, these were my first observations of atmospheric phenomenon. From these and many more experiences together, my mother influenced me to find delight, wonder, imagination, awe and appreciation for natural world.

Lausanne, April 2015 H. J. O.

Abstract

Turbulent exchanges between the atmosphere and the underlying surface transport heat, moisture, momentum and pollutants, and thus understanding them is crucial to water resource management, meteorological predictions, climate modeling, wind energy production and pollution transport modeling and mitigation. The majority of established theories and techniques used to model, predict and observe turbulent exchange assume the underlying surface is flat, uniform and homogeneous. Consequently, in mountainous regions, turbulent exchanges are difficult to model and predict because they are intrinsically linked to the underlying surface conditions and complexity. Few observational studies have focused on the vertical structure of turbulent fluxes over mountainous terrain due to practical challenges. In sum, researchers and practitioners urgently need better theories and techniques to study and model turbulent exchange in alpine environments.

In this dissertation, we analyze turbulent exchange measured over a steep, alpine slope in Switzerland to make quantitative comparisons with standard flat-terrain 'laws' and practices and develop new theories and techniques adapted to mountainous terrain. First, flux-profile relations derived from Monin-Obukhov similarity theory are widely used in a variety of models to relate the surface conditions to atmospheric variables. We show that for katabatic flow, or thermally-driven air drainage that often occurs at night over sloping terrain, these relations break down because they do not account for the strong vertical gradients in the observed turbulent fluxes. However, the measurements exhibit clear functionalities that we use to derive new, empirical flux-profile relations for katabatic flow. Our functions indicate increased turbulent mixing compared to the flat-terrain relations. Misalignment between gravity and the inclined surface helps explain these functional differences because it reduces (and even reverses over steep slopes) the typical nighttime buoyant suppression of turbulent kinetic energy, which acts vertically via gravity. We also revise the governing flow equations to properly account for this misalignment. Second, standard data treatment techniques, such as sensor tilt corrections, do not hold true over complex topography. We develop an *optimized* sector-wise planar fit (SPF) tilt correction to best select the SPF input parameters for any complex site, and quantify the resulting sensitivities in the momentum fluxes. Finally, we present a mechanistic study that combines measurements and the one-dimensional momentum balance. Results show that frictional and buoyant mechanisms dominate, but that drag forces from the alpine grass canopy and the modeled outer-layer pressure (for conditions with low wind speeds)

are also significant. In summary, this one-dimensional model or the newly developed flux-profile relations could replace inappropriate, flat-terrain wall models in larger-scale numerical models to improve atmospheric predictions for katabatic flow regimes. Additionally, terrain-appropriate sensor tilt corrections and proper alignment of buoyant forces improve turbulent flux estimates for complex and steep topography, and hence have ramifications for similarity or budget analyses that require accurate quantification of turbulent exchange.

Key words: Mountain meteorology · Turbulent exchange · Complex topography · Katabatic flow · Sensor tilt corrections · Tilted coordinate systems · 1D momentum balance · Monin-Obukhov similarity theory · Flux-gradient relations · Turbulence kinetic energy

Résumé

La compréhension de la dynamique des échanges de flux turbulents entre l'atmosphère et les transports de surface (chaleur, humidité, polluants) est cruciale pour une meilleure gestion des ressources en eau, pour les prévisions météorologiques, la modélisation climatique, la production de l'énergie éolienne, la modélisation et la réduction du transport des polluants. La majorité des théories établies et les techniques utilisées pour modéliser, prévoir et observer les échanges de flux turbulent considèrent la surface de terrain comme étant plate, uniforme et homogène. Par conséquent, dans les régions montagneuses, les échanges turbulents sont difficiles à modéliser et à prévoir parce qu'ils sont intrinsèquement liés aux conditions de surface complexes. Très peu d'études ont mis l'accent sur la structure verticale des flux turbulents en terrain montagneux en raison de difficultés pratiques. En résumé, les chercheurs et les utilisteurs sont en quête urgente de théories et techniques pour étudier et modéliser les échanges de flux turbulent dans les environnements alpins.

Dans cette thèse, nous avons analysé l'échange de flux turbulent mesuré sur une pente raide d'une région alpine en Suisse dans l'optique de faire des comparaisons quantitatives avec les méthodes standards sur terrain plat afin de développer de nouvelles théories et techniques adaptées aux terrains montagneux. Premièrement les relations de flux-profil, calculées à partir de la théorie de similarité de Monin-Obukhov, sont largement utilisées dans une variété de modèles afin de faire le lien entre les conditions de surface et les variables atmosphériques. Nous montrons que pour les vents catabatiques, dûs à un drainage d'air d'origine thermique qui se produit souvent la nuit sur un terrain en pente, ces relations ne sont plus valables car ils ne représente que les forts gradients verticaux dans les flux turbulents observés. Toutefois, les mesures présentent des caractéristiques physiques claires que nous avons utilisées pour déterminer de nouvelles relations empiriques de flux-profil pour les vents catabatiques. Ces nouvelles fonctions montrent une augmentation du mélange turbulent en comparaison aux résultats obtenus avec les modèles classiques sur terrain plat. Le désalignement entre la gravité et la surface inclinée permet d'expliquer ces différences puisque ceci réduit (ou, sur les pentes raides, inverse) la suppression de l'énergie cinétique turbulente flottable nocturne qui agit verticalement par gravité. Nous avons également étudié les équations gouvernant les écoulements pour intégrer les désalignements en terrain raides. Deuxièmement, les techniques standards de traitement de données, telles que les corrections du tilt des capteurs, ne sont pas adaptées pour les topographies complexes. Nous avons développé une méthode d'optimisation par secteur de régression surfaciale (SPF) intégrant l'inclinaison du terrain pour une

meilleure sélection des paramètres d'entrée du SPF pour tout site complexe, et afin de quantifier les sensibilités du moment de flux. Pour finir, nous présentons une étude mécanistique qui combine les mesures et le bilan de quantité de mouvement unidimensionnel. Nos résultats indiquent que les mécanismes de frottement et de flottabilité sont dominant mais que les forces de résistance de la canopée du paturage et la pression modélisée de la couche extérieure (en condition de vent faibles) sont aussi importantes. En somme, ce modèle unidimensionnel, où les relations de flux-profil que nous avons développées pourraient remplacer les modèles sur terrain plat inadaptés pour la modélisation numérique à large échelle, pourrait améliorer les prévisions atmosphériques en régime d'écoulement catabatiques. En outre, les corrections du tilt des capteurs et l'aligement des forces de flottabilité, appropriées aux topographies complexes et raides, améliorent les estimations des flux turbulents, ramifiliées aux analyses de similarité ou de bilan qui nécessitent une quantification précise des échanges turbulents.

Mots clefs : Météorologie de montagne · Échanges turbulents · Topographie complexe · Vent catabatique · Corrections du tilt de capteurs · Systèmes de coordonnées inclinées · Équilibre dynamique unidimensionnel · théorie de similarité de Monin-Obukhov · Relations de flux-profil · Énergie cinétique turbulente

Contents

List of Figures

List of Tables

1 Introduction

There is nothing with which we come into contact more frequently than the atmosphere. It is where we live and breathe. Less obvious perhaps is the extent to which turbulent exchange in the atmospheric boundary layer (ABL) affects daily life. Turbulent transport of heat, moisture and pollutants for example, can dictate the prices of agricultural goods, what clothes we might wear on a particular day, or our overall health and quality of life. Furthermore, the ability to quantify and model turbulent exchange between the atmosphere and the underlying surface is important for accurate hydrometeorological predictions and water resource management, numerical weather predictions, wind energy assessment and production, climate modeling, various agricultural activities, air quality monitoring and predictions, natural hazard risk assessment and mitigation, and even transportation safety. Hence, understanding physical processes that occur in the ABL have social and economic ramifications as well as scientific.

The majority of existing theories regarding flows in the ABL hold for regions of underlying flat, uniform, and statistically homogeneous terrain. However, essentially the entire Earth's land surface is complex terrain, which to varying degrees, is neither uniform nor locally homogeneous even if flat [Brutsaert, 1998]. Environmental complexities at the Earth's surface on a wide range of scales, from mountain ranges and urban centers to patches of moisture in a wheat field or a dirt road in the desert, complicate the nature of turbulent exchange in comparison to completely idealized surfaces. In the best case scenarios, these complexities contribute only small uncertainties to the end result, and the theoretical models work quite well from a practical perspective. In the worst cases, uncertainties caused by environmental heterogeneity cause the theoretical models to break down completely [Brutsaert, 1998]. Atmospheric flows in mountainous regions often fall into the latter category. Hence, observations in mountainous environments are necessary to construct a sufficiently deep understanding of the physical processes governing such flows to subsequently develop more appropriate theoretical models. Turbulent transport in alpine environments is the main topic of this dissertation, in which field observations in consort with theoretical arguments are employed to reveal the governing physical mechanisms of these complex flow scenarios.

1.1 Atmospheric Boundary Layer Turbulence

The lowermost region of the atmosphere, the troposphere, is divided further into two main layers, the free atmosphere and the atmospheric boundary layer (ABL). The depth of the ABL is spatially and temporally variable; it is defined as the depth over which the surface conditions, such as temperature, roughness or moisture, influence the atmospheric conditions on timescales of about an hour or less [Stull, 1988]. This definition of the ABL implies exchanges between the surface and the atmosphere. Outside of certain synoptic weather events, regular rhythms such as seasonal or diurnal cycles in ABL characteristics are controlled by the surface energy budget, which tracks the partitioning of the available energy (predominantly solar energy) into various forms of heat [Brutsaert, 2005, Whiteman, 2000]. The ground heat flux, which heats the surface, typically occurs via molecular diffusion; whereas the latent heat flux (energy consumed or supplied as the available moisture changes phase) and the sensible heat flux (the energy responsible for changing air temperatures) chiefly take place via atmospheric turbulence, which on scales larger than a few millimeters, transfers heat more efficiently than molecular or radiative processes in gases. Hence, turbulent exchange between the surface (land, water, snow, etc.) and the atmosphere is responsible for generating typical climatic conditions. Beyond heat and moisture, turbulent transport of other scalars, like greenhouse gasses and other pollutants, can dominate over transport by other atmospheric motions such as the mean wind (advection) or wave motions [Stull, 1988].

In a linguistic sense, turbulence can be difficult to define; often it is explained with adjectives. For example, the following words and phrases are regularly used to describe turbulence: chaotic, three-dimensional, multi-scale, seemingly random, mysterious, irregular swirls of eddies, the gustiness of wind, etc. Alternatively, visual mediums are frequently used to describe turbulence, for example: the whorls and swooshes behind rocks in a stream, expanding vortical plumes of smoke or the flutter of a tree leaf. Turbulence has even been the muse of mathematicians, poets and artists, such as Leonardo da Vinci. Mathematically, turbulence is quite easily defined as fluctuations from the spatial or temporal (or both) mean. However simple the definition, the exact details of each turbulent motion are unpredictable and irregular, and the interactions between turbulent fluctuations are nonlinear [Brutsaert, 1998]. This stochasticity implies that turbulence requires a statistical approach in its analysis.

The ABL is almost always turbulent. This turbulence occurs over and contains a wide range of length scales from nearly the depth of the ABL to just a few millimeters. Larger turbulent eddies contain more energy than smaller ones. However, this energy is transferred from large eddies to smaller and smaller eddies in the *energy cascade* down to the smallest possible eddies, where viscosity dissipates the mechanical energy in the eddies and transforms it into heat [Stull, 1988, Arya, 2001]. Hence, turbulence cannot sustain itself without an energy source.

Much of the turbulence in the ABL is generated via two surface-related processes. The first is mechanical shear production of turbulence. Vertical wind shear, or a vertical gradient in wind velocity, is usually caused by frictional drag at the surface. Wind shear tends to enhance

perturbations to generate or strengthen turbulence. The second mechanism is buoyant production of turbulence. The concept of buoyant production of turbulence is linked to the concept of atmospheric (un)stability. Fundamentally, perturbations in any *stably stratified* fluid (having heavier, more dense fluid below lighter less dense fluid) become damped and tend toward the equilibrium state. Whereas, perturbations in an *unstably stratified* fluid (having lighter, less dense fluid below heavier, more dense fluid) will tend to grow, generating convective plumes and increasing turbulence intensity [Turner, 1973, Stull, 1988]. Hence, atmospheric stability essentially quantifies the atmosphere's hindrance to buoyant vertical motions [Whiteman, 2000]. Under typical daytime conditions, solar heating of the surface causes air near the surface to heat more rapidly than the air aloft; this is depicted in the daytime (12:00 to 17:00) portion of Figure 1.1, showing air temperature decreasing with distance above the surface. This warmer air is less dense than the relatively cooler air above it (an unstable ABL), and so it tends to rise (much like a hot air balloon), generating large buoyant eddies, or *thermals* [Stull, 1988]. Conversely at night, the opposite typically occurs; radiative cooling at the surface causes the air near the surface to become more cold and dense than the air at higher elevations. The early morning hours in Figure 1.1 clearly show this *temperature inversion*, or temperature increasing with distance from the surface. Under such conditions, negative buoyancy suppresses vertical motion, and so the atmosphere is characterized as *stable*. Hence, the 'strength' of turbulence in the ABL, or the energy that turbulence possesses, is largely governed by atmospheric stability [Stull, 1988].

To summarize, proceed from left to right in Figure 1.1 to follow a typical clear-sky, summertime daily cycle. Very early in the morning (≈03:00) the air near the surface is colder than the air above it (a temperature inversion); the air does not have a tendency to rise under buoyant forces, and the atmosphere is characterized as stable with relatively little kinetic energy in the turbulence. As dawn approaches, the temperature inversion begins to weaken, and at local sunrise the surface begins to receive direct solar radiation and heat up. This relatively warmer surface begins to heat the air close to the surface more rapidly than than the air aloft (≈12:00); the warmer air has a tendency to rise due to buoyancy, and is characterized as unstable and having relatively more kinetic energy in the turbulence. After local sunset, the solar energy 'switch' is turned off, and the surface begins to cool faster than the air aloft to again form the nighttime temperature inversion. The cycle repeats.

1.1.1 Similarity Theory

Due to the stochastic nature of turbulence and other complicated physical interactions on various scales, it is generally not possible to derive a full analytical description of ABL flows based on first principles of physics and thermodynamics [Stull, 1988]. In these cases, similarity theory, which takes advantage of repetitive characteristics in the ABL, is the only practical approach [Brutsaert, 1998, Stull, 1988]. The approach of similarity theory is to group the variables of interest via dimensional analysis to determine if they are functionally related, once properly scaled. If related, these so called 'universal' functionalities must be determined empirically

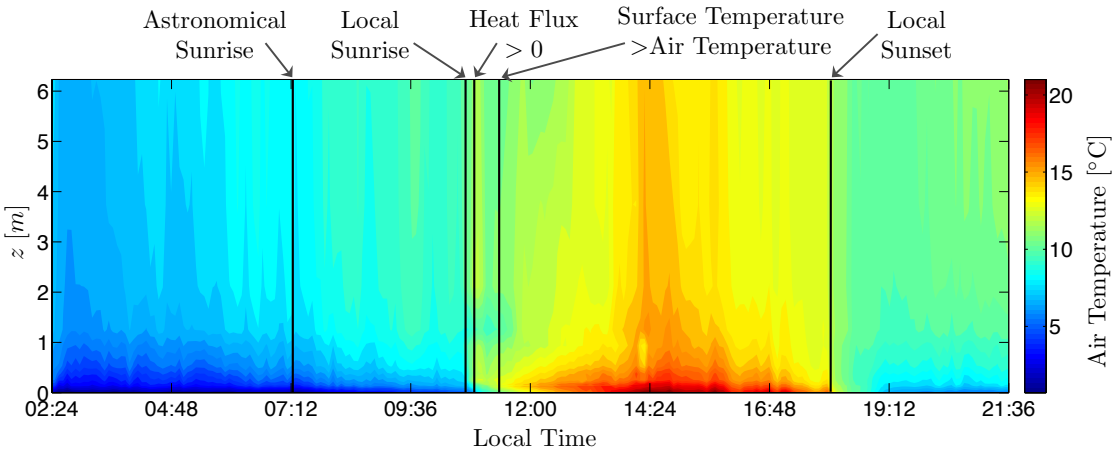

Figure 1.1 – Example of a typical diurnal pattern in near-surface air temperatures over an alpine slope in Val Ferret, Switzerland. Measurements were made with an array of 14 thin-wire thermocouples arranged with increasing resolution near the surface. They indicate an unstable boundary layer during the day and a stable boundary layer at night.

over a wide range of atmospheric conditions, usually varying stabilities. When appropriate, similarity theory can be a powerful tool for use in turbulence closure models or in prescribing wall models, which translate the surface conditions into atmospheric characteristics at a prescribed height above the surface. Monin-Obukhov similarity theory (see Monin and Obukhov [1959]) marks a major turning point in advancing our understanding of turbulent exchange in the ABL [Brutsaert, 1998, Businger and Yaglom, 1971, Foken, 2006]. Major assumptions for its applicability are stationarity, flat and statistically homogeneous underlying terrain, and the presence of a 'constant-flux' surface layer. These strict assumptions are rarely ever met in ABL flows. However in a practical sense, Monin-Obukhov similarity theory has been shown to be valid under a wide range of situations. This can generally be attributed to two characteristics of the ABL; first, horizontal scales of motion in the ABL are much larger than vertical scales, and second, the efficiency with which turbulence mixes tends to statistically wipe out small-scale inhomogeneities presented by the underlying surface [Brutsaert, 1998]. So turbulence can also be forgiving.

1.2 Flows in Mountainous Regions

In certain situations, inhomogeneities at the underlying surface are too great for turbulence to wash out and Monin-Obukhov similarity theory breaks down. As with flat terrain, variability in land-surface cover in mountainous terrain can introduce inhomogeneities in roughness, soil moisture, albedo, etc. that influence turbulent exchange. However, mountainous terrain introduces a host of additional complex features not usually exhibited by flat terrain. Some examples are, aspect irregularities and terrain shadowing associated with variable solar insolation [Nadeau et al., 2013, Lehner et al., 2011, Whiteman and Allwine, 1986], and terrain-

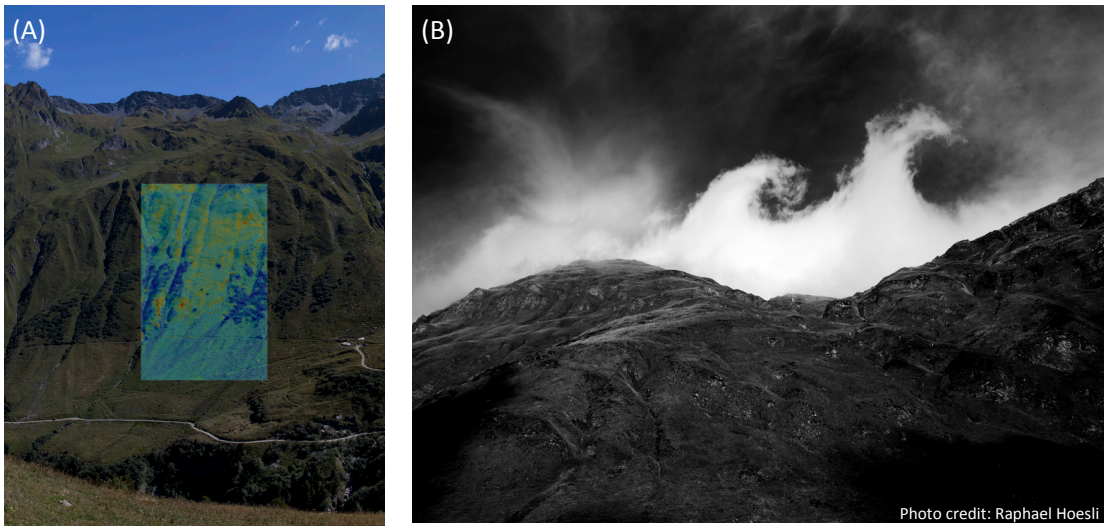

Figure 1.2 – (A) Photo of an alpine slope (valley floor to ridge line is ~ 1000 m) in Val Ferret, Switzerland with an infrared surface temperature thermal image overlay showing how small-scale variability in local aspect generates variability in surface heating. (B) Clouds over alpine peaks exhibiting terrain-induced Kelvin-Helmholtz wave forms.

induced forcing associated with gravity waves, gap flows or wake vortices which introduce non-local, multi-scale flow interactions (see Figure 1.2)[Whiteman, 2000, Sgouros and Helmis, 2009, Mahrt and Larsen, 1990, Manins and Sawford, 1979]. Therefore, the extent to which the application of Monin-Obukhov similarity theory is valid or invalid for mountainous terrain is largely unknown. It has been shown to be relatively suitable in mountainous environments for scaling second-order moments (e.g., De Franceschi et al. [2009], Rotach et al. [2008] and Nadeau et al. [2012]), but to break down over sloping terrain for flux-profile relations (e.g., Nadeau et al. [2012] and Smeets et al. [1998]). Moreover, the relative lack of turbulence observations over such terrain leaves this an open question.

In contrast, mean, thermally-driven, diurnal circulation patterns over slopes and in valleys have been well known since early investigations began in the Alps in the 1930's and 1940's (e.g., Defant [1949], Ekhart [1944], Prandtl [1942] and Wagner [1938]). Under clear skies with weak synoptic forcing, daytime solar heating of the surface generates unstable stratification, which near the surface is aligned with the sloping terrain. This buoyancy field causes warm air to rise upslope to generate *anabatic* flow. At night radiative surface cooling generates stable stratification and a negative buoyancy field, and triggers downslope or *katabatic* flow [Whiteman, 2000]. Katabatic flows quite often also occur over glaciers and ice sheets, and are not confined only to nighttime flows, but instead to near-surface stable stratification [Greuell et al., 1997, Oerlemans, 1998, Smeets et al., 1998]. The velocity profiles of katabatic flows exhibit a characteristic 'jet shape', wherein the 'jet peak', or maximum wind speed, is located at a height above, but near the surface, as shown in Figure 1.3. These jet-like velocity profiles also occur in anabatic flows, though they are less pronounced because vertical motions are

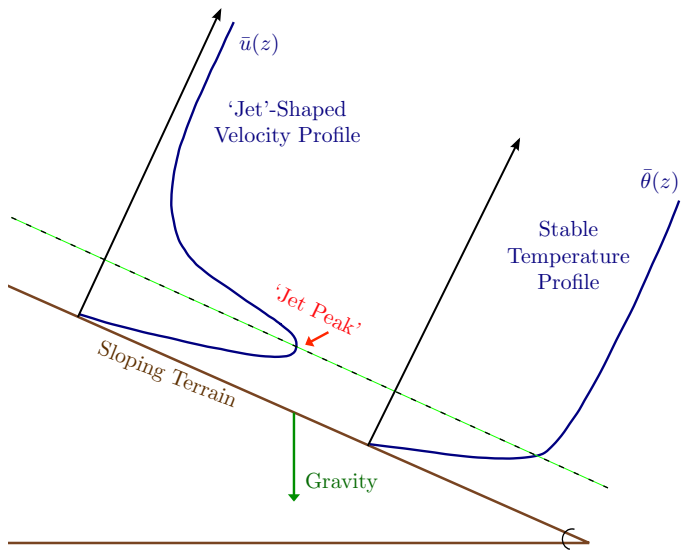

Figure 1.3 – Schematic of a katabatic flow showing the characteristic jet-shaped velocity profile and 'jet peak', or elevated velocity maximum, and the stable stratification, showing increasing temperature with elevation above the surface to generate the negative buoyancy field and downslope flow.

less restricted in unstable boundary layers.

1.2.1 Katabatic Flow

In addition to the more research-oriented interests of transporting heat [Monti et al., 2002], water vapor, pollutants [Pardyjak et al., 2009] and CO_2 [Sun et al., 2007] via turbulent exchange, the cold-air-transporting nature of katabatic flows means they can play significant roles in fog formation [Duynkerke, 1999], creating visibility concerns for air and auto travel, and frost formation[Laughlin and Kalma, 1987], leading to possible consequences with crop damage. Katabatic flows can also play a role in forming cold air pools in basins and valleys [Whiteman, 2000, Doran and Horst, 1983], which trap pollutants and smog (as shown by Figure 1.4), creating air quality, respiratory and mental health concerns [Lareau et al., 2013]. On a more positive note, the frequency and predictability of katabatic flows can be utilized in wind energy resource development.

Katabatic flows are often confined to thin layers near the surface because atmospheric stability limits vertical turbulent motions [Mahrt et al., 2001]. Subsequently, katabatic flows are characterized by steep vertical gradients in atmospheric quantities, including turbulent fluxes [Mahrt et al., 2001, Nadeau et al., 2012]. These steep gradients have implications for the applicability of Monin-Obukhov similarity theory, which requires a constant-flux-layer assumption. Few observational studies of katabatic flows have investigated turbulent exchange, and even fewer have measured fluxes at more than one or two locations above the surface [Grachev et al., 2014

Figure 1.4 – Poor air quality associated with a persistent cold air pool in the Salt Lake Valley, Utah, USA. Photo is courtesy of the Persistent Cold-Air Pool Study (PCAPS) at the University of Utah [Lareau et al., 2013].

submitted, Nadeau et al., 2012, Smeets et al., 1998, Horst and Doran, 1988].

In sum, the katabatic flow layer is very thin (shallow), the vertical gradients of turbulent fluxes are steep and observations are sparse. Therefore, details regarding the vertical structure of the turbulent fluxes have largely been explored by theoretical and numerical studies (e.g., Axelsen and van Dop [2009], Fedorovich and Shapiro [2009], Grisogono and Oerlemans [2001], Grisogono et al. [2007], Horst and Doran [1988] and Denby [1999]). Large-eddy simulation (LES), a numerical tool that has been quite successful for modeling ABL flows (e.g., Bou-Zeid et al. [2005] and Kumar et al. [2006]), is particularly poorly suited for katabatic flows for a variety of reasons. Several of these reasons are related to general complications in modeling turbulence in the stable boundary layer (see Mahrt [1998] and Mahrt [2014] for details). Moreover, since the katabatic layer is so thin and Monin-Obukhov similarity-based wall models are not well-posed for katabatic flows, the affordability of sufficient grid resolution for LES is also problematic [Renfrew, 2004]. In fact, personal correspondence with Marco Giometto regarding his LES studies of katabatic flow revealed that the height of the jet peak was determined by the location of the lowest grid point, unless several grid points below the jet peak are employed. In summary, many open questions remain regarding the vertical structure and variability of turbulent exchange in katabatic flows, and in flows over mountainous terrain, more generally.

1.3 Research Objectives and Dissertation Structure

The overall objective of this work was to address some of the open questions introduced above, by investigating turbulent transport in alpine environments. Observational investigations of katabatic flows were the main foci, for which turbulence measurements where captured over

a steep, alpine slope in Val Ferret, Switzerland.

However, prior to investigating katabatic flows, some 'best-practices' techniques necessary to accurately calculate and orient turbulent flux measurements over complex and steep terrain are developed in *Chapter 2*. For example, velocity sensor tilt corrections geometrically transform measured three-dimensional velocities from the *fixed* sensor coordinate system into the *streamline* coordinate system of the physical flow. These corrections are necessary to reduce cross-contamination between velocity components for more accurate turbulent flux estimates. In *Chapter 2*, we present objective measures for optimizing sector-wise planar fit sensor tilt corrections, and delve into the intricacies involved with selecting an appropriate coordinate system for analyzing the governing flow equations over steep, fully 3-dimensional terrain.

Chapter 3 and Appendix A.1 present a mechanistic study of the physical processes governing steep-slope katabatic flow. Measurements in consort with a one-dimensional mean momentum balance are employed to investigate physical mechanisms that were not measured directly, such as influences from the underlying grass canopy and larger-scale pressure perturbations.

An evaluation of Monin-Obukhov similarity theory for katabatic flows is presented in *Chapter 4*. This chapter also analyzes the vertical structure of turbulent fluxes in the katabatic layer to understand turbulent mixing mechanisms and advance similarity theory for such flows.

Summarizing conclusions and general outlook regarding turbulent exchange in complex, alpine environments are provided in *Chapter 5*. Finally, auxiliary investigations and field campaigns addressing turbulent processes in complex environments are included in the appendices. *Appendix A.2* presents a study of thermodynamic properties of seasonal snow, motivated by a potential influence between vertical turbulent motions in the atmosphere and heat transfer in the snow pack. In addition, a summary of field investigations related to turbulent transport in complex alpine environments is provided in *Appendix A.3*. These field experiments were carried out during my PhD work, but not directly investigate in this dissertation. They introduce several more open questions regarding atmospheric turbulence in alpine environments. The next three chapters present the detailed investigations and scientific contributions that were made during this PhD work, starting with addressing standard techniques that much be altered for flows over complex topography, in Chapter 2.

Bibliography

SP Arya. *Introduction to micrometeorology*, volume 79. Academic Press, 2001.

SL Axelsen and H van Dop. Large-eddy simulation of katabatic winds. part 1: Comparison with observations. *Acta Geophysica*, 57(4):803–836, 2009.

E Bou-Zeid, C Meneveau, and MB Parlange. A scale-dependent lagrangian dynamic model for large eddy simulation of complex turbulent flows. *Physics of Fluids*, 17:025105, 2005.

W Brutsaert. Land-surface water vapor and sensible heat flux: Spatial variability, homogeneity, and measurement scales. *Water resources research*, 34(10):2433–2442, 1998.

W Brutsaert. *Hydrology: an introduction*. Cambridge University Press, Cambridge, UK, 2005.

JA Businger and AM Yaglom. Introduction to Obukhov's paper on turbulence in an atmosphere with a non-uniform temperature. *Boundary-Layer Meteorology*, 2(1):3–6, 1971.

M De Franceschi, D Zardi, M Tagliazucca, and F Tampieri. Analysis of second-order moments in surface layer turbulence in an alpine valley. *Quarterly Journal of the Royal Meteorological Society*, 135(644):1750–1765, 2009.

F Defant. Zur theorie der hangwinde, nebst remerkungen zur theorie der berg- und talwinde [a theory of slope winds, along with remarks on the theory of mountain winds and valley winds]. *Archiv fuer Meteorologie Geophysik und Biolimatologie*, Ser. A, 1:421–450, 1949.

B Denby. Second-order modelling of turbulence in katabatic flows. *Boundary-Layer Meteorology*, 92(1):65–98, 1999.

JC Doran and TW Horst. Observations and models of simple nocturnal slope flows. *Journal of the Atmospheric Sciences*, 40(3):708–717, 1983.

PG Duynkerke. Turbulence, radiation and fog in dutch stable boundary layers. *Boundary-Layer Meteorology*, 90(3):447–477, 1999.

E Ekhart. Beitraege zur alpinen meteorologie [contributions to alpine meteorology]. *Meteorologische Zeitschrift*, 61(7):217–231, 1944.

E Fedorovich and A Shapiro. Structure of numerically simulated katabatic and anabatic flows along steep slopes. *Acta Geophysica*, 57(4):981–1010, 2009.

T Foken. 50 years of the Monin–Obukhov similarity theory. *Boundary-Layer Meteorology*, 119 (3):431–447, 2006.

AA Grachev, LS Leo, S Di Sabatino, HJS Fernando, ER Pardyjak, and CW Fairall. Structure of turbulence in katabatic flows below and above the wind-speed maximum. *Boundary-Layer Meteorol*, 2014 *submitted*.

W Greuell, WH Knap, and PC Smeets. Elevational changes in meteorological variables along a midlatitude glacier during summer. *Journal of Geophysical Research*, 102(D22):25941–25, 1997.

B Grisogono and J Oerlemans. A theory for the estimation of surface fluxes in simple katabatic flows. *Quarterly Journal of the Royal Meteorological Society*, 127(578):2725–2739, 2001.

B Grisogono, L Kraljević, and A Jeričević. The low-level katabatic jet height versus Monin–Obukhov height. *Quarterly Journal of the Royal Meteorological Society*, 133(629):2133–2136, 2007.

TW Horst and JC Doran. The turbulence structure of nocturnal slope flow. *Journal of the atmospheric sciences*, 45(4):605–616, 1988.

V Kumar, J Kleissl, C Meneveau, and MB Parlange. Large-eddy simulation of a diurnal cycle of the atmospheric boundary layer: Atmospheric stability and scaling issues. *Water Resour. Res*, 42(6):W06D09, 2006.

NP Lareau, E Crosman, CD Whiteman, JD Horel, SW Hoch, WOJ Brown, and TW Horst. The persistent cold-air pool study. *Bulletin of the American Meteorological Society*, 94(1):51–63, 2013/02/26 2013. doi: 10.1175/BAMS-D-11-00255.1. URL http://dx.doi.org/10.1175/BAMS-D-11-00255.1.

GP Laughlin and JD Kalma. Frost hazard assessment from local weather and terrain data. *Agricultural and forest meteorology*, 40(1):1–16, 1987.

M Lehner, CD Whiteman, and SW Hoch. Diurnal cycle of thermally driven cross-basin winds in arizona's meteor crater. *Journal of Applied Meteorology and Climatology*, 50(3):729–744, 2011.

L Mahrt. Stratified atmospheric boundary layers and breakdown of models. *Theoretical and computational fluid dynamics*, 11(3):263–279, 1998.

L Mahrt. Stably stratified atmospheric boundary layers. *Annual Review of Fluid Mechanics*, 46(1):23–45, 2014. doi: 10.1146/annurev-fluid-010313-141354. URL http://dx.doi.org/10.1146/annurev-fluid-010313-141354.

L Mahrt and S Larsen. Relation of slope winds to the ambient flow over gentle terrain. *Boundary-Layer Meteorology*, 53(1):93–102, 1990.

L Mahrt, D Vickers, R Nakamura, MR Soler, J Sun, S Burns, and DH Lenschow. Shallow drainage flows. *Boundary-layer meteorology*, 101(2):243–260, 2001.

PC Manins and BL Sawford. Katabatic winds: A field case study. *Quarterly Journal of the Royal Meteorological Society*, 105(446):1011–1025, 1979.

AS Monin and AM Obukhov. Basic laws of turbulent mixing in the surface layer of the atmosphere. *Contrib Geophys Inst Acad Sci USSR151*, 24(151):163–187, 1959.

P Monti, HJS Fernando, M Princevac, WC Chan, TA Kowalewski, and ER Pardyjak. Observations of flow and turbulence in the nocturnal boundary layer over a slope. *J. Atmos. Sci.*, 59(17): 2513–2534, September 2002.

DF Nadeau, ER Pardyjak, CW Higgins, and MB Parlange. Similarity scaling over a steep alpine slope. *Boundary-Layer Meteorol*, 147(3):401–419, 2012.

DF Nadeau, ER Pardyjak, CW Higgins, H Huwald, and MB Parlange. Flow during the evening transition over steep alpine slopes. *Quarterly Journal of the Royal Meteorological Society*, 139(672):607–624, 2013. ISSN 1477-870X. doi: 10.1002/qj.1985. URL http://dx.doi.org/10.1002/qj.1985.

J Oerlemans. The atmospheric boundary layer over melting glaciers. *Clear and cloudy boundary layers*, pages 129–153, 1998.

ER Pardyjak, HJS Fernando, JCR Hunt, AA. Grachev, and J Anderson. A case study of the development of nocturnal slope flows in a wide open valley and associated air quality implications. *Meteorologische Zeitschrift*, 18(1):85–100, 2009.

L Prandtl. *Führer durch die Strömungslehre*. Vieweg und Sohn, Braunschweig, 1942.

IA Renfrew. The dynamics of idealized katabatic flow over a moderate slope and ice shelf. *Quarterly Journal of the Royal Meteorological Society*, 130(598):1023–1045, 2004.

MW Rotach, M Andretta, P Calanca, AP Weigel, and A Weiss. Boundary layer characteristics and turbulent exchange mechanisms in highly complex terrain. *Acta Geophysica*, 56(1): 194–219, 2008.

G Sgouros and CG Helmis. Low-level jet development and the interaction of different scale physical processes. *Meteorology and Atmospheric Physics*, 104(3):213–228, 2009.

CJPP Smeets, PG Duynkerke, and HF Vugts. Turbulence characteristics of the stable boundary layer over a mid-latitude glacier. part I: A combination of katabatic and large-scale forcing. *Boundary-Layer Meteorology*, 87(1):117–145, 1998.

RB Stull. *An Introduction to Boundary Layer Meteorology*. Kluwer Academic publishers, 1988.

J Sun, SP Burns, AC Delany, SP Oncley, AA Turnipseed, BB Stephens, DH. Lenschow, MA LeMone, RK Monson, and DE Anderson. CO2 transport over complex terrain. *Agricultural and Forest Meteorology*, 145(1-2):1–21, 2007.

J. S. Turner. *Buoyancy Effects in Fluids*. Cambridge University Press, 1973. ISBN 9780511608827. URL http://dx.doi.org/10.1017/CBO9780511608827. Cambridge Books Online.

A Wagner. Theorie und reobachtung der periodischen gebirgswinde [theory and observatjon of periodic mountain winds]". *Gerlands Beitr . Geophys*, 52:408–449, 1938.

CD Whiteman. *Mountain Meteorology: Fundamentals and Applications*. Oxford University Press, USA, 2000.

CD Whiteman and KJ Allwine. Extraterrestrial solar radiation on inclined surfaces. *Environmental Software*, 1(3):164–169, 1986.

2 Adapting Tilt Corrections and the Governing Flow Equations for Steep, Fully Three-Dimensional, Mountainous Terrain

The previous chapter introduced the topic of turbulent exchange in the atmospheric boundary layer, and presented some of the open questions in the field of mountain hydrometeorology. This chapter addresses some of the complications associated with applying traditional techniques to turbulent flux measurements over complex and steeply sloping topography. It has been submitted for publication with the following citation:

H J Oldroyd, E R Pardyjak, H Huwald and M B Parlange. Adapting Tilt Corrections and the Governing Flow Equations for Steep, Fully Three-Dimensional, Mountainous Terrain. *Boundary-Layer Meteorology, under review*

Abstract: *Due to increased activity in studying atmospheric turbulent surface exchanges in more complex environments, some questions have arisen concerning velocity sensor tilt corrections and the governing flow equations for coordinate systems aligned with steep slopes. The standard planar fit (PF) method, a popular tilt correction technique, must be modified when applied to complex mountainous terrain. The ramifications of these adaptations have not fully been explored in the literature. In this paper, we carefully evaluate the impacts of the selection of sector size (the range of wind angles admitted for analysis) and PF averaging time. This work offers a methodology to determine an optimized sector-wise planar fit (SPF), and evaluates the sensitivity of momentum fluxes to varying these SPF input parameters. Additionally, this work clarifies discrepancies in the governing flow equations for slope-aligned coordinate systems that arise in the buoyancy terms due to the gravitational vector no longer acting along a coordinate axis. New adaptions to the momentum equations and turbulence kinetic energy budget equation allow for the proper treatment of the buoyancy terms for purely up or downslope flows and for slope flows having a cross-slope component. Field data show that new terms in the slope-aligned*

forms of the governing flow equations can be significant and should not be omitted. Since the optimized SPF and the proper alignment of buoyancy terms in the governing flow equations both affect turbulent flux quantities, these results hold implications for similarity theory or budget analyses for which accurate flux estimates are important.

Keywords: Complex terrain · Governing flow equations · Sensor tilt corrections · Slope flows · Turbulent flux measurements

2.1 Introduction

Turbulence measurements over complex terrain have recently been given increased attention, largely motivated by the need to quantify greenhouse gas fluxes [Feigenwinter et al., 2008, Baldocchi et al., 2000] and improve model parameterizations in numerical weather prediction codes for wind power, hydrological and meteorological forecasting, which typically implement models that were developed for flat and statistically homogeneous terrain (e.g., Shamarock et al. [2008] and Xue et al. [2001]). For example, the flat-terrain relations developed via Monin-Obukhov similarity theory are widely implemented in models, but break down for steep, sloping terrain where the fluxes throughout the thin, slope-flow layer can vary by far more than 10% [Nadeau et al., 2012].

Given this increased attention to turbulence measurements over steep terrain, some questions have arisen regarding discrepancies in the form of the governing flow equations applied to these flow scenarios. The roots of these concerns can be explained by the challenges that steep, sloping and/or geometrically variable terrain poses for choosing coordinate systems, and subsequently, how best to measure and then transform the velocity data into that coordinate system [Stiperski and Rotach, 2014, Ross and Grant, 2014, Ono et al., 2008, Yuan et al., 2007, 2011].

Near the surface in the atmospheric boundary layer (ABL), surface-normal wind shear acts parallel to the local terrain, whereas buoyancy always acts parallel to the gravitational force vector. In the case of flat terrain, it is obvious that the governing equations of motion should be written for a horizontal/vertical (HV) coordinate system because the terrain normal and gravitational vectors are parallel. However, for significantly steep terrain, the choice of coordinate system is not obvious, and implicitly, any choice consequentially must consider that the forcings arising from buoyancy and shear are no longer perpendicular [Sun, 2007]. Most commonly, an orthogonal coordinate system that follows the sloping terrain (slope-normal/slope-parallel hereafter called SNSP; see Fig. 2.1c for a 2D schematic) is used to simplify the momentum equations. However, in the SNSP coordinate system, the buoyancy force is no longer aligned with the terrain-normal direction. Clearly, the governing flow equations must be adapted to account for this reorientation. The SNSP forms of the momentum equations have been interpreted consistently between studies for pure (up or down) slope flows. However, the specific SNSP adaptations for slope flows with a cross-slope component have been largely unaddressed. In addition, formulations of the terms accounting for buoyant production/consumption of

turbulence kinetic energy (TKE) in the TKE budget equation are inconsistent among various studies (see Sect. 2.8 for a more complete problem description). One of the primary goals of this study is to derive more generalized forms of the governing flow equations that are also appropriate for streamwise-oriented, terrain-following, SNSP coordinate systems, such that the adaptations are clear and that any discrepancies are easily rectified.

An additional complication for steep, complex terrain is that the velocity measurements must be taken in or transformed into the SNSP coordinate system. Herein, 'complex terrain' refers mainly to geometrical variability of the terrain that is significant enough that it cannot be lumped into a roughness length, or canopy scheme. It has been shown for sonic anemometer measurements over sloping terrain that mounting the sensor in SNSP coordinate system reduces flow distortion, especially in the surface-normal direction [Geissbühler et al., 2000, Christen et al., 2001]. However, since exact sensor alignment is difficult even for flat terrain, a tilt correction should also be performed to reduce cross-contamination between velocity components [Lee et al., 2006]. This cross-contamination not only affects the mean velocity measurements through misalignment, but also contributes to greater errors in flux estimates, especially for the momentum fluxes [Kaimal and Haugen, 1969, Wilczak et al., 2001]. The planar-fit (PF) tilt correction described by Wilczak et al. [2001] is a commonly-used technique to reduce the cross-contamination errors due to sensor misalignment. For measurements over more complex topography, the sector-wise planar-fit (SPF) tilt correction is often used [Ono et al., 2008, Yuan et al., 2007, 2011]. For the SPF, PF tilt corrections are performed for individual wind direction sectors. For example, it has been applied to a steeply sloping alpine site [Nadeau et al., 2012], at other mountainous sites [Ono et al., 2008, Yuan et al., 2007, 2011], and for benthic flux measurements in a river flow over a complex bedform [Lorke et al., 2013]. This popularity has arisen because the SPF technique has been shown to provide better momentum flux estimates, compared to those of a single sector PF, by accounting for the terrain-induced directional variability of the mean streamline plane [Ono et al., 2008]. Implementation of the SPF approach requires selection of sector sizes, sector locations, and the PF averaging time (see Sect. 2.3). These parameters are typically reported in studies with little or no justification and without sensitivity analyses. Since they are site dependent, it can be difficult for researchers to know how to best select the appropriate parameters. Therefore, another primary aim of this paper is to provide an objective methodology for determining the SPF degrees of freedom, and subsequently to quantify the implications of these choices on the resulting averaged momentum fluxes.

Overall, this paper seeks to address issues associated with adapting common techniques, such as sensor tilt corrections and properly aligning the governing flow equations to SNSP coordinate systems, for field measurement sites having steep and/or complex topography. More specifically, this paper addresses the governing assumptions and the most appropriate coordinate and equation alignments that compose a framework to best capture the turbulence statistics over steep and fully three-dimensional terrain. Field data from two sites, one flat and uniform and the other steep and variable, are used as examples for the methodologies introduced herein, and are presented in Sect. 2.2. Following Sect. 2.2 and with the exception

of the Conclusions Section (Sect. 2.10), this paper is organized such that it can be read in two parts, one addressing the optimization for sensor tilt corrections (Sects. 2.3 to 2.7) and the other addressing adaptations of the governing flow equations for SNSP coordinate systems (Sects. 2.8 and 2.9). Each part begins with a more specific problem description, followed by methodologies, examples from field data, and discussions and recommendations. Finally, Sect. 2.10 summarizes the main conclusions and recommendations.

2.2 Field Experiment Sites

Data sets from two field experiment sites using the same sonic anemometer model are used to illustrate the methodologies and developments presented herein. The two sites were chosen because they represent drastically different topography (see Fig. 2.1) and therefore, nicely elucidate the complications associated with measurements over complex topography. The first site (PLAYA) is essentially a control site for the sensor tilt correction analysis. The PLAYA site (40.13498 N, 113.45158 W) shown in Fig. 2.1a is located in the Great Salt Lake Desert of the United States on the dry lake bed of the prehistoric Lake Bonneville (surrounding what is presently The Great Salt Lake, Utah). The terrain at the PLAYA site is extremely flat, smooth ($z_o < 1$ mm) and uniform (≈ 1 m change in elevation per 10 km) [Metzger et al., 2007], and provides an idealized data set for comparison and methodology validation. The site is so idealized that the nearby Surface Layer Turbulence and Environmental Science Test (SLTEST) site has historically been used for fundamental, high Reynolds number, wall-bounded flow studies (e.g., Klewicki et al. [1995], Kunkel and Marusic [2006], Hutchins and Marusic [2007]) and measurements testing subgrid-scale models commonly used in large-eddy simulations (e.g., Carper and Porté-Agel [2004], Higgins et al. [2007, 2009]). The two dominant wind directions under fair weather conditions at the site are northerly and southerly. In this work, 20 Hz data from a sonic anemometer (CSAT3, Campbell Scientific) mounted at 10.4 m above ground on a 28 m tower during May 2013 are used. The sonic anemometer was oriented 250° from north, such that the tower and mounting arm are located at 47° from north. The data were collected as part of the Mountain Terrain Atmospheric Modeling and Observations (MATERHORN) Program [Fernando and Pardyjak, 2013, Fernando et al., 2015 *in press*]. Details of the full set of flux observations made at the PLAYA site are given in Jensen et al. [2015 *in press*].

The SLOPE site (45.90179 N, 7.12374 E) shown in Fig. 2.1b is located in Val Ferret, a narrow alpine valley in Switzerland near the Italian and French borders (see also Simoni et al. [2011], Nadeau et al. [2013], Mutzner et al. [2013] and Oldroyd et al. [2014] for more site and hydrometeorological descriptions). The slope has a west-facing aspect, and locally, a slope angle of 35.5°. Figure 2.1d shows the steep, complex terrain surrounding the SLOPE site tower. Vegetation surrounding the SLOPE tower is characterized by 30 cm-high alpine grasses and flowers. The dominant fair weather wind directions are east (down-slope, $\phi \approx 85°$, where ϕ is defined as degrees from north) at night and north-west (up slope and up valley, $\phi \approx 285°$) during the day. The 20 Hz data from a sonic anemometer (CSAT3, Campbell Scientific) mounted at a

surface-normal height of 1.27 m above ground from 1 September to 5 October 2011 are used for methodology examples and subsequent flux analyses. The sonic anemometer was oriented to the north, such that the tower and mounting arms were located at 180° from north. In addition, the anemometer was mounted with a SNSP tilt from vertical (e.g., w_{sonic} aligned with the surface normal and v_{sonic} aligned with the along-slope axis) to reduce flow distortion [Geissbühler et al., 2000, Christen et al., 2001] and tilt correction angles into the streamline-defined SNSP coordinate system. This particular measurement height was chosen for the analyses herein because wind speeds at this height are most consistent between typically day (anabatic) and night (katabatic) flow regimes.

PF and SPF tilt correction methods require a long-term data set to generate statistically robust fitting planes. Yuan et al. [2007] have shown for their SPF corrections that one to two weeks of data were sufficient. However, the exact minimum ensemble averaging time will likely vary by site and the SPF composition. Therefore, to ensure a sufficiently long ensemble averaging time, data from approximately one month at PLAYA and SLOPE sites were selected. In addition, velocity data originating from wind directions behind sonic anemometers are often not used in practice because the mounting arms can disturb the flow field [Foken, 2008]. Li et al. [2013] suggest separating these sectors when performing SPF tilt corrections. However, these data have been retained in this example study so as not to impose any sector definitions *a priori*. Therefore, it should be assumed that data from these sectors are potentially of lower quality (see also Li et al. [2013]).

2.3 Tilt corrections for complex terrain: problem description

Consider a time series of velocity, u_i measured by a stationary sensor (in this case a 3D sonic anemometer) over or surrounded by complex, variable terrain. Here, standard index notation is adopted such that $u_1 = u$, or the streamwise velocity, $u_2 = v$, or the spanwise velocity, and $u_3 = w$, or the surface-normal velocity. Assuming that the flow near the surface follows the terrain, as shown by Sun [2007], the total u_i signal potentially contains a turbulent signal, an atmospheric wave-induced signal (e.g., gravity waves or Kelvin-Helmholtz shear instabilities), and a terrain-induced signal generated by departures from a purely planar underlying surface (local topographical features such as dips, tilts and curvature as are typical of real terrain) or larger-scale terrain features surrounding the measurement site (hills, valleys etc.) that can influences the flow field (see Ono et al. [2008]). Following a time series decomposition analogy, similar to a typical triple-decomposition (e.g., Cheng et al. [2005]), the time series can be expressed by,

$$u_i = \overline{u}_i + u_i' + \tilde{u}_i + \breve{u}_i, \tag{2.1}$$

where $\overline{u}_i$, is the mean, u_i' is the turbulent departure from mean, $\tilde{u}_i$ is the wave signal, and $\breve{u}_i$ is the terrain-induced signal. A major difference between $\tilde{u}_i$ and $\breve{u}_i$ is that $\tilde{u}_i$ is typically identifiable by scale differences from u_i' (see Cheng et al. [2005] or Vickers and Mahrt [2005]),

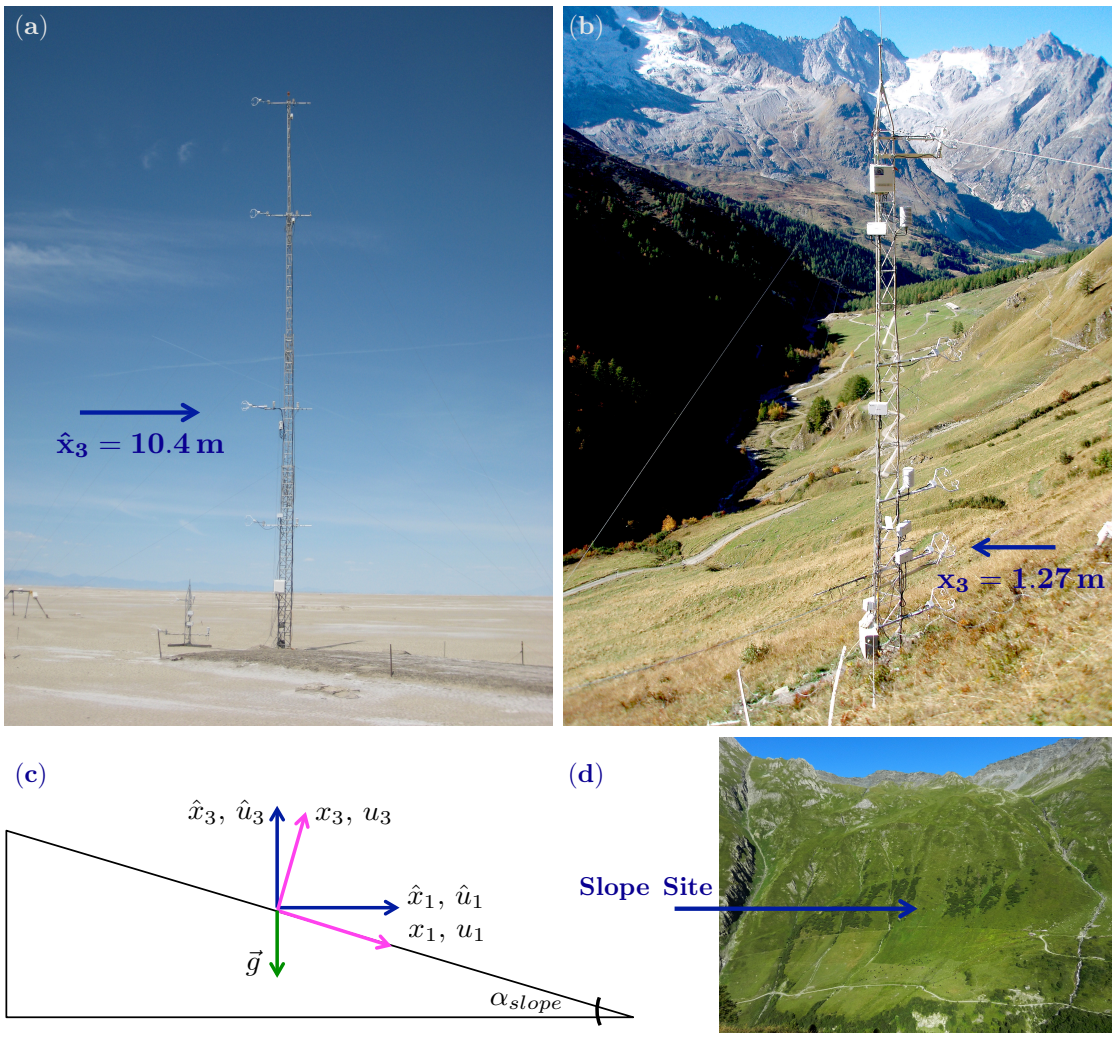

Figure 2.1 – (a) PLAYA and (b) SLOPE field experiment sites. (c) Schematic of a general slope-aligned (magenta, x_3, x_1, for pure downslope flow, not drawn to scale with the SLOPE site) and horizontal-vertical (blue, $\hat{x}_3$, $\hat{x}_1$) coordinate systems (the *hat* accent over a variable indicates the HV coordinate system). (d) Mountainous terrain surrounding the SLOPE site. For scale, the total slope length is ≈1000 m.

whereas $\check{u}_i$ is wind direction dependent and not necessarily scale dependent. If analyzing any component of the time series (e.g., u_i' to calculate turbulent fluxes) is the objective, then $\check{u}_i$ must be removed from the time series, or it will contaminate the other signals. However, defining $\check{u}_i$ exactly and explicitly requires complete knowledge of the sensor's orientation with respect to the terrain for all possible sensor footprints and wind directions. This is a task that is nearly impossible even for flat terrain. Therefore, the goal of implementing a tilt correction scheme for complex topography is to use the measured data to reduce cross-contamination between the directional velocity components, as previously mentioned, but also to simultaneously reduce $\check{u}_i$ as much as possible.

The classical double rotation (DR) tilt correction scheme (traditionally used for uniform and flat terrain) transforms the mean velocities for the desired flux averaging time, τ_f, such that, $\overline{u}_3 = \overline{u}_2 = 0$, for which an over bar indicates time averaging [Kaimal and Finnigan, 1994]. However, for situations where the real $\overline{u}_3$ in the atmosphere may or may not be zero (e.g., a non-zero $\overline{u}_3$ due to subsidence), the planar-fit (PF) tilt correction scheme is advantageous because it allows for $\overline{u}_3 \neq 0$, and instead imposes that $\langle u_3 \rangle = 0$, where the angle brackets indicate the ensemble mean over several averaging periods [Wilczak et al., 2001, Lee, 1998]. Hence, in PF tilt correction schemes, the tilt-corrected velocity time series maintains the original sampling frequency, as opposed to the DR scheme for which the tilting transformations are performed on the flux averaging windows. This has additional advantages, for example, in performing spectral analyses with the tilt-corrected time series. For PF schemes, $\langle u_3 \rangle = 0$ is established by fitting a plane to the mean streamlines of the flow. The best-fit plane is determined through a multiple linear regression by minimizing S, the function given in Wilczak et al. [2001] (on page 142, Eq. 47; the nomenclature has been altered for consistency with that of this document),

$$S = \sum_{j=1}^{N} (\overline{u}_{3m,j} - b_0 - b_1 \overline{u}_{1m,j} - b_2 \overline{u}_{2m,j})^2, \tag{2.2}$$

where the subscript, m indicates the measured velocities (in this case, in the sonic anemometer coordinate system), and the subscript j indicates an individual averaged segment ranging from 1 to N, the total number of averaged segments going into the PF; the $b-$coefficients (subscripts do not invoke summation notation in this case) determine the planar shift and tilt angles in order to transform the measurement coordinate system into a streamline coordinate system; b_0 is the mean offset instrument error in the measured u_3 component, the pitch angle, γ, can be determined by $\sin\gamma = -b_1/\sqrt{b_1^2 + b_2^2 + 1}$ and the roll angle, β, by $\sin\beta = b_2/\sqrt{1 + b_2^2}$ [Wilczak et al., 2001]. Refer to Wilczak et al. [2001] for a complete description of the PF tilt correction methodology. The PF tilt correction generates an orthonormal, streamline-aligned coordinate system; it is therefore also assumed that it generates a terrain-following coordinate system [Wilczak et al., 2001]. However, if the terrain causes significant deviations with wind direction from a true plane, then a single PF tilt correction will be biased toward the terrain over which the wind direction sectors have the highest probability distribution. Since the SPF technique performs the planar fitting for individual wind sectors, it can reduce this wind direction-dependent bias in the tilt corrections, leading to more accurate turbulent flux

estimates from complex environments [Ono et al., 2008]. Therefore, it is assumed that a SPF scheme can remove a significant amount of $\check{u}_i$ from the time series, as well as reduce cross-contamination between velocity components. However, very little has been documented regarding how to select the degrees of freedom for the SPF, such as the sector size, Λ, the sector centre location, and the PF averaging time, τ_{PF}, which is the averaging time used to generate the input data segments (e.g., $\overline{u}_{1m,j}$ in Eq. 2.2) that are used to generate the PF. Although, the choice of τ_{PF} has been shown to have an effect on flux measurements [Vickers and Mahrt, 2006]. The objectives of the following sections are to propose objective methods to quantitatively evaluate how well a particular Λ and τ_{PF} define the tilt correction fitting planes and present hypotheses regarding the optimal choices for Λ and τ_{PF}.

2.3.1 Objectives for SPF optimization

The primary objective is to find the optimal SPF that accounts for terrain irregularities by 'tilting' the sensors *a posteriori* into a streamline-oriented, terrain-following, orthogonal coordinate system given a set of measured 3D velocities. The primary hypothesis is that the best transformation for each wind direction sector will minimize a set of objective 'cost functions'. The first proposed cost function is a root-mean-square (rms) error, S_{rms}, that describes how well the measured streamlines define the fitting plane for a particular Λ and τ_{PF}, such that

$$S_{rms} = \frac{\sqrt{S}}{\sqrt{N}} = f(\tau_{PF}, \Lambda), \tag{2.3}$$

where N is the number of segments going into the PF and S is the PF least-squares minimization function (Eq. 2.2). Note that increasing N increases the statistical significance of the fitting plane, and it has been shown, for example by Yuan et al. [2007], that some minimal N is required to converge the PF tilt coefficients for any given wind sector and τ_{PF}. This minimal N dictates the minimal ensemble averaging time, or amount of data necessary to perform a statistically robust PF (see Yuan et al. [2007] for more details). Its exact value will vary by site and SPF composition, but in practice, typically a few weeks or months provide a sufficient quantity of data [Ono et al., 2008, Wilczak et al., 2001, Yuan et al., 2007, 2011]. For a time series of finite length, Λ, τ_{PF} and N are interlinked in such a way that the minimum S_{rms} will always be for long τ_{PF} and small Λ (as will be shown in Sect. 2.4) because fitting a plane to a single set of streamlines, as in the most extreme case, will always be a better fit (smaller rms error) than multiple sets of streamlines. This idea is similar to the idea that two points define a perfect line. In summary, S_{rms} provides information regarding the quality of the fitting plane, but its minimization is an insufficient criteria for selecting optimal Λ and τ_{PF}. Hence, additional cost functions are necessary. These additional six cost functions seek to locate 'regions of converged' tilt coefficients by minimizing the absolute variability of the PF $b-$coefficients for

changing Λ,

$$\left|\frac{\partial(b_{0,1,2})}{\partial\Lambda}\right| = f(\tau_{PF}, \Lambda), \tag{2.4}$$

and for changing τ_{PF},

$$\left|\frac{\partial(b_{0,1,2})}{\partial\tau_{PF}}\right| = f(\tau_{PF}, \Lambda). \tag{2.5}$$

In practice, these partial derivatives can be estimated with finite differencing or other numerical methods. In total, seven cost functions (Eqs. 2.3, 2.4 and 2.5) have been proposed, and their minimizations can be utilized individually and/or in some combination, for example by summing or weighted summing, to search for optimal Λ and τ_{PF}. Since the units of the cost functions are innately incongruent, it is recommended to use a normalized weighted sum (i.e, normalizing each by its maximum), when analyzing their combined effects. Applied examples of using the cost functions are shown in Sects. 2.4 and 2.5.

2.3.2 Hypotheses for optimal PF averaging time, τ_{PF}

Much has been written regarding the importance of selecting an appropriate averaging time for computing turbulent fluxes, τ_f (e.g., Vickers and Mahrt [2005] and Babić et al. [2012]). However, little has been written regarding the appropriate averaging time for the data segments used to compute the planar fit (PF) coefficients, τ_{PF}. These two averaging times are not necessarily the same for PF methods, as opposed to double or triple rotation tilt correction methods, for which τ_f also imposes the averaging time of the velocity vector transformation. In fact, selecting the appropriate τ_{PF} aims to meet a different objective from selecting an appropriate τ_f for converged flux estimates. In general, τ_{PF} should be long enough such that the *mean streamlines* do not vary excessively and are representative of the mean flow, but short enough such that the velocity signal is reasonably stationary. In addition, a shorter τ_{PF} provides a larger N for the PF plane to be well defined with reduced uncertainty, and for the $b-$coefficients to be well converged. Since statistical significance increases with N, it makes sense to maximize N by choosing the smallest reasonable (minimizes the cost functions) τ_{PF}, that converges the tilt coefficients for a particular sector size.

2.3.3 Hypotheses for optimal SPF sector size, Λ

An optimal SPF wind sector will be large enough such that it envelopes enough of the variability in wind direction, for example, it should encompass some majority of the fluctuations in wind direction, σ_ϕ. However, it should be small enough to reduce the terrain-induced perturbations to the velocity signal, $\breve{u}_i$, which is the reason for using multiple sectors, in the first place. An important distinction must be noted for implementing a cost function methodology to determine Λ for a *dominant* wind direction (i.e., a peak in a wind direction histogram) and

a *secondary* wind direction (i.e., in the tails of the wind direction histogram). For sectors containing a dominant wind direction, the cost functions beyond a certain Λ will be insensitive to increasing Λ because the streamlines in the tails of the wind direction distribution are not statistically frequent enough to have an impact on the cost functions (see examples of this insensitivity in Sect. 2.4). However, whatever transformation is determined for that sector will impact the whole sector, and the more statistically frequent streamlines will determine the tilting angles and subsequently, bias the transformation for the streamlines in the tails of the distribution (similar to the problems with using a single PF). Hence for dominant wind directions, the optimal Λ should be the smallest Λ that minimizes the cost functions. For secondary wind directions, it is more likely that a larger Λ will optimize the PF because some threshold for N (which increases with Λ) is necessary to converge the tilt coefficients (minimize the six $b-$coefficient cost functions in Eqs. 2.4 and 2.5).

2.4 Cost function examples

Examples of the cost function analyses provided for the PLAYA and SLOPE sites are for Λ centred on a dominant wind direction (at ϕ =5° and ϕ =85°, respectively). Since the PLAYA site is characterized by extremely flat terrain, very little change is expected in the cost functions and PF tilt angles for changing Λ and τ_{PF}. Therefore, to test extrema, the test ranges for Λ and τ_{PF} are larger for the PLAYA site than those used for the more complex SLOPE site. Figure 2.2 shows the S_{rms} cost functions for the PLAYA and SLOPE sites. As expected, it shows that S_{rms} is largest for large Λ and in particular, for small τ_{PF} because the mean streamlines require longer averaging times to be representative of the mean flow patterns. As discussed previously, the general trend in S_{rms} tends toward minimization with small Λ and large τ_{PF} as N decreases. This result is expected because in the most extremes, the rms error will be the lowest for a single set of streamlines. However, for a given Λ and τ_{PF}, increasing N will increase the convergence of the PF tilt coefficients and the overall statistical significance of the fitting plane. For data sets of finite length, insufficient N (due to the overall size of the data set, a small Λ, a wind direction sector with a low probability density and/or a long τ_{PF}) will result in non-representative PF tilt angles.

These competing, site-dependent effects and lack of sufficient minimization criteria are the reasons for introducing the six additional cost functions (Eqs. 2.4 and 2.5). Figure 2.3 shows an example of the $\partial b_1/\partial\tau_{PF}$ cost function. Since the b_1 coefficient is used to determine the PF pitch correction angle, γ, Fig. 2.3 shows that γ is highly sensitive to changes in τ_{PF} for very small Λ (< 20°) at both sites. Additionally, since Fig. 2.3 shows results for dominant wind directions, it shows the insensitivity to increasing Λ for the variability cost functions (Eqs. 2.4 and 2.5). As previously discussed, this insensitivity is due to the limited influence that streamlines in the tails of the wind direction histograms can have relative to the more frequently represented streamlines in the peaks. Figure 2.3a also shows that nonstationarity in the velocity measurements with large τ_{PF} can be reflected in the cost functions.

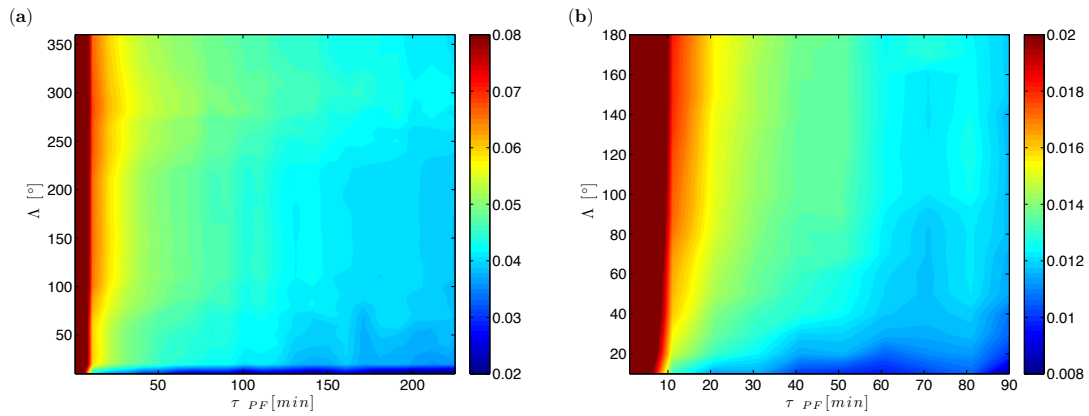

Figure 2.2 – S_{rms} (m s^{-1}) cost function for (a) PLAYA (dominant wind direction sector is centred at ϕ =5°) and (b) SLOPE sites (dominant wind direction sector is centred at ϕ =85°). Note the different scales for Λ and τ_{PF} for the two sites, and that the colour data ranges have been rescaled to show details. The original ranges are 0.015 to 0.13 m s^{-1} and 0.007 to 0.037 m s^{-1} for PLAYA and SLOPE, respectively.

Figure 2.4 shows examples of the normalized weighted sum of all seven cost functions for both field sites. The normalized weighted sum was computed by normalizing each cost function field by its maximum, then summing over the seven cost functions. This is just one possible method for analyzing the combined effects of the cost functions and it has two advantages over a simple, unweighted sum. One advantage is that it ameliorates the problem of having incongruent units between cost functions. Another advantage is that it places all seven cost functions on the same scale from zero to one, such that each cost function contributes equally relative to the sum. The color data in Fig. 2.4 have been rescaled to better show the details. For both sites the maxima of the normalized cost function sums along the coordinate axes are associated with very short τ_{PF} and very small Λ, as expected. In addition to the cost functions, it can be useful to also examine how the actual PF pitch, γ, and roll, β, tilt angles vary with Λ and τ_{PF}, as shown in Fig. 2.5 for both sites. This provides a tangible sense of the physical consequences of a particular choice for Λ and τ_{PF}. Figures 2.5a and c show that for the PLAYA site the PF tilt angles vary by less than 1° for $\Lambda > 20°$ and all τ_{PF} in the test ranges. In contrast, Figs. 2.5b and c containing the PF tilt angles for the SLOPE site, show much more variability (especially for γ) over even the smaller test ranges of Λ and τ_{PF}.

2.5 Methodology for SPF optimization

Since the PF tilt angles for the PLAYA site show very little variability with Λ and τ_{PF} (see Figs. 2.5a and c), a single PF is probably sufficient. Therefore, this section details the methodology used to select Λ, τ_{PF} and wind sector centres for only the more complex SLOPE site. To aid in the methodology description, Fig. 2.6 shows the 20 Hz wind direction histogram for the SLOPE site and the SPF sectors assigned by methodology presented herein. For ease of

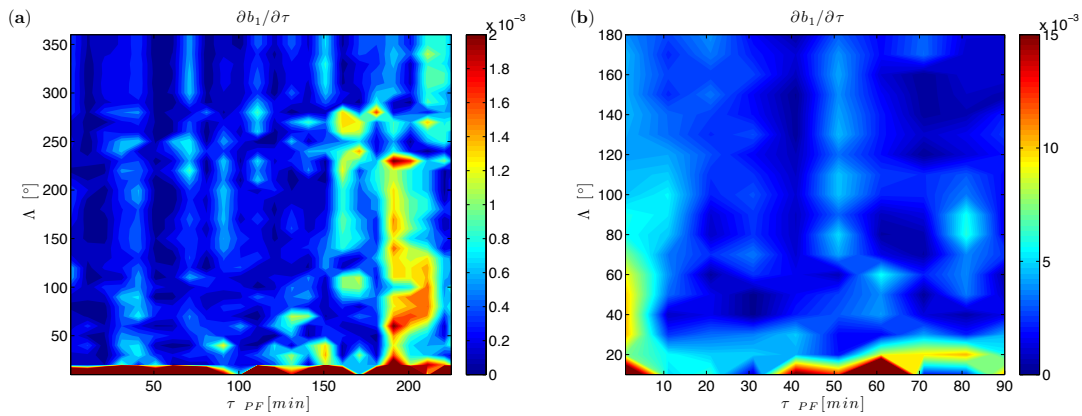

Figure 2.3 – The $\partial b_1/\partial\tau_{pf}$ cost function for (a) PLAYA site for the dominant wind direction sector centred at ϕ =5°, and (b) SLOPE site (right) for the dominant wind direction sector centred at ϕ =85°. The colour data ranges have been rescaled to show details. The original scales for each are: (a) 0 to 0.06 and (b) 0 to 0.05.

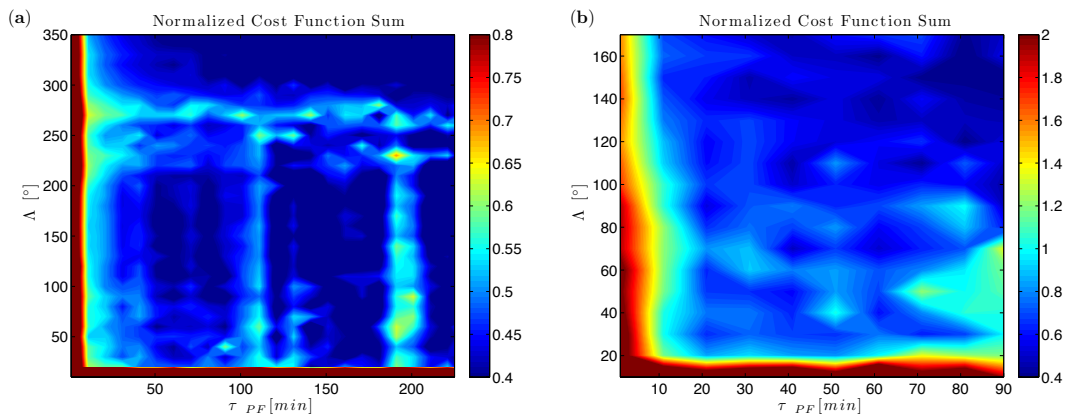

Figure 2.4 – The normalized weighted sum of all seven cost functions for (a) PLAYA site for the dominant wind direction sector centred at ϕ =5°, and (b) SLOPE site for the dominant wind direction sector centred at ϕ =85°. The colour data ranges have been rescaled to show details. The original scales for each are: (a) 0.3 to 4.2 and (b) 0.35 to 4.6.

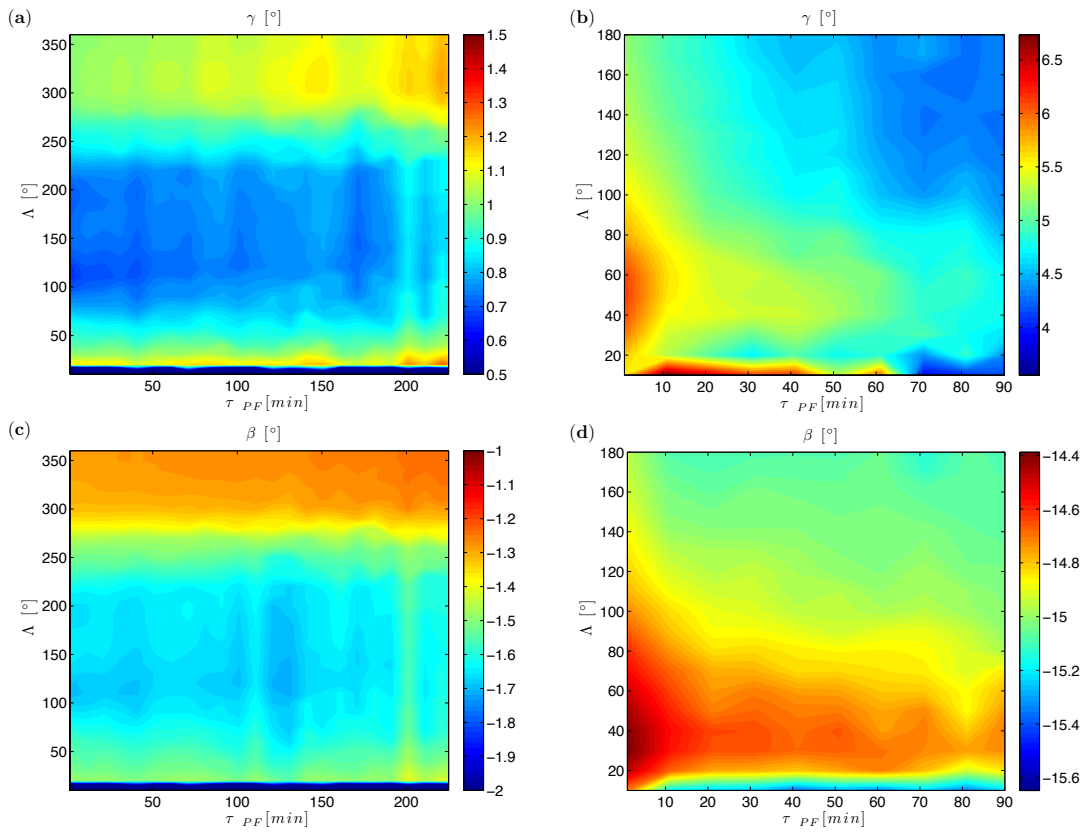

Figure 2.5 – Variation in PF tilt angles, γ, or pitch (top), and β, or roll (bottom), for PLAYA site (left) for the dominant wind direction sector centred at ϕ =5°, and SLOPE site (right) for the dominant wind direction sector centred at ϕ =85°. The colour data ranges for the PLAYA site have been rescaled to show details. The original scales for these panels are: (a) -1.3° to 2.6° and (c) -3.2° to -1.1°.

reference, the sector labels in Fig. 2.6 name the sector (A, B, C...) and show the order in which the sectors were assigned (1 for dominant or 2 for secondary wind directions).

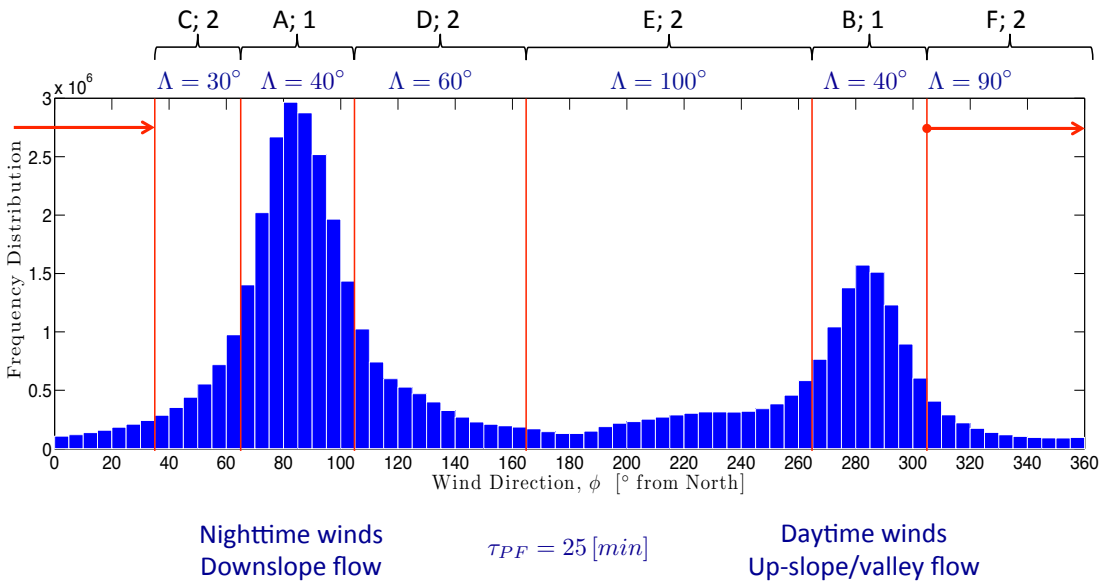

Figure 2.6 – Wind direction histogram and results of the complete cost function analysis for the SLOPE site. The optimal SPF sector assignments are marked by the red vertical lines and the optimal τ_{PF} was found to be 25 min. The labels at the top of each sector indicate the sector name (A, B, C...) for ease in reference and the number indicates the order in which the sectors were defined (1 for dominant wind directions and 2 for the secondary wind directions). In addition, the PF tilt correction angles (γ and β) for each segment are reported at the top of the figure.

The following methodology was the one found most useful and objective for selecting Λ and τ_{PF} for the SLOPE site. However, the cost functions could potentially be used in other ways to select these same SPF parameters.

1. Identify the dominant wind directions (i.e., the peaks in the wind direction histogram). Most sites have at least one or two dominant wind directions. It makes sense to start with the dominant wind directions because they account for the majority of wind vectors, and so the SPF optimization of these sectors should take precedence.

2. For each of the dominant wind directions calculate all the cost functions, and the corresponding cost function sum (weighted or not) for a range of Λ (centred on each of the dominant wind directions) and a range of τ_{PF}. For the SLOPE site example the test ranges used were $10° \leq \Lambda \leq 180°$ with $\Delta\Lambda = 10°$ and 1 min $\leq \tau_{PF} \leq$ 171 min with $\Delta\tau_{PF}$ =10 min.

3. Analyze the fields of the cost functions and the normalized cost function sum looking

for minima. For this analysis recall that for dominant wind directions the smallest reasonable Λ should be used due to the insensitivity of the variability cost functions to large Λ, as previously discussed. Additionally, recall that the selected τ_{PF} must be the same for all SPF sectors, otherwise individual velocity points could be assigned more than one PF tilt due to overlapping averaged segments. Hence, for the analysis of the dominant wind directions the objective is to select a sector size (smallest reasonable) and a range of τ_{PF} that minimize the cost functions.

For example, using Fig. 2.4b and searching for the smallest reasonable Λ, a region between $30° < \Lambda < 60°$ and 20 min $< \tau_{PF} <$ 50 min can be found, which is characterized by a clear minimum. In addition, the resulting PF tilt angles (Figs. 2.5b and d) within this minimization region show low variability between $40° < \Lambda < 60°$ for the same τ_{PF} range. Therefore, $\Lambda = 40°$ and an initial range of 20 min $< \tau_{PF} <$ 50 min were chosen for the wind sector centred at $\phi = 85°$ as shown in Fig. 2.6, sector A. Similarly using the same procedures, $\Lambda = 40°$ and an initial range of 20 min $< \tau_{PF} <$ 50 min were also chosen for the other dominant wind direction centred at $\phi = 285°$ to define sector B in Fig. 2.6. Even though $\Lambda = 40°$ for both dominant wind sectors in the example case, the result is somewhat coincidental and could be different for a different site, or even another measurement height at the same site. In fact, it was expected that the optimal Λ would be slightly smaller for the sector centred at $\phi = 285°$ because the observed daytime wind directions are typically less variable than those observed during the night. Now that the sectors have been assigned for all of the dominant wind directions, the remaining sectors can be assigned. The optimal τ_{PF}, from within the initial minimizing range, can be selected after all SPF sectors are determined, as discussed below.

For the secondary wind direction sectors, the cost function analyses are performed for varied Λ over the remaining, or unassigned, wind direction sectors and the same $\Delta\Lambda$, τ_{PF} range and $\Delta\tau_{PF}$ as were used for the dominant wind direction sectors. The main difference in the cost function analyses for secondary wind direction sectors is in how the Λ test ranges and sector centers are assigned, as enumerated below:

1. The limits for each of the Λ test ranges should be determined. These can be set as the edges of the sectors that were previously defined for the dominant wind directions. For the example data, this means that one of the four secondary test sector ranges starts at $\phi > 105°$ (the upper edge of sector A), increases by $\Delta\Lambda = 10°$ and ends at the maximum $\Lambda = 160°$, which corresponds with $\phi < 265°$, the lower edge of sector B. Hence, the sector centres for the off-wind directions will change with Λ, as opposed to the dominant wind directions, for which the sector centres are constant.

2. Once test ranges have been determined for the secondary directions, the computation and minimization analyses of the cost functions are the same as for the dominant wind directions, recalling that τ_{PF} must be the same for all SPF sectors.

This process should be repeated for all secondary test sectors until all ϕ in the data set have

been assigned to a sector. Finally, the optimal τ_{PF} can be chosen from the initial range depending on the cost function results for all wind direction sectors. If the secondary wind direction sectors do not narrow the initial range, then the shortest τ_{PF} in the initial range should be chosen because it is associated with a larger N. In the example case for the SLOPE site, it was possible to assign all of the secondary sectors (sectors D through F in Fig. 2.6) with these four test ranges, making in total six optimized SPF sectors. However, it may be necessary for other data sets or sites to have more than six sectors if the optimal Λ for the secondary sectors are not large enough to include all remaining ϕ and if N is sufficiently large.

This methodology shows that the optimal sector sizes vary due to variable topography and available data. As Fig. 2.6 shows, typically the optimal sectors for the ϕ in the tails of the distribution have a larger Λ likely because increased N were necessary to improve the PF convergence. This illustrates the competing effects implied by the degrees of freedom for the SPF approach, and that selecting evenly distributed sectors of a single sector size, as typically done for the SPF approach (e.g.,Yuan et al. [2007], Ono et al. [2008], and Nadeau et al. [2013]), may not objectively account for these competing effects. It is important to note (as shown in the cost functions examples for SLOPE vs. PLAYA sites) that the resulting optimization is site-specific, and that the available data at any given site will determine the optimization. For example, the sector labeled C in Fig. 2.6 is relatively small ($\Lambda = 30°$), which likely indicates influences from site heterogeneity caused by some ≈2-3 m high shrubs that run parallel to upper portions of the main slope axis (see Figure 2.1d). These shrubs are located ≈ 50 m north of the main slope axis that intersects with the tower and likely impact streamlines from $\phi \approx 0°$ to 35°. In addition, the PF method requires that sensors are not moved during the time series, and if they are moved throughout the experiment duration, a separate PF or SPF must be performed for the respective data sets [Wilczak et al., 2001]. This implies that seasonal changes in vegetation or surface roughness may also require that a time series might need to be split-up for the PF or SPF methods. In fact at the SLOPE site, SPF tilt-correction angles for the lower sonic anemometers are significantly different for June and July when the alpine grasses are tall and green from those in September and October when the grasses are senescent and shorter (the analysis is not shown herein, but is mentioned as a word of caution). This is one example of how even small differences in terrain (vegetation and topography), can perturb the velocity time series, especially near the surface. However, this significant seasonal difference in tilt-correction angles was not seen in the higher sonic anemometers (at x_3 ≈4 to 6 m) at the SLOPE site probably because they sample larger scale velocities over more terrain and the change in vegetation is not significant enough to perturb the velocities at that scale.

2.6 Resulting momentum fluxes for varied SPF schemes

As stated previously, the sensor tilt corrections have been shown to have a greater effect on the momentum fluxes than on the heat fluxes [Kaimal and Haugen, 1969, Wilczak et al., 2001]. Therefore, to quantify the effects of and sensitivities to non-optimized sensor tilt corrections for varied Λ and τ_{PF}, this section focuses on the resulting momentum fluxes for

varied SPF tilt corrections. The Ogive analyses (Babić et al. [2012]) of the daytime and nighttime turbulent fluxes at the SLOPE site (not shown herein) have indicated that the appropriate flux averaging time, τ_f, that converges fluxes is 30 min; this averaging time is implemented for all flux calculations herein (recall the differences between τ_f and τ_{PF} as detailed in Sec. 2.3.2). Additionally, linear detrending in time of the tilted velocities was implemented before calculating mean and fluctuating components of u_i.

Figure 2.7 shows the differences between the momentum fluxes calculated from a variety of non-optimized SPF tilt corrections and the momentum fluxes calculated from the optimized SPF tilt corrections for the SLOPE site. The legend labels refer to the sector definitions and the τ_{PF}. The sector definitions called 'optimized' refer to the sectors defined by the proposed SPF optimization methodology, and shown in Fig. 2.6; the remaining sector definitions refer to the number of evenly divided/distributed sectors of size Λ (i.e., $36 \times 10°$ means the SPF was performed on 36 evenly distributed, 10° wind sectors). For the test cases with evenly distributed sectors, the sector centres are aligned as much as possible with the dominant wind directions. Figure 2.7a shows a direct comparison scatter plot of momentum fluxes from the varied, non-optimized SPF versus those from the fully optimized SPF shown in Fig. 2.6. Figure 2.7b quantifies the errors between the momentum fluxes from the varied SPF schemes and those from the fully optimized SPF. It shows a segment of the absolute %-difference time series for three consecutive clear-sky days. In general, the errors (absolute %-differences) are lower for clear-sky days. In addition, the times series (Fig. 2.7b) shows that the errors are lower for the daytime fluxes. This is not surprising since the daytime flows are typically stronger and less variable than the nighttime flows. This could also indicate potential wind speed dependence for PF tilt correction schemes, that was not considered in these analyses.

Table 2.1 shows the overall statistics for the complete Sept.-Oct. time series. As expected, a single PF ($1 \times 360°$) performs poorly for the complex SLOPE site. However, surprisingly, selecting small Λ ($36 \times 10°$) results in the highest absolute percent-difference in the momentum fluxes from the optimized SPF. This can be explained by the fact that smaller sector sizes are likely to have a significant percentage of σ_ϕ in each streamline segment that are larger than or fall outside of the sector itself. In fact for this data set, choosing Λ that are too large provides better momentum flux estimates than choosing Λ that are too small. Long τ_{PF} (200 min) also behave poorly because long τ_{PF} coincide with smaller N so fewer representative streamlines are available to define the fitting plane. In addition, long τ_{PF} potentially average over events for which a separate PF might be optimal (potentially non-stationary events). Not surprisingly, the SPF with the 'optimized' sector definitions and with $\tau_{PF} = 45$ min provided momentum fluxes most similar to those from the fully optimized SPF. Recall that 45 min is in the initial range of τ_{PF} from the dominant wind direction sector analyses (see Sect. 2.5 and Fig. 2.4) and was later ruled out based on the secondary wind direction cost function analyses. Hence, the resulting fluxes should be far less sensitive to the τ_{PF} =45 min variation of the SPF. Finally, it is important to reiterate that these results are site specific, and that only the methodologies are transferable to other sites.

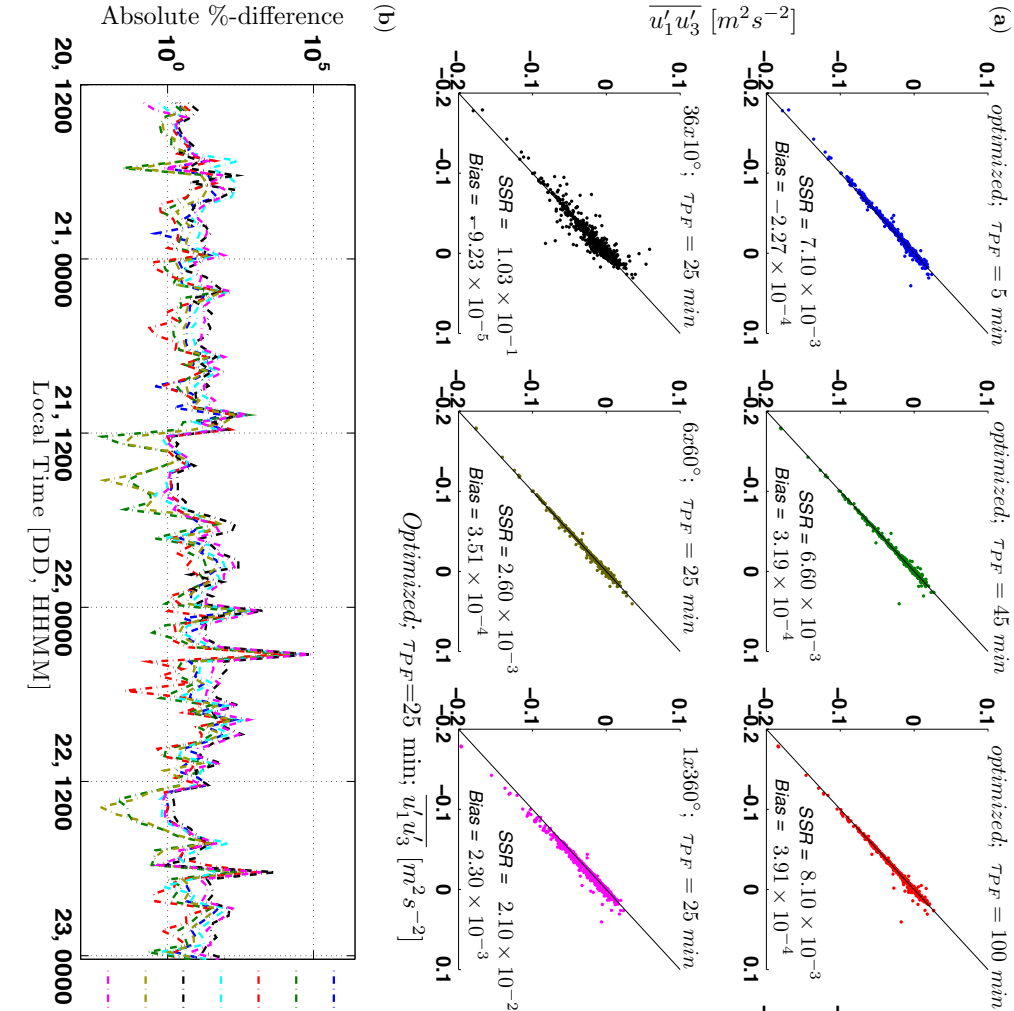

Figure 2.7 – Sensitivity of the momentum fluxes ($\overline{u_1' u_3'}$ or $\overline{u' w'}$) to varied SPF degrees of freedom (see text for more details about the legend labels). The plots show how the momentum fluxes from non-optimized SPF schemes compare to the optimized SPF momentum fluxes: (a) correlations with reporting of the respective biases (mean offsets in [$m^2 s^{-2}$]) and sums of the squared residuals (SSR in [$m^4 s^{-4}$]) and (b) a portion of the absolute %-difference time series for three consecutive clear-sky days. Note the logarithmic scale on panel b.

Table 2.1 – Summary of statistics over the full month of data (1224 total averaged segments with τ_{PF} =25 min.) comparing $\overline{u_1' u_3'}$ resulting from the various SPF parameters for the SLOPE site.

Sector Definition	τ_{PF} [min]	Median Absolute %-diff.	Mean Absolute %-diff.
optimized	25	0	0
optimized	5	8.6	100.4
optimized	45	4.1	50.7
optimized	100	4.6	60.7
optimized	200	12.0	160.1
36 × 10°	25	27.3	422.0
6 × 60°	25	6.5	83.8
1 × 360°	25	21.7	298.6

2.7 Discussions regarding SPF

The SPF methodology presented herein is appropriate for measurements over complex terrain where the streamline-normal velocity component ($\overline{u}_3$) may be non-zero. However in general, the PF and SPF tilt correction approaches have some drawbacks that should be discussed. First, since the PF tilt correction is not a pure rotation technique, the magnitudes of the individual velocity vectors may not be conserved during the tilt correction process. This issue has been discussed (e.g., Sun [2007]), but is typically not quantified or reported. For the SLOPE site this lack of vector conservation before and after the tilt correction was found to be small for the resultants of the velocity vectors (0.15 absolute mean %-difference), especially over the flux averaging time, τ_f. However, for some individual vectors the error is as high as 300%, and since the focus has been on flux measurements, it makes sense to quantify how this error translates to TKE conservation. The mean percent differences for TKE and mean TKE are smaller than for velocity, 0.09% and 0.007%, respectively. Hence, for the SLOPE site this error is acceptable. However, this error is specific to the SLOPE site and the sonic anemometer of interest and should be quantified/verified as a general practice for other data sets. Second, the SPF optimization methodology is not automated, as it requires an objective researcher to analyze the cost functions and make decisions. Furthermore, an automated algorithm may not be possible due to the insensitivities of the cost functions to increased sector size (as discussed above in Sect. 2.3.3) and the fact that the global minima for the cost functions cannot reflect this insensitivity. For example in Fig. 2.4d the true minimum would indicate that Λ should be near 110° and τ_{PF} should be near 120 min. However, this would result in significantly different tilting angles for the sector (see also Fig. 2.5) and would not reduce $\check{u}_i$ adequately. The lack of an automated algorithm makes the SPF optimization methodology inefficient. Future work should include using the optimized SPF methodology to indicate other, more efficiently determinable predictors for the optimal Λ and τ_{PF}. For example, the data from SLOPE site (including those from the other four measurement heights) suggests that the optimal Λ can be predicted by a factor of, $\overline{\sigma}_\phi$, the mean standard deviation in wind direction encompassed

within the sector. This relationship requires future verification with more data from other sites, and a similar predictor is simultaneously needed for the optimal τ_{PF} since $\overline{\sigma}_\phi = f(\Lambda, \tau_{PF})$. Third, the SPF technique inherently generates discontinuities in the tilting angles between wind sectors (Ross and Grant [2014]). The uncertainties that these discontinuities contribute to analyses will depend on the sizes of the discontinuities and the number of affected data points in a particular mean segment. Researchers should at least flag affected mean data segments and consider neglecting these segments if they contribute significantly to the overall mean. Methods to address the discontinuity problems, such as curve fitting the tilt correction angles near the discontinuities or using overlapping SPF segments, should be a topic of future research. Fourth, selecting the best SPF parameters for sectors characterized by very low wind speeds (i.e., above the katabatic layer for downslope flow at the SLOPE site or during transition periods) can be very difficult and unclear with the cost function methodology. This is likely because the streamlines are too weakly characterized to define a good fitting plane. An alternative methodology for very low wind speed sectors should also be considered in future work. Finally, the cost functions defined in Eqs. 2.3-2.5 were written as functions of Λ and τ_{PF}, alone. However, a wind speed or an atmospheric stability dependence on the SPF parameters cannot be ruled out and should also be a topic of future studies.

2.8 Adaptations of the governing flow equations: problem description

Now that the sonic anemometer tilt corrections have been optimized for the complex SLOPE site, the adaptations of the governing flow equations can be addressed. This work focuses on the momentum, velocity variance and TKE budget equations, but the transformations from HV to SNSP coordinate systems presented in Sect. 2.9 are generalized and applicable to other governing equations where gravity plays a role, such as the turbulent flux or the higher order moment prognostic equations. However, prior to showing these adaptations, it is useful to examine the governing flow equations in the HV coordinate system to better assess the complications associated with adapting them to the SNSP system.

For flat terrain, neglecting Coriolis forces near the surface and viscous effects on the mean motions, and employing the shallow convection Boussinesq approximations [Dutton and Fichtl, 1969, Mahrt, 1986], the mean momentum equations are (following Mahrt [1986]):

$$\frac{\partial \bar{\hat{u}}_i}{\partial t} + \bar{\hat{u}}_j \frac{\partial \bar{\hat{u}}_i}{\partial \hat{x}_j} = -\frac{1}{\bar{\rho}_a}\frac{\partial \bar{P}}{\partial \hat{x}_i} - \delta_{i3} g \frac{\Delta\overline{\theta}}{\overline{\theta_a}} - \frac{\partial \overline{\hat{u}_i' \hat{u}_j'}}{\partial \hat{x}_j}, \tag{2.6}$$

where, again employing index notation, $\hat{u}_1$ is the streamwise velocity in the mean flow direction, $\hat{x}_1$, $\hat{u}_2$ is the spanwise velocity in the $\hat{x}_2$ direction, and $\hat{u}_3$ is the vertical velocity in the $\hat{x}_3$ direction; the over bar indicates time averaging, the primes indicate turbulent excursions from the mean and the 'hat' accent above a variable indicates the variable is in the HV coordinate system (see Fig. 2.1c); t is time, ρ_a is the ambient air density at a reference height (note that

hereafter, variables with the subscripted a are taken at the reference level.), P is pressure, δ_{i3} is the Kronecker delta effectuating the acceleration due to gravity, g, in the vertical direction and the buoyancy forces under the above assumptions are generated by the difference in virtual potential temperature, $\Delta\bar{\theta} = \bar{\theta}_a - \bar{\theta}$, from the ambient virtual potential temperature. The momentum equations in the SNSP coordinate system have been presented consistently in the slope flow literature for flows aligned with the main slope (e.g., Manins and Sawford [1979], Mahrt [1982], Haiden and Whiteman [2005] and Nadeau et al. [2013]). This transformation results in modifications to the gravitational term (the fourth term in Eq. 2.6). Since the SNSP coordinate system is no longer aligned with the gravitational force, the vertical projections of the SNSP buoyancy forces must be used. With these transformations the buoyancy term in the u_1 (along slope) component momentum equations is $+g\frac{\Delta\bar{\theta}}{\bar{\theta}_a}\sin(\alpha_{slope})$, and the u_3 (slope normal) component equation now has $-g\frac{\Delta\bar{\theta}}{\bar{\theta}_a}\cos(\alpha_{slope})$ as the buoyancy forcing, where α_{slope} is the main slope angle, and the plus sign for the u_1 component clarifies that the buoyancy force drives the flow, providing positive momentum. This formulation of the momentum equations is suitable for flows aligned with the main slope axis (purely up or down slope flows). However, for slope flows having a cross-slope component (e.g., the daytime thermally driven flows for the SLOPE site are aligned with $\phi = 185°$, or the upslope/upvalley direction) the proper SNSP alignment has gone largely undocumented. A more general form of the momentum equations that will appropriately hold for SNSP coordinate systems aligned with a cross-slope component in $\bar{u}_1$ will be developed in Sect. 2.9.

In addition, the TKE budget equation for slope flows in the SNSP coordinate system has been presented inconsistently in the literature. For flat terrain, the mean TKE budget equation is [Stull, pp. 115–195, 1988],

$$\frac{\partial\overline{e}}{\partial t} + \bar{\hat{u}}_j\frac{\partial\overline{e}}{\partial\hat{x}_j} = +\delta_{i3}\frac{g}{\bar{\theta}}(\overline{\hat{u}_i'\theta'}) - \overline{\hat{u}_i'\hat{u}_j'}\frac{\partial\overline{\hat{u}_i}}{\partial\hat{x}_j} - \frac{\partial(\overline{\hat{u}_j'\overline{e}})}{\partial\hat{x}_j} - \frac{1}{\overline{\rho}}\frac{\partial(\overline{\hat{u}_i'P'})}{\partial\hat{x}_i} - \varepsilon, \tag{2.7}$$

where e is TKE and ε is dissipation rate of TKE. The third term of Eq. 2.7 represents the buoyant production/consumption of TKE, and the δ_{i3} Kronecker delta, again, makes this term act only in the vertical direction. The main discrepancy found in the literature for the SNSP transformation of the TKE budget equation is in the treatment of the buoyant production/destruction term, arising from the physical constraint of the vertical gravitational force. For example, Horst and Doran [1988] and Łobocki [2014] use $-(g/\bar{\theta})(\sin\alpha_{slope}(\overline{u_1'\theta'}) - \cos\alpha_{slope}(\overline{u_3'\theta'}))$, whereas Nadeau et al. [2013] and Arritt and Pielke [1986] use the slope-normal component of buoyancy ($g\overline{u_3'\theta'}/\bar{\theta}$). A third approach might be to use the covariance of the vertical velocity and virtual potential temperature for the buoyancy term, $g(\overline{\hat{u}_3'\theta'})/\bar{\theta}$. However, this potentially limits the possible physical interpretations provided by analyzing the components separately. A plausible reason for these discrepancies/confusions is that TKE is a scalar quantity, and when non-orthogonality exists between the coordinate system and buoyant mechanisms (as in the case of SNSP coordinate systems), it is not readily clear what approach is most appropriate.

The final complication for adapting the governing equations to the SNSP coordinate system for flows over steep, complex terrain is that the streamwise slope angle changes with varying wind direction, ϕ. So the coordinate system and subsequently, the tilt from horizontal of the mean streamline plane change within the time series. This changing coordinate system poses additional difficulties in applying the governing flow equations, especially for the terms associated with gravitational forcing. The following section proposes adaptations that can be used to generalize the governing flow equations, such that transformation to the streamwise SNSP coordinate system for all ϕ becomes clear, and can be used consistently in future research.

2.9 Governing flow equations for slope-aligned coordinate systems

To derive more general forms of the governing flow equations that are easily adaptable for SNSP and other orthogonal coordinate systems requires a more general formulation for gravitational acceleration. The Kronecker delta convention used in Eqs. 2.6 and 2.7 for the HV coordinates makes the quantity $\delta_{i3}g$ for the gravitational acceleration act in only the vertical direction, as expected. However, in a fixed SNSP coordinate system, the directional vectors, $i, j, k = 1, 2, 3$, correspond respectively, to slope-parallel, slope-span and slope-normal directions and the Kronecker delta convention used in the HV forms of the equations no longer correctly applies the gravitational forcing. If instead, a more generalized Kronecker delta convention for the gravitational acceleration is used, the proper projections of the buoyancy forces can be made for all directions, x_i, in the SNSP coordinate system. This more general form of the Kronecker delta convention is

$$-g(\delta_{i1} sin\alpha_1 + \delta_{i2} sin\alpha_2 - \delta_{i3} cos\alpha_3). \tag{2.8}$$

Equation 2.8 shows three different slope angles: α_1, α_2 and α_3. The slope angles α_1 and α_2 are defined as the angles from the horizontal aligned with x_1 and x_2, respectively and assuming that x_1 and u_1 follow the mean wind, can change with changing wind direction (i.e., the angles of the terrain 'seen' by the mean wind, u_1 and u_2). Park and Park [2006] also observe this changing slope angle over larger scales. The slope angle α_3 is defined as the angle between the planar slope-normal direction, x_3, and the vertical direction, and is a constant angle (assuming a planar slope) that represents the main planar tilt of the terrain. Since α_1 and α_2 change with wind direction (in a coordinate system aligned with the mean wind direction), a convention relating wind direction to the sloping plane must first be defined and established to generalize the mathematical definitions of α_i for any slope aspect. This generalized wind direction, ψ, is defined by a clockwise wind direction compass aligned with zero at the top of the slope, such that for pure downslope flow, $\psi = 0° = 360°$ and for pure upslope flow $\psi = 180°$. Hence to transform the SNSP forms of the equations developed herein to any site, all that is needed is a site-specific relationship between ψ, the generalized, slope-referenced wind direction and ϕ, the meteorological wind direction defined from north. For example, $\psi = \phi - 90°$ for the west-facing SLOPE site, where northerly winds blow cross-slope from left to right when

looking up from the base of the slope. Subsequently, assuming a planar slope α_1 and α_2 are:

$$\alpha_1 = \arcsin(\cos\psi \sin\alpha_3) \tag{2.9}$$

and

$$\alpha_2 = \arcsin(\cos(\psi - 90)\sin\alpha_3). \tag{2.10}$$

Figure 2.8 shows an example schematic of how ψ, ϕ and α_i are defined for a west-facing, planar slope of $\alpha_{slope} = 35.5° = \alpha_3$ (an idealization of the SLOPE site). If the planar-slope assumption is not reasonable for a particular site, then $\alpha_{1,2,3} = f(\phi)$ can alternatively come from a high-resolution digital elevation model (DEM) with advanced geographic information system (GIS) tools. To evaluate the planar slope assumption for the SLOPE site, Fig. 2.9 shows the elevation profiles for the $\phi = 90°$ and $\phi = 285°$ meteorologic wind directions for the SLOPE site. By visual inspection, the slope near the tower appears to be quite uniform and locally, the planar slope assumption seems reasonable. To better quantify this assumption, the local slope angles given in the inset of Fig. 2.9 were estimated from a 10 m by 10 m grid taken from a 1 m resolution DEM and centred at the measurement tower. The local slope angle for $\phi = 285°$, $\alpha = 33.6°$, is reasonably close to the mathematically derived (Eq. 2.9), planar slope angle, $\alpha = 34.1°$. Table 2.2 summarizes the departures in local α_1 slope angles for various ϕ, determined by comparing estimates from the DEM at the SLOPE site and the theoretical slope angles assuming a purely planar slope. For most wind directions at the SLOPE site, this departure is minimal, especially for the dominant wind directions (the first two rows in Tab. 2.2). The largest percent difference, 100%, is for the purely cross-slope wind direction ($\phi = 0°$) because the theoretical slope angle is zero and the DEM slope angle is not zero. The next largest percent difference, 18.6%, would add significant uncertainly to buoyancy flux estimates for wind directions $\phi = 20°$ or $\phi = 200°$. However, the wind from these directions happen to occur infrequently at the SLOPE site (see Fig. 2.6).

Substituting the generalized Kronecker delta convention (Eq. 2.8) into the gravitational term for Eq. 2.6 gives the generalized mean momentum equations,

$$\frac{\partial \bar{u}_i}{\partial t} + \bar{u}_j \frac{\partial \bar{u}_i}{\partial x_j} = -\frac{1}{\bar{\rho}_a}\frac{\partial \bar{P}}{\partial x_i} + \frac{\Delta\theta g}{\bar{\theta}_a}(\delta_{i1} sin\alpha_1 + \delta_{i2} sin\alpha_2 - \delta_{i3} cos\alpha_3) - \frac{\partial \overline{u_i' u_j'}}{\partial x_j}. \tag{2.11}$$

To compare with the slope-aligned forms of the mean momentum equations in the literature for pure downslope flow, requires that $\alpha_1 = \alpha_3 = \alpha_{slope}$ and $\alpha_2 = 0$. With these slope angles, $\sin\alpha_2 = 0$ and the standard forms of the u_1 and u_3 momentum balances given in Manins and Sawford [1979], Mahrt [1982] and others are recovered. In addition, Eq. 2.11 is now also appropriate for slope flows having a cross slope component, a topic that has gone largely undocumented. For example, at the SLOPE site the dominant daytime wind direction is $\phi = 285°$ (upslope/upvalley flow), making $\psi = 195°$ and $\alpha_1 = -34.1°$. As opposed to the pure downslope flow case, $\alpha_1 \neq \alpha_3$, and the local gravitational forcing in the u_1 mean momentum

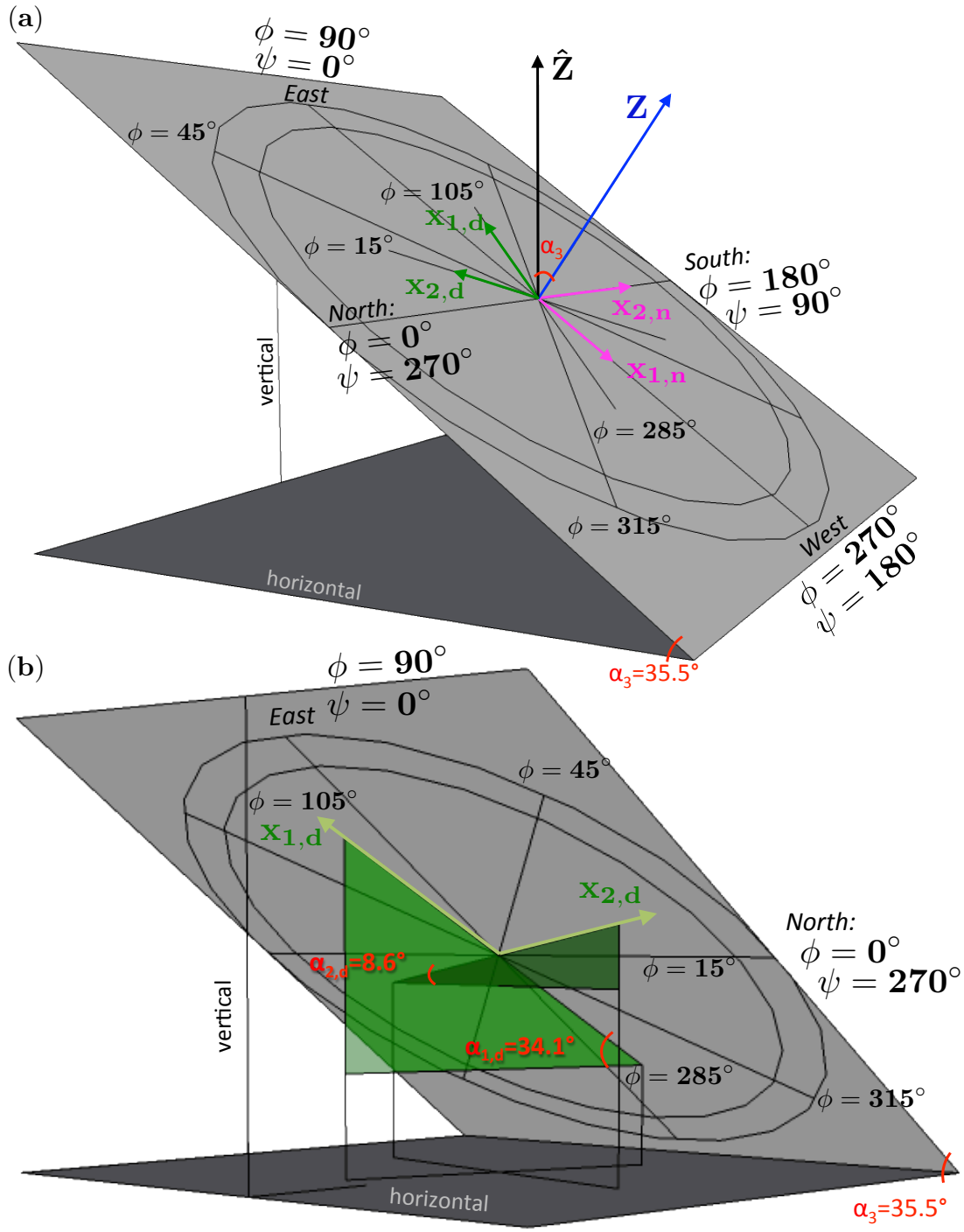

Figure 2.8 – Idealized planar slope schematic for a west-facing ($\psi = \phi - 90°$) slope with $\alpha_3 = 35.5°$. (a) The front side of the slope showing the dominant wind directions for night (downslope flow; $\phi = 90°$; magenta vectors, $x_{1,n}$, $x_{2,n}n$) and day (upslope/upvalley flow; $\phi = 285°$; green vectors, $x_{1,d}$, $x_{2,d}$). (b) The back, or underside, of the slope showing α_1 and α_2 for $\phi = 285°$, a wind direction not aligned with the main slope angle.

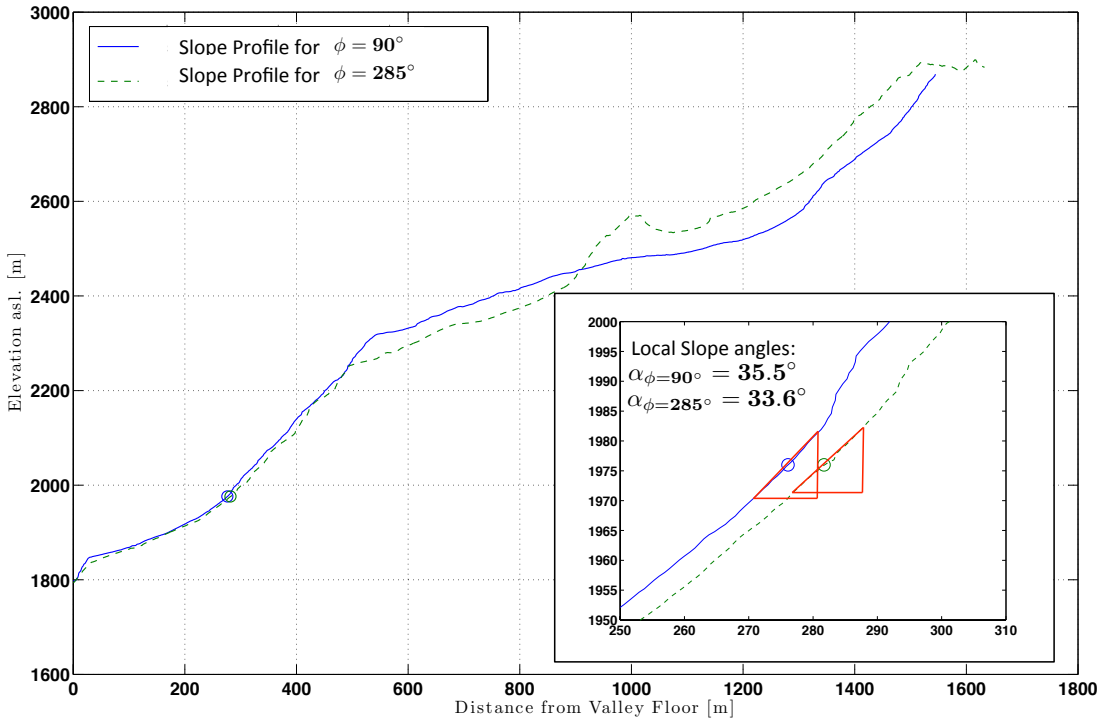

Figure 2.9 – Elevation profiles from the valley floor to the ridge top for the $\phi = 90°$ and $\phi = 285°$ wind directions at the SLOPE site. The circles indicate the measurement tower location at 1976 m asl., where the two profiles intersect. The inset shows a zoomed-in region near the tower and the local slope angles that were estimated from a 1 m resolution digital elevation map over 10 m by 10 m grid centred at the tower.

Table 2.2 – Magnitudes of the terrain slope angles estimated from the DEM at the SLOPE site, and determined theoretically assuming a perfectly planar slope with $\alpha_3 = 35.5°$ for various wind directions, and percent differences of the sine of these angles calculated by $100(\sin|\alpha_{1,DEM}| - \sin|\alpha_{1,TH}|)/\sin|\alpha_{1,DEM}|$.

ϕ	$\lvert\alpha_{1,DEM}\rvert$	$\lvert\alpha_{1,TH}\rvert$	%-difference
90°, 270°	35.5°	35.5°	0
105°, 285°	33.6°	34.1°	-1.3
0°, 180°	1.05°	0°	100
20°, 200°	14.2°	11.5°	18.6
40°, 220°	22.1°	21.9°	0.8
45°, 135°	27.5°	24.2°	11.2
60°, 240°	32.1°	30.2°	5.5
80°, 260°	35.1°	34.5°	1.4
120°, 300°	31.8°	30.2°	4.5
140°, 320°	20.9°	21.9°	-4.6
160°, 340°	10.3°	11.5°	-11.5

balance is slightly reduced due to the reduced slope angle 'seen' by the mean wind.

Similarly for the TKE budget equation, one could simply insert the generalized Kronecker delta convention (Eq. 2.8) to obtain the SNSP appropriate adaptations. However, since documented discrepancies have characterized the SNSP form of the TKE budget equation, a more complete derivation is presented here. TKE is defined as [Stull, pp. 115–195, 1988]:

$$\overline{e} = 0.5\overline{u_i'^2}. \tag{2.12}$$

From Eq. 2.12 and also following Stull [pp. 115–195, 1988], to derive the TKE budget equation requires summing the prognostic equations for velocity variances and dividing by 2. The prognostic equations for velocity variances [Stull, pp. 115–195, 1988],

$$\frac{\partial \overline{\hat{u}_i'^2}}{\partial t} + \overline{\hat{u}}_j \frac{\partial \overline{\hat{u}_i'^2}}{\partial \hat{x}_j} = +2\delta_{i3}\frac{g\overline{(\hat{u}_i'\theta')}}{\overline{\theta}} - 2\overline{\hat{u}_i'\hat{u}_j'}\frac{\partial \overline{\hat{u}_i}}{\partial \hat{x}_j} - \frac{\partial \overline{(\hat{u}_j'\hat{u}_i'^2)}}{\partial \hat{x}_j} - \frac{2}{\overline{\rho}}\frac{\partial \overline{(\hat{u}_i'P')}}{\partial \hat{x}_i} - 2\varepsilon, \tag{2.13}$$

was derived for a HV coordinate system as indicated by the Kronecker delta convention in the third term. In the SNSP coordinate system, each of the three components of the velocity variance can potentially have a contribution from buoyant forcing. To account for these contributions, the more generalized Kronecker delta formulation (Eq. 2.8) is used, and then Eq. 2.13 can be written for the SNSP system without violating the physical law of gravity acting vertically. With these substitutions, Eq. 2.13 is now,

$$\begin{aligned}\frac{\partial \overline{u_i'^2}}{\partial t} + \overline{u}_j \frac{\partial \overline{u_i'^2}}{\partial x_j} = -2\delta_{i1} sin\alpha_1 \frac{g\overline{(u_i'\theta')}}{\overline{\theta}} - 2\delta_{i2} sin\alpha_2 \frac{g\overline{(u_i'\theta')}}{\overline{\theta}} + 2\delta_{i3} cos\alpha_3 \frac{g\overline{(u_i'\theta')}}{\overline{\theta}} \\ -2\overline{u_i'u_j'}\frac{\partial \overline{u}_i}{\partial x_j} - \frac{\partial \overline{(u_j'u_i'^2)}}{\partial x_j} - \frac{2}{\overline{\rho}}\frac{\partial \overline{(u_i'P')}}{\partial x_i} - 2\varepsilon.\end{aligned} \tag{2.14}$$

If now Eq. 2.14 is substituted into the definition for mean TKE, $2\overline{e} = \overline{u_i'^2}$ (Eq. 2.12), the TKE budget equation for a general, planar-slope coordinate system is,

$$\begin{aligned}\frac{\partial \overline{e}}{\partial t} + \overline{u}_j \frac{\partial \overline{e}}{\partial x_j} = -sin\alpha_1 \frac{g\overline{(u_1'\theta')}}{\overline{\theta}} - sin\alpha_2 \frac{g\overline{(u_2'\theta')}}{\overline{\theta}} + cos\alpha_3 \frac{g\overline{(u_3'\theta')}}{\overline{\theta}} \\ -\overline{u_i'u_j'}\frac{\partial \overline{u}_i}{\partial x_j} - \frac{\partial \overline{(u_j'\overline{e})}}{\partial x_j} - \frac{1}{\overline{\rho}}\frac{\partial \overline{(u_i'P')}}{\partial x_i} - \varepsilon.\end{aligned} \tag{2.15}$$

For flat terrain, $\alpha_1 = \alpha_2 = \alpha_3 = 0$ and the flat terrain form of the TKE budget equation (Eq. 2.7) is recovered. Theoretically for a planar slope, all three components of the buoyancy term must be kept. To our knowledge, the α_2 buoyancy term has not been shown in the literature. This oversight is probably explained by two reasons. First, when $\bar{u}_1$ is rotated into the mean wind direction, $\bar{u}_2 = 0$ so it is easy to overlook any contributions from u_2'. The second reason can be explained using the magenta vectors ($x_{i,n}$) sketched in Fig. 2.8 for pure downslope flow. In this

case, $\alpha_1 = \alpha_3 = \alpha_{slope} = 35.5°$ and $\alpha_2 = 0°$ so $(g/\bar{\theta})(-\overline{u_2'\theta'}\sin\alpha_2) = 0$, and the formulations in Horst and Doran [1988] and Łobocki [2014] are recovered. However, pure up or down slope flows are special cases and for a wind direction not aligned with the main slope axis (i.e., the green vectors in Fig. 2.8, $x_{i,d}$) $\sin\alpha_2 \neq 0$ and $(g/\bar{\theta})(-\overline{u_2'\theta'}\sin\alpha_2)$ is also not necessarily equal to zero. Since it is unclear from the theoretical formulations if the α_2 component of the buoyancy term is significant with respect to the other two components, Fig. 2.10 uses the data from the SLOPE site to investigate this question. Figure 2.10a shows all three buoyancy components from the TKE budget equation for three consecutive clear-sky days. Figure 2.10b shows the corresponding time series of their respective slope angles on the left, blue axis and the wind direction angles, ϕ and ψ on the right, grey axis for reference. Above all, Fig. 2.10 shows that except in the case of pure downslope flow, for example at night, all three components of the buoyancy term can be significant and should be retained in TKE budget analyses. In this example, the $(g/\bar{\theta})(-\overline{u_2'\theta'}\sin\alpha_2)$ term contributes little to the vertical buoyancy flux; However, it is nonzero. This implies that for a SNSP coordinate systems for which u_1 follows the mean wind direction, the $(g/\bar{\theta})(-\overline{u_2'\theta'}\sin\alpha_2)$ term is potentially significant for some sites, and should not be neglected *a priori*. In addition, Fig. 2.10a shows that the resultant buoyancy flux computed by summing the three flux components is equivalent to the buoyancy flux computed by using the vertical velocity component, $\overline{\hat{u}_3'\theta'}$, as expected (note the 'hat' notation for the HV coordinate system). Using the vertical velocity component to calculate the total buoyancy flux, $g/\bar{\theta}_v\overline{\hat{u}_3'\theta'}$, may seem like a more simple formulation to use. However, using the three components can elucidate a richness of information regarding physical mechanisms because it unfolds how fluxes over sloping terrain differ from their flat terrain counterparts. For example, since the along slope buoyancy fluxes are now aligned with the momentum fluxes one can explore how the two interact. These results also have implications for the flux Richardson number, Ri_f, that is defined as the ratio of shear production terms to the buoyant production/destruction terms from the TKE budget equation. Therefore, in a SNSP coordinate system, the flux Richardson number is

$$Ri_f = \frac{\frac{g}{\bar{\theta}}(-sin\alpha_1\overline{u_1'\theta'} - sin\alpha_2\overline{u_2'\theta'} + cos\alpha_3\overline{u_3'\theta'})}{\overline{u_i'u_j'}\frac{\partial\overline{U_i}}{\partial x_j}} = \frac{\frac{g}{\bar{\theta}}\overline{\hat{u}_3'\theta'}}{\overline{u_i'u_j'}\frac{\partial\overline{U_i}}{\partial x_j}}. \tag{2.16}$$

These results show that in using the SNSP coordinate system the buoyancy terms in the governing equations must retain extra terms. In addition, when x_1 and $\bar{u}_1$ follow the mean wind direction the physical interpretations of the buoyancy fluxes in the TKE budget equation become more complicated because α_1 and α_2 are changing in magnitude and sign throughout a diurnal cycle. Therefore, in future studies where a planar slope assumption is reasonable, it is recommended that a *fixed* SNSP coordinate system is adopted. In such a case, x_1 and $\bar{u}_1$ are not rotated into the mean wind direction and are aligned with the main slope axis. Hence, $\bar{u}_2 \neq 0$, necessarily, and x_2 and $\bar{u}_2$ are aligned with the cross-slope direction. For the fixed SNSP coordinate system the general SNSP forms of the governing equations derived herein remain valid and $\alpha_1 = \pm\alpha_3 = \alpha_{slope}$ and $\alpha_2 = \sin\alpha_2 = 0$, which is a significant simplification

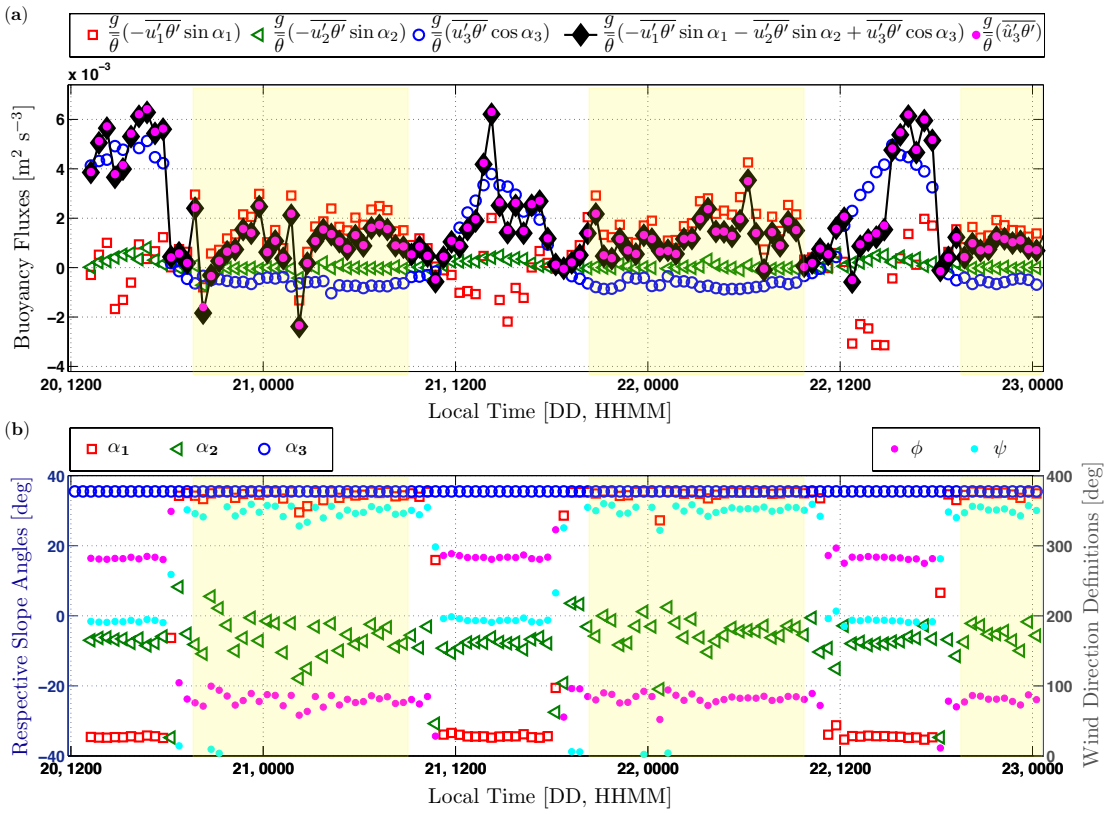

Figure 2.10 – Three consecutive clear-sky diurnal cycles showing (a) SNSP components of the buoyancy flux from Eq. 2.15 and the resultant buoyancy flux computed by two equivalent methods, summing the SNSP components and using the vertical velocity component and (b) the respective slope angles (blue, left axis) for each component. For reference, the corresponding time series of wind direction angles, ϕ and ψ are also shown (grey, right axis). The shaded regions indicate the nighttime, downslope flow regimes. Note the diurnal sign changes in α_1 corresponding to the diurnal changes in ϕ (see also Fig. 2.6).

when analyzing the buoyancy fluxes in the TKE budget. However, care must be taken to ensure that the signs for α_1 align properly with the fixed coordinate system chosen. For example, if positive x_1 is aligned with the upslope direction, then $\alpha_1 = -\alpha_3$. Conversely, if positive x_1 is aligned with the downslope direction, then $\alpha_1 = \alpha_3$ for the equations herein to produce the correct signs. One disadvantage associated with using a fixed SNSP coordinate system, is that analysis of the momentum budget becomes more complicated because the $\bar{u}_2$ component of the momentum balance equations must be retained for flows not aligned with the dominant slope axis.

2.10 Summary and Conclusions

In this paper, solutions for addressing some of the challenges associated with adapting field data and the governing flow equations to coordinate systems aligned with steep slopes in three-dimensional complex terrain have been proposed and developed for practical use. First, to reduce the artificial, terrain-induced portion of the measured velocity signal, $\check{u}_i$, a methodology is developed that provides objective cost functions for selecting appropriate sectors sizes, Λ, and planar fit averaging time τ_{PF} for the sector-wise planar fit (SPF) tilt correction scheme. Through the ensemble minimization of these cost functions an optimized SPF helps to place the 3D velocity measurements into a more planar, terrain-following coordinate system. Field data from an alpine, steep slope site show that significant deviations from the optimized SPF can produce large errors in the momentum flux estimates as shown in Fig. 2.7 and summarized in Table 2.1. In particular, some of the highest errors in the momentum fluxes are produced by using small Λ (422% mean absolute percent difference for $\Lambda = 10°$) or very long τ_{PF} (160% mean absolute percent difference for τ_{PF} =200 min) for the SPF because the data segments defining each PF contain too much variability such that the mean streamlines are not representative of observed velocity signals. In addition, using a single PF also performed poorly because of the geometrically variable terrain surrounding the SLOPE site. The cost functions also show that for the very idealized, flat site (PLAYA) a single planar fit is likely sufficient because the PF coefficients, and subsequent PF tilt angles, do not change much for varying Λ and τ_{PF}, except for very long τ_{PF}.

Second, simplifications, inconsistencies and oversights found in the slope flow literature that can be associated with improper treatment of the buoyancy terms for the governing flow equations in the slope-normal/slope-parallel (SNSP) coordinate system are addressed. New and generalized adaptations for the governing flow equations are developed for slope-aligned coordinate systems. In particular, these SNSP forms of mean momentum equations can properly account for a coordinate system changing in time to follow the terrain in the mean wind direction and hence, a slope flow that is not aligned with the main slope axis (i.e., has a cross-slope component). In such cases, the buoyancy forces are reduced in the streamwise ($\bar{u}_1$ component) equation because the real slope angle 'seen' by $\bar{u}_1$ is less steep than the angle experienced by pure upslope or downslope flows. In addition, a generalized, terrain-following, TKE budget equation is derived that is appropriate for orthogonal, planar

coordinate systems. Therefore, it is appropriate for both flat and sloping terrain if the x_3 and $\bar{u}_3$ components are aligned with the surface-normal direction. This equation contains all three directional contributions to the buoyancy flux and therefore, the buoyant production/destruction term of the full budget equation. Data from the SLOPE site show that the typically omitted $\sin(\alpha_2)g\overline{(u_2'\theta')}/\bar{\theta}$ component of the buoyancy flux was found to be nonzero for slope flows having a cross slope component, and should not necessarily be neglected. Subsequently for these cases, the flux Richardson number must also contain all three components. For pure upslope or downslope flows this term is zero because $\alpha_2 = 0$, and the Horst and Doran [1988] and Łobocki [2014] formulations are sufficient.

In summary, this paper is motivated by a need to revisit traditional methodologies for more complex measurements sites. The results presented herein are largely site specific, though the methodologies and especially the derivations are adaptable to other sites. The standardization of methodologies for properly handling atmospheric measurements over very complex sites is still in the developmental stage. Even the optimized SPF scheme presented herein has some imperfections that researchers should seek to address, such as discontinuities in tilting angles, problems fitting a plane to very low wind speed sectors, efficiency in selecting optimized SPF parameters, wind speed dependence on the SPF parameters, and velocity vector conservation. However, this SPF scheme is an important step toward improved and standardized methodologies because it offers a clear technique with which more objective decisions can be made for SPF implementations over complex terrain.

Acknowledgements

This research was primarily funded by the Swiss National Science Foundation (SNSF-200021-134892) and the Competence Center for Environmental Sustainability (CCES-SwissEx) of the ETH domain. This work was partially supported by the United States Office of Naval Research, Award #N00014–11–1–0709. The authors wish to thank Dr. Evgeni Fedorovich, Dr. Nikki Vercauteren and Marco Giometto for lively and helpful discussions regarding the subject matter of this paper, and to Derek Jensen of the MATERHORN campaign for assistance with the PLAYA data set. Thanks go also to our colleagues from the EFLUM laboratory for great assistance in the Val Ferret field campaign, especially Raphael Mutzner who also helped with GIS support. Finally, special thanks to the Commune d'Orsières for general logistical support for field campaigns in Val Ferret.

Bibliography

R W Arritt and R A Pielke. Interactions of nocturnal slope flows with ambient winds. *Boundary-Layer Meteorol*, 37(1):183–195, 1986.

K Babić, Z Bencetić Klaić, and Ž Večenaj. Determining a turbulence averaging time scale by Fourier analysis for the nocturnal boundary layer. *Geofizika*, 29(1):35–51, 2012.

D D Baldocchi, J J Finnigan, K Wilson, K T Paw U, and E Falge. On measuring net ecosystem carbon exchange over tall vegetation on complex terrain. *Boundary-Layer Meteorol*, 96(1-2): 257–291, 2000.

M A Carper and F Porté-Agel. The role of coherent structures in subfilter-scale dissipation of turbulence measured in the atmospheric surface layer. *J Turbul*, 5:32–32, 2004.

Y Cheng, M B Parlange, and W Brutsaert. Pathology of Monin-Obukhov similarity in the stable boundary layer. *J Geophys Res*, 110(D6):D06101, 2005.

A Christen, E Van Gorsel, R Vogt, M Andretta, and M W Rotach. Ultrasonic anemometer instrumentation at steep slopes wind tunnel study-field intercomparison-measurements. *MAP Meeting Schliersee (MAP newsletter)*, 15:206–209, 14–16 May 2001.

J A Dutton and G H Fichtl. Approximate equations of motion for gases and liquids. *J Atmos Sci*, 26(2):241–254, 1969.

C Feigenwinter, C Bernhofer, U Eichelmann, B Heinesch, M Hertel, D Janous, O Kolle, F Lagergren, A Lindroth, S Minerbi, U Moderow, M Mölder, L Montagnani, R Queck, C Rebmann, P Vestin, M Yernaux, M Zeri, W Ziegler, and M Aubinet. Comparison of horizontal and vertical advective CO2 fluxes at three forest sites. *Agr Forest Meteorol*, 148(1):12–24, 2008.

H J S Fernando and E R Pardyjak. Field studies delve into the intricacies of mountain weather. *Eos Trans AGU*, 94(36):313–315, 2013.

H J S. Fernando, E R Pardyjak, S Di Sabatino, F K Chow, S F J De Wekker, S W Hoch, J Hacker, J C Pace, T Pratt, Z Pu, J W Steenburgh, C D Whiteman, Y Wang, D Zajic, B Balsley, R Dimitrova, G D Emmitt, C W Higgins, J C R Hunt, J G Knievel, D Lawrence, Y Liu, D F Nadeau, E Kit, B W Blomquist, P Conry, R S Coppersmith, E Creegan, M Felton, A Grachev, N Gunawardena, C Hang, C M Hocut, G Huynh, M E Jeglum, D Jensen, V Kulandaivelu, M Lehner, L S Leo,

D Liberzon, J D Massey, K McEnerney, S Pal, T Price, M Sghiatti, Z Silver, M Thompson, H Zhang, and T Zsedrovits. The MATERHORN – Unraveling the intricacies of mountain weather. *B Am Meteorol Soc*, 2015 *in press*.

Thomas Foken. *Micrometeorology*. Springer, 2008.

P Geissbühler, R Siegwolf, and W Eugster. Eddy covariance measurements on mountain slopes: the advantage of surface-normal sensor orientation over a vertical set-up. *Boundary-Layer Meteorol*, 96(3):371–392, 2000.

T Haiden and C D Whiteman. Katabatic flow mechanisms on a low-angle slope. *J Appl Meteorol*, 44(1):113–126, 2005.

C W Higgins, C Meneveau, and M B Parlange. The effect of filter dimension on the subgrid-scale stress, heat flux, and tensor alignments in the atmospheric surface layer. *J Atmos Ocean Tech*, 24(3):360–375, 2007.

C W Higgins, C Meneveau, and M B Parlange. Geometric alignments of the subgrid-scale force in the atmospheric boundary layer. *Boundary-Layer Meteorol*, 132(1):1–9, 2009.

T W Horst and J C Doran. The turbulence structure of nocturnal slope flow. *J Atmos Sci*, 45(4): 605–616, 1988.

N Hutchins and I Marusic. Evidence of very long meandering features in the logarithmic region of turbulent boundary layers. *J Fluid Mech*, 579:1–28, 2007.

D D Jensen, D F Nadeau, S W Hoch, and E R Pardyjak. Observations of near-surface heat flux and temperature profiles through the early evening transition over contrasting surfaces. *Boundary-Layer Meteorol*, 2015 *in press*.

J C Kaimal and J J Finnigan. *Atmospheric Boundary Layer Flows: Their Structure and Measurement*. Oxford University Press, 1994.

J C Kaimal and D A Haugen. Some errors in the measurement of Reynolds stress. *J Appl Meteorol*, 8(3):460–462, 1969.

J C Klewicki, M M Metzger, E Kelner, and E M Thurlow. Viscous sublayer flow visualizations at $R_\theta \cong 1\,500\,000$. *Phys Fluids*, 7(4):857–863, 1995.

G J Kunkel and I Marusic. Study of the near-wall-turbulent region of the high-Reynolds-number boundary layer using an atmospheric flow. *J Fluid Mech*, 548:375–402, 2006.

X Lee. On micrometeorological observations of surface-air exchange over tall vegetation. *Agr Forest Meteorol*, 91(1):39–49, 1998.

X Lee, W J Massman, and B E Law. *Handbook of Micrometeorology: A Guide for Surface Flux Measurement and Analysis*, volume 29. Springer, 2006.

M Li, W Babel, K Tanaka, and T Foken. Note on the application of planar-fit rotation for non-omnidirectional sonic anemometers. *Atmos Meas Tech*, 6:221–229, 2013.

L Łobocki. Surface-layer flux–gradient relationships over inclined terrain derived from a local equilibrium, turbulence closure model. *Boundary-Layer Meteorol*, 150(3):469–483, 2014.

A Lorke, D F McGinnis, and A Maeck. Eddy-correlation measurements of benthic fluxes under complex flow conditions: Effects of coordinate transformations and averaging time scales. *Limnol Oceanogr Methods*, 11:425–437, 2013.

L Mahrt. Momentum balance of gravity flows. *J Atmos Sci*, 39:2701–2711, 1982.

L Mahrt. On the shallow motion approximations. *J Atmos Sci*, 43(10):1036–1044, 1986.

P C Manins and B L Sawford. A model of katabatic winds. *J Atmos Sci*, 36:619–630, 1979.

M M Metzger, B J McKeon, and H A Holmes. The near-neutral atmospheric surface layer: turbulence and non-stationarity. *Philos T Roy Soc A*, 365(1852):859–876, 2007.

R Mutzner, E Bertuzzo, P Tarolli, S V Weijs, L Nicotina, S Ceola, N Tomasic, I Rodriguez-Iturbe, M B Parlange, and A Rinaldo. Geomorphic signatures on Brutsaert base flow recession analysis. *Water Resour Res*, 49(9):5462–5472, 2013.

D F Nadeau, E R Pardyjak, C W Higgins, and M B Parlange. Similarity scaling over a steep alpine slope. *Boundary-Layer Meteorol*, 147(3):401–419, 2012.

D F Nadeau, E R Pardyjak, C W Higgins, H Huwald, and M B Parlange. Flow during the evening transition over steep alpine slopes. *Q J Roy Meteorol Soc*, 139(672):607–624, 2013. ISSN 1477-870X. doi: 10.1002/qj.1985. URL http://dx.doi.org/10.1002/qj.1985.

H J Oldroyd, G Katul, E R Pardyjak, and M B Parlange. Momentum balance of katabatic flow on steep slopes covered with short vegetation. *Geophys Res Lett*, 41(13):4761–4768, 2014.

K Ono, M Mano, A Miyata, and Y Inoue. Applicability of the planar fit technique in estimating surface fluxes over flat terrain using eddy covariance. *J Agr Meteorol (Japan)*, 64:121–130, 2008.

M Park and S Park. Effects of topographical slope angle and atmospheric stratification on surface-layer turbulence. *Boundary-Layer Meteorol*, 118(3):613–633, 2006.

A N Ross and R Grant. Flux measurements in complex, forested terrain. In *21st Symposium on Boundary Layers and Turbulence*. American Meteorology Society, 9–13 June 2014.

W Shamarock, J B Klemp, J Dudhia, D O Gill, D M Barker, M G Duda, X Y Huang, W Wang, and J G Powers. A description of the advanced research WRF version 3. *NCAR technical note NCAR/TN/u2013475*, 2008.

S Simoni, S Padoan, D F Nadeau, M Diebold, A Porporato, G Barrenetxea, F Ingelrest, M Vetterli, and M B Parlange. Hydrologic response of an alpine watershed: Application of a meteorological wireless sensor network to understand streamflow generation. *Water Resour Res*, 47 (W10524):W10524, 2011.

I Stiperski and M W Rotach. i-box: Studying boundary layers in very complex terrain. In *21st Symposium on Boundary Layers and Turbulence*. American Meteorology Society, 9–13 June 2014.

R B Stull. *An Introduction to Boundary Layer Meteorology*. Kluwer Academic publishers, pp. 115–195, 1988.

J Sun. Tilt corrections over complex terrain and their implication for CO2 transport. *Boundary-Layer Meteorol*, 124(2):143–159, 2007.

D Vickers and L Mahrt. A solution for flux contamination by mesoscale motions with very weak turbulence. *Boundary-Layer Meteorol*, 118(3):431–447, 2005.

D Vickers and L Mahrt. Contrasting mean vertical motion from tilt correction methods and mass continuity. *Agr Forest Meteorol*, 138(1):93–103, 2006.

J M Wilczak, S P Oncley, and S A Stage. Sonic anemometer tilt correction algorithms. *Boundary-Layer Meteorol*, 99(1):127–150, 2001.

M Xue, K K Droegemeier, V Wong, A Shapiro, K Brewster, F Carr, D Weber, Y Liu, and D Wang. The Advanced Regional Prediction System (ARPS)–A multi-scale nonhydrostatic atmospheric simulation and prediction tool. Part II: Model physics and applications. *Meteorol Atmos Phys*, 76(3-4):143–165, 2001.

R Yuan, M Kang, S Park, J Hong, D Lee, and J Kim. The effect of coordinate rotation on the eddy covariance flux estimation in a hilly KoFlux forest catchment. *Korean J Agr Forest Meteorol*, 9(2):100–108, 2007.

R Yuan, M Kang, S-B Park, J Hong, D Lee, and J Kim. Expansion of the planar-fit method to estimate flux over complex terrain. *Meteorol Atmos Phys*, 110(3-4):123–133, 2011.

3 Momentum balance of katabatic flow on steep slopes covered with short vegetation

The previous chapter presented new methodologies and adaptations that are required to obtain accurate flux estimates over steep and fully three-dimensional terrain. Subsequently, this chapter begins the investigations into atmospheric flows in mountainous regions. It presents a study of the prevailing physical mechanisms governing the one-dimensional momentum balance of katabatic flow, and has been published with the following citation:

H J Oldroyd, G Katul, E R Pardyjak and M B Parlange. Momentum balance of katabatic flow on steep slopes covered with short vegetation. *Geophysical Research Letters*, 41(13):4761–4768, 2014.

Note that the corresponding supporting materials that were published in the online version of this publication can be found in Appendix A.1.

Abstract: *Katabatic flows over alpine mountainous terrain differ from their forested or bare slope counterparts due to the presence of well-ventilated, short vegetation. The impact of a grass canopy and larger scale pressure perturbations on the one-dimensional mean momentum balance is explored via theory and field measurements. The model presented here reproduces the measured velocity jet shape and turbulent flux gradients. These two features imply that even when Monin-Obukhov similarity theory breaks down, its use for a stability adjusted mixing length remains effective to first order. Results reveal that outer-layer pressure effects can be significant under low speed wind conditions at the top of the thin katabatic layer when larger variations in the wind direction are observed. An analytical expression to estimate the jet height, which can be utilized in large-scale weather prediction models, shows the importance of including canopy effects for the thin katabatic flow region above the vegetation.*

3.1 Introduction

Katabatic winds in mountainous terrain are drawing increased attention given their role in transporting heat [Monti et al., 2002], water vapor, pollutants [Pardyjak et al., 2009], and CO_2 (especially, if vegetated or near urban environments) [Sun et al., 2007], and in the formation of frost [Laughlin and Kalma, 1987], fog [Duynkerke, 1999] and cold pools [Whiteman et al., 2001] within basins and valleys. Typically, katabatic winds form over sloping terrain during nights characterized by clear sky conditions and weak synoptic forcing. Radiative cooling at the surface generates stable stratification and negative buoyancy thereby causing cooler air to sink down the inclined surface [Whiteman, 2000]. Nocturnal drainage flow within and above tall (forest) canopies on slopes has received significant attention (e.g. Chen and Yi [2012], Luo et al. [2009], Luo and Li [2009]), especially in the context of ecosystem carbon balance closure (e.g. Burns et al. [2011], Turnipseed et al. [2003]). Additionally, slopes with forested canopies have been shown to produce complicated mean flow structures, having jet peaks above or below the canopy top [Burns et al., 2011, Yi et al., 2005, Froelich et al., 2005, Froelich and Schmid, 2006]). However, the effects of short vegetation over steep slopes have been largely ignored or lumped into a roughness length that is typically an order of magnitude smaller than the canopy height itself. It has been known for some time that katabaic flows over steep slopes pose unique challenges to their inclusion within large-scale numerical models. First, models of the stable atmospheric boundary layer often 'break down' due to a range physical phenomena that are not commonly included in turbulence modeling, from the formation of a low-level jet to larger scale motions that propagate to the surface [Mahrt et al., 2001, Mahrt, 1998]. In addition, numerical models of the stable boundary layer are prone to producing non-physical phenomena such as 'run-away' surface cooling and spurious laminarization [Jiménez and Cuxart, 2005, Mahrt, 1998]. Second, numerical models generally implement similarity-based scaling parameterizations, usually adopting Monin-Obukhov similarity theory to link the surface to the flow. These parameterizations, developed for flat terrain (e.g. Pahlow et al. [2001] and Brustaert [1982]) with a constant-flux surface layer, are known to break-down in the presence of katabatic flows [Nadeau et al., 2012]. Third, steep, alpine mountainous slope flows typically result in near-surface jets with a peak jet velocity close to the ground surface, thereby compounding the common problems of vertical grid resolution and the explicit coupling between the land surface and the flow aloft in a coarse grid [Renfrew, 2004].

Existing layer models of katabatic wind vary in complexity and structural description, from bulk parameterizations (e.g. Mahrt [1982], Manins and Sawford [1979]) to those that describe mean (velocity and temperature) (e.g. Garrett [1983], Yamada [1983]) and turbulent flux (momentum and heat) profiles (e.g. Rao and Snodgrass [1981], Yi et al. [2005]). However, only a handful of models have been compared with measurements over steep slopes (> 15°). Furthermore, since few measurements have been made of the detailed turbulent structure within the katabatic layer, especially over steep terrain [Nadeau et al., 2013], models are rarely compared with turbulent flux measurements [Yi et al., 2005]. These comparisons are necessary because even if the katabatic layer is shallow (as over steep slopes), mass, momentum, and

heat exchanges between the atmosphere and canopy-ground system occur within this layer [Mahrt et al., 2001].

Here, a one-dimensional mean momentum balance formulation is developed that is forced with measured air temperature profiles. This model is used in conjunction with multi-level measurements over a steep, grassy, alpine slope to interpret the mean momentum balance and characterize the katabatic jet. A key feature of this model is that it explicitly includes the role of short vegetation (as previously considered by Garrett [1983], Luo et al. [2009] and Luo and Li [2009] for a forested canopy), and it is shown that even for short canopies, the role of canopy height remains significant. In addition, the model includes a simplified pressure parameterization that accounts for weak larger scale (synoptic, meso and/or valley scales) pressure perturbations originating from the outer layer and penetrating to the surface. This type of pressure penetration has been studied in flows over hills [Belcher and Wood, 1996, Raupach and Finnigan, 1997], and can also account for some of the variation of topographic curvature over extensive slopes [Haiden and Whiteman, 2005]. Using measurements from nine different intensive observation nights, the significance of including such outer pressure parameterization on the form and structure of the katabatic flow is explored.

3.2 Field Experiment

During the summer of 2011 in Val Ferret [Simoni et al., 2011], a narrow alpine valley in Switzerland, instruments were deployed to investigate thermally driven steep slope flows as a follow-up experiment (see Nadeau et al. [2013]). The local downslope angle, determined from a 10 m^2 area of a 1 m resolution digital elevation map, is 35.5°. Vegetation along the slope was ~30 cm tall alpine flowers and grasses. Measurements were sampled at 20 Hz from five triaxial sonic anemometers (CSAT3, Campbell Scientific) that were mounted with a slope-normal tilt from vertical (to reduce tilt correction angles, and verified with an inclinometer) on a 10 m tower at slope-normal heights of 0.45, 1.27, 2.15, 3.79, and 6.32 m (see Figure 3.1(a)). Velocity tilt corrections were made with the planar fit method applied to each of six 40° wind sectors [Wilczak et al., 2001, Foken, 2008] (see supporting information [herein Appendix A.1] for details regarding the sensor tilt corrections). Additionally, a thermocouple array measuring 1-minute mean air temperatures, was mounted at the tower site. These measurements were converted to virtual potential temperatures, θ, and used to drive the thermal forcing in the model described herein (see supporting information [herein Appendix A.1] for more details about the temperature measurements). Figure 3.1(b) introduces the slope-aligned coordinate system and provides a schematic for the shallow katabatic jet and the near-surface temperature profile that drives the flow. The schematic includes characteristic heights such as the canopy height, h_c, the jet layer height, h_j, and the jet peak height, z_p, and the virtual temperature deficit, $\Delta\theta$. Measurements from nine clear-sky nights in September of 2011 when downslope flow was observed, were used in conjunction with the model. Note that the flow exhibits no consistent jet shape in the $U(z)$ profile during the nights of Sept. 24, 29 and 30, indicating a significant larger scale disturbance preventing a katabatic jet formation. Table A.4

in supporting information [herein Appendix A.1] summarizes characteristic quantities for the experiments. A co-spectral analysis (not included herein) shows that due to sensor path length and sampling frequency limitations, the measured turbulent fluxes at the lowest measurement location are attenuated and their magnitudes are underestimated. This underestimation should not be overlooked in data-model comparisons.

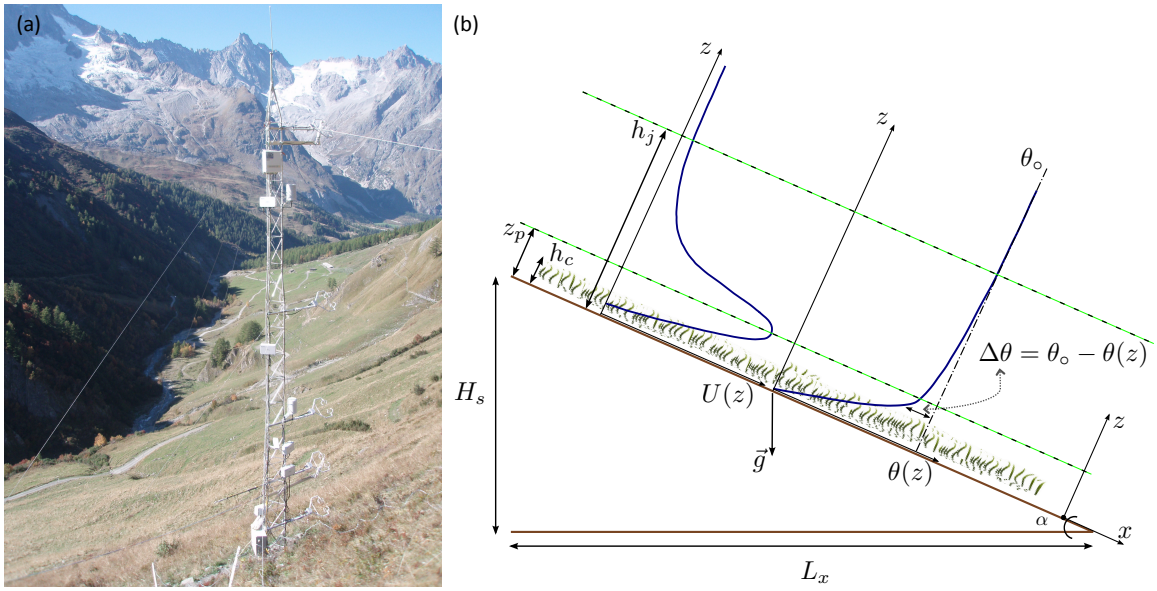

Figure 3.1 – (a) Alpine slope experiment site showing the flux tower. (b) Schematic of slope-aligned coordinate system including sketches of a theoretical katabatic jet and virtual temperature profile (see text for label descriptions).

3.3 Theory

3.3.1 Definitions and Governing Equations

For a constant slope with no curvature and ignoring Coriolis effects near the ground surface, the mean longitudinal and surface-normal momentum balance equations for a katabatic flow on a slope uniformly covered with vegetation (adapted from Haiden and Whiteman [2005] to include the canopy drag) are

$$\frac{\partial U}{\partial t} + U\frac{\partial U}{\partial x} + V\frac{\partial U}{\partial y} + W\frac{\partial U}{\partial z} = -\frac{1}{\rho_o}\frac{\partial P}{\partial x} + g\frac{\Delta\theta}{\theta_o}\sin(\alpha) - \frac{\partial \overline{u'w'}}{\partial z} - C_d a(z)|U|U \tag{3.1}$$

and

$$\frac{\partial W}{\partial t} + U\frac{\partial W}{\partial x} + V\frac{\partial W}{\partial y} + W\frac{\partial W}{\partial z} = -\frac{1}{\rho_o}\frac{\partial P}{\partial z} - g\frac{\Delta\theta}{\theta_o}\cos(\alpha) - C_d a(z)|U|W \tag{3.2}$$

where t is time, x, y and z are aligned directions so that x is the streamwise direction, y is the spanwise direction, and z is orthogonal to the ground, U, V, and W are the mean velocity components along x, y and z, respectively, α is the slope angle, H_s and L_x are characteristic height and length of the slope, respectively ($\tan(\alpha) = H_s/L_x$), P is the turbulent pressure, g is the gravitational acceleration, ρ_o and θ_o are the background density and air temperature above the katabatic flow region (hereafter, quantities subscripted with o indicate averaged variables outside the katabatic jet), $\Delta\theta$ is the virtual temperature deficit (difference from the background state) within the katabatic flow region, and u' and w' are turbulent excursions from the mean state, and an overbar represents time averaging, C_d is the drag coefficient of the foliage defining the canopy, and $a(z)$ is the leaf area density of the vegetation assumed to be uniformly covering the slope and is represented here as LAI/h_c, where LAI is the leaf area index and h_c is the mean vegetation height. The terms $\partial\overline{u'u'}/\partial x$, $\partial\overline{u'v'}/\partial y$, and $\partial\overline{w'w'}/\partial z$ are ignored relative to other terms in the respective mean momentum balance equations given that the turbulence is generally weak under such conditions. Note however, that the $\partial\overline{w'w'}/\partial z$ term may play a role not considered here. The model coordinate system is aligned so that $V = 0$ and $W = 0$ (for consistency with the field experiment, see supporting information [herein Appendix A.1] for further justification), lateral homogeneity is also assumed locally along with stationarity so that

$$0 = -\frac{1}{\rho_o}\frac{\partial P}{\partial x} + g\frac{\Delta\theta}{\theta_o}\sin(\alpha) - \frac{\partial\overline{u'w'}}{\partial z} - C_d a(z)|U|U, \tag{3.3}$$

and

$$0 = -\frac{1}{\rho_o}\frac{\partial P}{\partial z} - g\frac{\Delta\theta}{\theta_o}\cos(\alpha). \tag{3.4}$$

Upon integrating the momentum balance for W along the z direction from the ground, $z = 0$, up to the layer encompassing the katabatic flow region, $z = h_J$,

$$\frac{P(h_J, x)}{\rho_o} = -\frac{g}{\theta_o}\cos(\alpha)\int_0^{h_J}\Delta\theta(z)dz + \frac{P(0,x)}{\rho_o}. \tag{3.5}$$

Here, the term $P(0,x)$ is an integration constant that reflects possible surface pressure variations along the x direction originating from a number of factors such as larger scale disturbances. The h_J is commonly delineated by the height at which $\Delta\theta(z) = 0$, and this delineation is employed here. Substituting this estimate of $P(x)$ into equation (3.3) yields:

$$0 = \frac{g}{\theta_o}\left(\sin(\alpha)\Delta\theta(z) + \cos(\alpha)\frac{\partial\int_0^{h_J}\Delta\theta(z)dz}{\partial x}\right) - \frac{\partial\overline{u'w'}}{\partial z} - C_d a(z)|U|U - \frac{1}{\rho_o}\frac{\partial P(0,x)}{\partial x}. \tag{3.6}$$

The interpretation of the terms are as follows: the first is the hydrostatic pressure driving the katabatic flow downslope, the second is known as the thermal wind arising from the W mean momentum balance, the third is the Reynolds stress gradient, the fourth is the canopy drag force, finite only for $z < h_c$, and the last term reflects pressure undulations originating from

larger scale disturbances in the outer layer (i.e. $z/h_J >> 1$) impacting the katabatic flow regime locally.

3.3.2 Closure Models

Even when $\Delta\theta(z)$ is known, equation 3.6 remains unclosed necessitating another relation between U and $\overline{u'w'}$. Here, a first-order closure is adopted and is given as $\overline{u'w'} = -K_t \partial U/\partial z$, where $K_t = l_m^2 |\partial U/\partial z|$ and l_m is an effective mixing length specified as $\kappa(z-d)/\phi_m(\xi)$ for $z/h_c > 1$ and $\kappa(h_c - d)/\phi_m(\xi_c)$ for $z/h_c < 1$, where $\phi_m(\xi) = 1 + 5\xi$, $\xi = (z-d)/L_{mo}$, and $\xi_c = (h_c - d)/L_{mo}$, L_{mo} is the measured Obukhov length defined above the jet region, $\kappa = 0.4$ is the von Kármán constant, and d is the zero-plane displacement height of the vegetation determined from the centroid of the drag force acting on the flow and is given as

$$d = \frac{\int_0^{h_c} z C_d a U(z)^2 dz}{\int_0^{h_c} C_d a U(z)^2 dz}. \tag{3.7}$$

With these closure assumptions, and upon specifying $\Delta\theta(z)$ (from measurements), the mean longitudinal momentum balance can be solved for $\overline{u'w'}$ and U provided $\partial P(0,x)/\partial x$ is known (or ignored) and boundary conditions are specified. The boundary conditions imposed are $U(0) = 0$ (no-slip at the ground), and $U(z_{max}) = U_o = U_5$, where $z_5 > h_J$ is a reference height, and U_o is taken as a reference velocity (specified from measurements, U_5) above the jet reflecting outer-layer conditions. Additionally, the canopy is assumed to be characterized by a dimensionless foliage drag, $C_d = 0.2$, and typical $LAI = 1.5$ m^2/m^2 [Katul et al., 2004].

3.3.3 Scaling analysis

Even for the idealized setup considered here, difficulties in analyzing drainage flows on steep slopes covered with vegetation remain. These difficulties originate from a multiplicity of length scales impacting the mean momentum balance. The pertinent length scales include $L_x = H_s(\tan(\alpha))^{-1}$ that typically governs horizontal gradients, the thickness of the katabatic flow region, h_J, that impacts vertical gradients above the canopy but within the jet, the adjustment length scale, $L_c = h_c(C_d LAI)^{-1}$, the canopy height, h_c, affecting the flow within the canopy, and the Obukhov length, L_{mo}, dictating the eddy sizes responsible for vertical mixing of momentum. The relative importance of the thermal wind to the hydrostatic pressure term is given as

$$\frac{\cos(\alpha)}{\sin(\alpha)} \frac{\frac{\partial \int_0^{h_J} \Delta\theta(z) dz}{\partial x}}{\Delta\theta(z)} \sim \frac{\cos(\alpha)}{\sin(\alpha)} \frac{h_J}{L_x}. \tag{3.8}$$

For the steep slopes here, h_J is of order of 10 m (as shown later), while L_x is of order 1000 m. Hence, the thermal wind term may be ignored relative to the hydrostatic term. Moreover, the local distortion time scale of the mean flow by advective terms are on the order of L_x/U while

vertical gradients of the mean flow within the katabatic region equilibrate with the stresses on time scales of h_J/u_*, where u_* is the friction velocity above the canopy but within the katabatic flow region. Hence, provided $(h_J/L_x)(U/u_*) << 1$, the advective terms impact the mean velocity profile at time scales much longer than the shear gradients, and the two terms are prohibited from interacting locally. In general, U/u_* can be of order 10, but h_J/L_x is of order 1×10^{-3}. In the event that $(h_J/L_x)(U/u_*)$ is of order unity, advective terms cannot be ignored and the problem can no longer be treated as one-dimensional. It has been known for sometime that a drainage flow immediately above the surface is influenced by the local slope on the smallest scales, while the flow at the higher levels in the atmosphere may be influenced by terrain slopes on a larger scale. Larger scale disturbances may originate from variations in outer layer mean wind direction, thereby sensing slope angles different from α during the course of an averaging period. These large scale variations in slope angles are occurring over distances much larger than h_J and impact the outer layer flow field far above the katabatic flow region. Under those conditions, and as is common in studies of flow over hills, a scaling analysis for the outer layer well above the katabatic flow region suggests that

$$-\frac{1}{\rho_o}\frac{\partial P(0,x)}{\partial x} = U_o\frac{\partial U_o}{\partial x} + \frac{\partial U_o}{\partial t} \sim C_p\frac{U_o^2}{R}, \tag{3.9}$$

where C_p is a pressure coefficient, U_o is, as before, the typical outer-layer velocity [Belcher and Wood, 1996], and R is an effective curvature (positive or negative) reflecting slope changes along L_x sensed by the larger scale wind [Haiden and Whiteman, 2005]. For a uniform slope, $R \to \infty$, and the usual assumptions invoked in earlier studies are recovered. With these simplifications,

$$0 = \frac{g}{\theta_o}\sin(\alpha)\Delta\theta(z) \mp C_p\frac{U_o^2}{R} + \frac{\partial}{\partial z}\left(l_m^2\left|\frac{\partial U}{\partial z}\right|\frac{\partial U}{\partial z}\right) - C_d a(z)|U|U. \tag{3.10}$$

Hence, larger scale variations in wind direction lead to different slope angles being sensed in the outer layer well above h_J, that then produces a $\partial P(x)/\partial x$ that integrates these variations at a point. To first order it may be assumed that $R \sim L_x$. In the data analysis here, conditions where the stability regime near the top of h_J is strong (and hence susceptible to such larger scale disturbances) or weak (and bulk flow is near neutral above the jet with a preset direction) are both explored. It is common practice to replace the canopy vertical structure with a momentum roughness height (z_o) while ensuring that $\overline{u'w'}(z_o) = \overline{u'w'}(h_c)$. Here, h_c was retained (via the drag force) thereby allowing the role of h_c in modifying aspects of the jet shape such as the location of the maximum mean velocity ($z = z_p$) to be assessed. To illustrate, consider a linear temperature profile given as $\Delta\theta(z) = \Delta\theta_{max}(1 - z/h_J)$ when $h_c/h_J < 1$ and $\Delta\theta(z) = 0$ when $z > h_J$. For $h_c < z < h_J$, where the location of the maximum jet velocity is anticipated, equation 3.10 can be integrated to yield

$$\overline{u'w'}(z) = \overline{u'w'}(h_c) + (A_D \mp B_P)(z - h_c) + A_D\frac{h_c^2 - z^2}{2h_J}, \tag{3.11}$$

where $A_D = (g/\theta_o)\sin(\alpha)\Delta\theta_{max}$ and $B_P = C_p U_o^2/R$ are constants independent of z. The maximum jet velocity U_{max} occurs at a $z = z_p$ where $\partial U/\partial z = 0$. From the closure equation ($\overline{u'w'} = -K_t \partial U/\partial z$), it follows that z_p is co-located with the height at which $\overline{u'w'}(z) = 0$. Using this condition and solving for z_p from equation 3.11 results in

$$\frac{z_p}{h_J} = \left[1 \mp \frac{B_p}{A_D} - \sqrt{\left(-\frac{h_c}{h_J} + 1 \mp \frac{B_p}{A_D}\right)^2 + 2\frac{\overline{u'w'}(h_c)}{A_D h_J}}\right], \tag{3.12}$$

which now makes explicit the role of h_c/h_J. A finite h_c displaces the vertical location of the jet peak velocity downwards compared to the case when $h_c = 0$. Likewise, when B_p is negative and increasing in magnitude, z_p decreases. Also, for negligible B_p and small A_D associated with a small $\Delta\theta_{max}$, z_p increases with declining $\Delta\theta_{max}$. For illustration, consider the case with $B_p = 0$, $h_J = 6$m, $h_c = 0.3$m, $\Delta\theta_{max}/\theta_o = 0.01$, $\alpha = 35.5°$, and $\overline{u'w'}(h_c) = -0.05$ m^2 s^{-2}. Using equation 3.12, $z_p/h_J \approx 0.2$ resulting in $z_p/h_c \approx 4$ (i.e. of order unity). It is for this reason that the vertical structure of the canopy cannot be entirely ignored for katabatic flows on steep slopes covered even by short vegetation.

3.4 Results and Discussion

Figure 3.2 shows the comparison between modeled and measured mean velocity and vertical momentum flux profiles for varying pressure coefficient (C_p = 0, 5, 10), along with the measured mean air temperature profile used to force the buoyancy term for the night of 15 September. The model with optimal C_p captures the shape of the katabatic jet and its peak velocity near the vegetation top. In addition, it reproduces the large gradients observed in the vertical momentum flux and the sign change that occurs in the vicinity of the jet peak. The largest disagreement between the model and measurements for $\overline{u'w'}$ occurs at the lowest measurement location, where measured flux attenuation determined from co-spectral analysis was also observed. This underestimation in the measured flux magnitudes explains some of the difference, but bias in the modeled results could also exist due to uncertainties in the canopy height or temperature measurements. However, the general agreement infers that even in the absence of a constant flux surface layer, the use of Monin-Obukhov similarity theory to set the stability adjusted mixing length in a K-theory closure model can produce reasonable (first order) estimations for $\overline{u'w'}$. Assuming sufficient vertical grid resolution to resolve the extremely thin jet layer, the use of K-theory may be valid for vertical momentum transport if the advection time scale is *much* longer than the equilibration time scale of turbulence. From a scaling analysis perspective, the advection time $\sim L_x/U_o$ and the equilibration time with the mean velocity gradient is on the order of the turbulent kinetic energy normalized by its dissipation rate ($\sim l_m/\sigma_w$). Hence, when $L_x/l_m >> U_o/\sigma_w$, K-theory closure may be used. For the setup here, $L_x/l_m \sim 100$, while $U_o/\sigma_w \sim 10$ perhaps suggesting the use of K-theory to close one of the terms in the mean momentum balance is justifiable. The momentum flux profile within the canopy region differs from the expected monotonic profile for near-neutral conditions over flat terrain (e.g. Yi [2008], Finnigan [2000]). Near the ground, $U \approx 0$ so the

drag force (scales as U^2) is small and $\partial/\partial z(\overline{u'w'})$ must balance $(g/\theta_o)sin(\alpha)\Delta\theta$ resulting in a negative deviation in $\overline{u'w'}$ from zero. Additionally, a nonzero $\partial P/\partial x$ amplifies this effect. The derivation here also makes clear that C_p is only significant when larger scale variations introduce large variability in wind direction. Figure 3.3 suggests that the optimal C_p derived by minimizing the root-mean squared error between measured and modeled $U(z)$ is largest for small U_o, and that small U_o are, in fact (observed also by Davies and Thomson [1999] and Turnipseed et al. [2003]), associated with the largest variance in wind direction (thereby sampling multiple slope angles). This trend is observed at all measurement heights (see Figure A.1 in supporting information [herein Appendix A.1]), which implies that larger scale pressure perturbations can penetrate down to the surface and that flow decoupling through the katabatic layer does not occur (unlike the case of a dense and tall forested canopy). For large U_o or small variations in wind direction at h_j, the optimal $C_p \approx 0$ and this term can be ignored for a conventional katabatic jet along a homogeneous slope. However, if the wind direction fluctuations are large, presumably due to larger disturbances originating from the outer layer, then $C_p \approx 20$. Note that following the optimization of the C_p value, the root-mean squared error between measured and modeled $U(z)$ becomes independent of U_o (i.e. the flow conditions above the katabatic jet). Even in the cases when $C_p \approx 20$, this term contributes to no more than 20% of the mean momentum balance. Therefore, the outer pressure term can be significant, but as expected, the momentum budget is mainly a balance between buoyancy and frictional mechanisms. Naturally, C_p may also encode other processes such as local advection and subsidence that need not be independent of z. However, lower values of C_p are associated with low root-mean squared error and higher values of U_o, when advective effects are more likely to have importance. Hence, advection likely plays a small role in the momentum budget here and its omission is a reasonable assumption (see also supporting information [herein Appendix A.1]). In contrast, Horst and Doran [1986] show results for a site where vegetation and topography are highly variable in space, and advection cannot be neglected *a priori*, likely because of these non-uniformities along the slope. Figure 3.3 makes clear that deviations between modeled and measured $U(z)$ can be partially corrected via a C_p that is significantly linked to variability in wind direction. This link is further established by Figure A.2 in the supporting information [herein Appendix A.1] that shows the correlations between U and mean wind direction, which is characterized by a Gaussian distribution (Figure A.3).

3.5 Conclusions

A one-dimensional mean momentum balance formulation is developed for describing the katabatic jet on steep slopes covered with vegetation. The main novelty is inclusion of the effects of the short vegetation and the weak larger scale pressure perturbations that cause large fluctuations in wind direction. The model explicitly reveals how these two additions impact the location of the peak velocity within the katabatic jet. Because of its simplified structure, the approach proposed here can be used to complement classical wall-functions

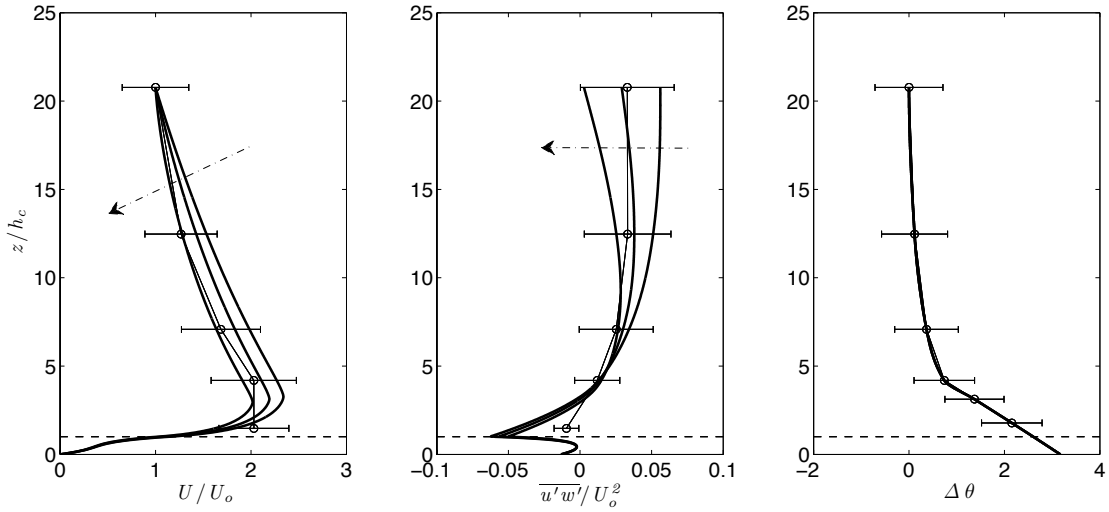

Figure 3.2 – Comparison between measured (symbols with error bars) and modeled (lines) $U(z)$ and $\overline{u'w'}(z)$ averaged over 1 hour for the night of 15 September. Horizontal error bars indicate one standard deviation derived from 5 minute averages around the hourly mean. Dashed horizontal lines at $z/h_c = 1$ show the canopy height. Arrows indicate direction of increasing C_p (=0, 5,10). For reference the measured $\Delta\theta(z)$ used to drive the model is shown.

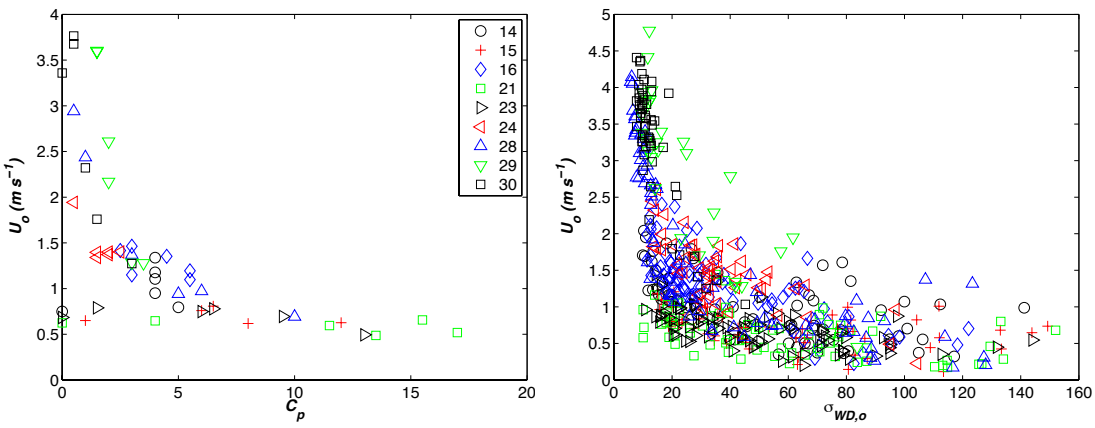

Figure 3.3 – The variation of computed optimal C_p as inferred by minimizing the root-mean-squared error (RMSE) between measured and modeled $U(z)$ for each 1-hour run across nine nighttime runs in September (differentiated by symbols) for measured U_o. Note the increasing C_p with decreasing U_o. Finally, the relation between the measured U_o and $\sigma_{WD,o}$ is shown for all five minute segments.

used to bridge the land-surface with atmospheric flows in large-scale numerical models of mountainous terrain. It can also aid in field experimental designs aimed at resolving the structure of turbulence within the katabatic jet. This latter topic is now receiving broad experimental attention as approaches to quantifying CO_2 drainage at night are becoming a central research focus to correcting eddy-covariance based flux measurements aimed at estimating carbon balances over complex topography.

Acknowledgments

The data for this work can be obtained via email from the corresponding author. This research was primarily funded by the Swiss National Science Foundation (SNSF-200021-134892) and the Competence Center for Environmental Sustainability (CCES-SwissEx) of the ETH domain. Katul acknowledges the National Science Foundation (NSF-EAR-1013339, NSF-AGS-1102227, and NSF-CBET-103347), the United States Department of Agriculture (2011-67003-30222), the U.S. Department of Energy (DOE) through the office of Biological and Environmental Research (BER)Terrestrial Ecosystem Science (TES) Program (DE-SC0006967), and the Binational Agricultural Research and Development (BARD) Fund (IS-4374-11C). Pardyjak acknowledges the Office of Naval Research Award # N00014-11-1-0709.

Bibliography

SE Belcher and N Wood. Form and wave drag due to stably stratified turbulent flow over low ridges. *Q. J. Roy. Meteor. Soc.*, 122(532):863–902, 1996.

W Brustaert. *Evaporation into the atmosphere, theory, history and application.* Kluwer Academic Publishers, The Netherlands, 1982.

Sean P Burns, J Sun, DH Lenschow, SP Oncley, BB Stephens, C Yi, DE Anderson, J Hu, and RK Monson. Atmospheric stability effects on wind fields and scalar mixing within and just above a subalpine forest in sloping terrain. *Boundary-Layer Meteorol.*, 138(2):231–262, 2011.

H Chen and C Yi. Optimal control of katabatic flows within canopies. *Q. J. Roy. Meteor. Soc.*, 138(667):1676–1680, 2012.

BM Davies and DJ Thomson. Comparisons of some parametrizations of wind direction variability with observations. *Atmos. Environ.*, 33(29):4909–4917, 1999.

PG Duynkerke. Turbulence, radiation and fog in dutch stable boundary layers. *Boundary-Layer Meteorol.*, 90(3):447–477, 1999.

J Finnigan. Turbulence in plant canopies. *Annu. Rev. Fluid Mech.*, 32(1):519–571, 2000.

T Foken. *Micrometeorology.* Springer, Berlin, Germany, 2008.

NJ Froelich and HP Schmid. Flow divergence and density flows above and below a deciduous forest: Part II. Below-canopy thermotopographic flows. *Agr. Forest Meteorol.*, 138(1):29–43, 2006.

NJ Froelich, HP Schmid, CSB Grimmond, H-B Su, and AJ Oliphant. Flow divergence and density flows above and below a deciduous forest: Part I. Non-zero mean vertical wind above canopy. *Agr. Forest Meteorol.*, 133(1):140–152, 2005.

AJ Garrett. Drainage flow prediction with a one-dimensional model including canopy, soil and radiation parameterizations. *J. Clim. Appl. Meteorol.*, 22(1):79–91, 1983.

T Haiden and CD Whiteman. Katabatic flow mechanisms on a low-angle slope. *J. Appl. Meteorol.*, 44(1):113–126, 2005.

TW Horst and JC Doran. Nocturnal drainage flow on simple slopes. *Boundary-Layer Meteorol.*, 34(3):263–286, 1986.

MA Jiménez and J Cuxart. Large-eddy simulations of the stable boundary layer using the standard Kolmogorov theory: range of applicability. *Boundary-Layer Meteorol.*, 115(2): 241–261, 2005.

G Katul, L Mahrt, D Poggi, and C Sanz. One-and two-equation models for canopy turbulence. *Boundary-Layer Meteorology*, 113(1):81–109, 2004.

GP Laughlin and JD Kalma. Frost hazard assessment from local weather and terrain data. *Agr. Forest Meteorol.*, 40(1):1–16, 1987.

Z Luo and Y Li. Influence of plant canopy on the katabatic winds. Yokohama, Japan, 29 June - 3 July 2009. The seventh International Conference on Urban Climate.

Z Luo, Y Li, and C Yi. Analytical solution of cold-air-drainage flow within and above forest canopy. Berkeley, CA, September 2009. Second International Conference on Countermeasures to Urban Heat Islands.

L Mahrt. Momentum balance of gravity flows. *J. Atmos. Sci.*, 39:2701–2711, 1982.

L Mahrt. Stratified atmospheric boundary layers and breakdown of models. *Theor. Comp. Fluid Dyn.*, 11(3):263–279, 1998.

L Mahrt, D Vickers, R Nakamura, MR Soler, J Sun, S Burns, and DH Lenschow. Shallow drainage flows. *Boundary-Layer Meteorol.*, 101(2):243–260, 2001.

PC Manins and BL Sawford. A model of katabatic winds. *J. Atmos. Sci.*, 36:619–630, 1979.

P Monti, HJS Fernando, M Princevac, WC Chan, TA Kowalewski, and ER Pardyjak. Observations of flow and turbulence in the nocturnal boundary layer over a slope. *J. Atmos. Sci.*, 59(17): 2513–2534, September 2002.

DF Nadeau, ER Pardyjak, CW Higgins, and MB Parlange. Similarity scaling over a steep alpine slope. *Boundary-Layer Meteorol.*, 147(3):401–419, 2012.

DF Nadeau, ER Pardyjak, CW Higgins, H Huwald, and MB Parlange. Flow during the evening transition over steep alpine slopes. *Q. J. Roy. Meteor. Soc.*, 139(672):607–624, 2013. ISSN 1477-870X. URL http://dx.doi.org/10.1002/qj.1985.

M Pahlow, MB Parlange, and F Porté-Agel. On Monin–Obukhov similarity in the stable atmospheric boundary layer. *Boundary-Layer Meteorol.*, 99(2):225–248, 2001.

ER Pardyjak, HJS Fernando, JCR. Hunt, AA Grachev, and J Anderson. A case study of the development of nocturnal slope flows in a wide open valley and associated air quality implications. *Meteorol. Z.*, 18(1):85–100, 2009.

KS Rao and HF Snodgrass. A nonstationary nocturnal drainage flow model. *Boundary-Layer Meteorol.*, 20(3):309–320, 1981.

MR Raupach and JJ Finnigan. The influence of topography on meteorlogical variables and surface-atmosphere interactions. *J. Hydrol.*, 190(3):182–213, 1997.

IA Renfrew. The dynamics of idealized katabatic flow over a moderate slope and ice shelf. *Q. J. Roy. Meteor. Soc.*, 130(598):1023–1045, 2004.

S Simoni, S Padoan, DF Nadeau, M Diebold, A Porporato, G Barrenetxea, F Ingelrest, M Vetterli, and MB Parlange. Hydrologic response of an alpine watershed: Application of a meteorological wireless sensor network to understand streamflow generation. *Water Resour. Res.*, 47 (10):W10524, 2011.

J Sun, SP Burns, AC Delany, SP Oncley, AA Turnipseed, BB Stephens, DH Lenschow, MA LeMone, RK Monson, and DE Anderson. CO2 transport over complex terrain. *Agr. Forest Meteorol.*, 145(1-2):1–21, 2007.

AA Turnipseed, DE Anderson, PD Blanken, WM Baugh, and RK Monson. Airflows and turbulent flux measurements in mountainous terrain: Part 1. Canopy and local effects. *Agr. Forest Meteorol.*, 119(1):1–21, 2003.

CD Whiteman. *Mountain Meteorology: Fundamentals and Applications.* Oxford University Press, USA, 2000.

CD Whiteman, S Zhong, WJ Shaw, JM Hubbe, X Bian, and J Mittelstadt. Cold pools in the columbia basin. *Weather Forecast.*, 16(4):432–447, 2001.

JM Wilczak, SP Oncley, and SA Stage. Sonic anemometer tilt correction algorithms. *Boundary-Layer Meteorol.*, 99(1):127–150, 2001.

T Yamada. Simulations of nocturnal drainage flows by a $q^2 l$ turbulence closure model. *J. Atmos. Sci.*, 40(1):91–106, 1983.

C Yi, RK Monson, Z Zhai, DE Anderson, B Lamb, G Allwine, AA Turnipseed, and SP Burns. Modeling and measuring the nocturnal drainage flow in a high-elevation, subalpine forest with complex terrain. *J. Geophys. Res.*, 110:D22303, 2005.

Chuixiang Yi. Momentum transfer within canopies. *J. Appl. Meteorol. Clim.*, 47(1), 2008.

4 Advancing Similarity Theory for Katabatic Flow

In the previous chapter, a one-dimensional model was used in consert with measurements to investigate the mean momentum balance of katabatic flows. The results from that study implied that the use of Monin-Obukhov similarity theory to set the mixing length in the turbulence closure model is valid for katabatic flow, despite the steep vertical gradients observed in the momentum fluxes. To examine this implication more thoroughly, this chapter directly investigates Monin-Obukhov similarity theory, and local similarity scaling more generally, for katabatic flows. In addition, the vertical structure of turbulent fluxes in katabatic flow and their transport capabilities are also closely examined in this chapter.

4.1 Introduction

Katabatic, or thermally-driven drainage flows in mountainous regions are notoriously problematic for numerical weather prediction models. This can be attributed to a variety of factors like difficulties in representing the underlying terrain (especially for very steep slopes), and typical complications associated with simulating a stable boundary layer (see Mahrt [1998] and Mahrt [2014] for a comprehensive compilation). However, one characteristic of katabatic flows that makes them particularly difficult to model is the fact that katabatic jet layers are relatively thin, or extremely thin (< 10 m) in the case of steep slopes (e.g., [Nadeau et al., 2013, Oldroyd et al., 2014]). Subsequently, all of the turbulent exchange between the atmosphere and the underlying surface occurs over this thin layer, leading to steep gradients in the variables of interest [Mahrt et al., 2001]. For numerical models this leads to problems with affording sufficient grid resolution [Renfrew, 2004]. Moreover, since gradients of velocity, temperature, momentum flux and scalar fluxes are very steep within the katabatic jet layer, traditional wall models, which 'transfer' the surface conditions to the lowest grid cells in the simulated atmosphere, are no longer appropriate. Traditional wall models were developed for flat terrain and typically assume a constant flux surface layer; therefore, they cannot reproduce the steep gradients found in katabatic flows [Grisogono and Oerlemans, 2001, Mahrt, 1998, Nadeau et al., 2012].

Wall models are often developed from similarity theory, which states that for certain types of atmospheric boundary layer (ABL) flows a 'universal' functionality exists between properly-scaled (nondimensionalized) flow variables [Stull, 1988]. Hence when appropriate, similarity theory can be a powerful tool in describing and predicting ABL flows for which descriptions or laws based solely on first principles of physics and thermodynamics are often unattainable [Stull, 1988]. Typically in similarity theory, flow variables are grouped via dimensional analysis and the functional relation is determined empirically over a range of stability conditions. Beyond numerical modeling applications, similarity theory can be used to estimate turbulent fluxes from mean measurements [Brustaert, 1982].

The most widely used similarity theory, Monin-Obukhov similarity theory, was initially proposed for ABL flows over flat and statistically homogeneous terrain over which a 'constant-flux' (varying by less than 10%) surface layer exists [Monin and Obukhov, 1959]. The scaling variables in this case are defined within this constant-flux surface layer and so sometimes it is referred to as *surface-layer scaling*. Even though 'flat and statistically homogeneous terrain' implies a very strict classification for *real* terrain to satisfy, Monin-Obukhov similarity theory has been shown to hold for a variety of flow situations outside of the narrow terrain assumptions initially proposed. Brutsaert [1998] attributes the ability to relax some of these strict assumptions in a practical sense to the fact that horizontal scales are much larger than vertical scales in the ABL, and to the homogenizing nature of turbulence.

The notion that Monin-Obukhov similarity theory typically works helps to explain why it is so widely used in meteorological and hydrological models for real terrain, even when theoretically it should break down. Under ideal conditions it can have an accuracy of 10-20% [Foken, 2006]. However, beyond the strict set of assumptions, no clear metric exists for whether or not a similarity theory holds in a practical sense. One reason why a clear metric is difficult to define is that data from observational studies typically show varying degrees of scatter around the similarity relations and the distribution of this scatter also tends to vary with stability (e.g, [Högström, 1996] and [Johansson et al., 2001]). Another reason is that random errors in the measurements can propagate to varying degrees in the measured relations [Salesky and Chamecki, 2012]. Furthermore, the stability parameter itself can be associated with high uncertainties; for example Salesky and Chamecki [2012] show uncertainties as high as 40% or more in the Monin-Obukhov stability parameter for the unstable regime. In addition, the similarity scalings may hold for one variable but break down for another. Hence, it is difficult to attribute the scatter to random error or to incomplete theory. Perhaps another explanation as to why Monin-Obukhov similarity theory is so widely used (potentially when it is inappropriate) is due to a lack of alternative, or more accurate, theories to predict turbulent exchange in the ABL.

The surface layer and local Monin-Obukhov similarity scalings have been shown to break down for katabatic flows [Grisogono and Oerlemans, 2001, Mahrt, 1998, Nadeau et al., 2012]. Yet, thermally driven katabatic flows are largely governed by the surface conditions (roughness and radiative cooling rates) and exhibit a jet-like velocity profile [Whiteman, 2000]. This suggests

potential 'universal-katabatic' relations, which could be revealed with the proper similarity scaling. Some studies have been aimed at using the local Monin-Obukhov similarity scaling to investigate this hypothesis. Modified Mellor-Yamada type models [Mellor and Yamada, 1982] have been used by Denby [1999] and Łobocki [2013] to generate simulated similarity relations specifically for katabatic flow within the Monin-Obukhov scaling framework. Field studies of katabatic flows with shallow slope angles (~ 5°) have evaluated local Monin-Obukhov similarity scaling for flux-gradient relations over glaciers (e.g., Smeets et al. [1988, 2000] and Van Der Avoird and Duynkerke [1999]) with relative success for a very narrow range of stabilities. In addition, Nadeau et al. [2012] have evaluated the validity of local Monin-Obukhov similarity scaling for steep slope flow for a single measurement height. Their study shows that steep slope katabatic flow presents an example for which even local Monin-Obukhov similarity theory completely breaks down in the flux-profile relations [Nadeau et al., 2012]. Hence, it remains unclear if a 'universal functionality' exists for katabatic flows.

This chapter seeks to advance similarity theory for steep slope katabatic flows using field data taken over a steep (35.5°), alpine slope in Val Ferret, Switzerland. Section 4.2 discusses the field data used in the study, some data processing techniques, and the coordinate systems which frame the analyses. Box plots showing the mean vertical structure within the katabatic layer are presented in Section 4.3. Section 4.4 provides a brief overview of Monin-Obukhov similarity theory, and Section 4.5 reevaluates the validity of local Monin-Obukhov similarity theory and the extended stability functions for steep slope katabatic flow within the purview of qualitatively understanding the differences (and similarities) between turbulent mixing that occurs over flat versus steeply sloping terrain. This will be done by expanding the analyses of Nadeau et al. [2012] to five measurement locations within the katabatic jet layer to determine if a clear functionality within this scaling framework exists for the katabatic flow. Model-generated relations and measurements from field studies over glaciers are used in comparison with the observed behaviors. Subsequently, alternative, empirically-derived, similarity relations are proposed and evaluated using the field data. Section 4.6 discusses roles that turbulent kinetic energy plays in relation to turbulent mixing within katabatic jets and in relation to similarity theory. Hypotheses and future work suggested to further advancement of similarity theories for katabatic flow are discussed in Section 4.8. Finally, Section 4.9 summarizes key findings.

4.2 Field Data

The field data set used for the similarity theory analyses presented herein is the same as was used for the 1D momentum balance analyses presented in Chapter 3, and a description of the field experiment is provided in Sections 3.2 and A.1.3. The momentum balance was analyzed for nine clear-sky nights in September 2011 when downslope flow was observed. Table A.4 summarizes key quantities for these nights. It shows that for 5 nights (14, 15, 16, 21 and 23 of September) conditions were such that a clear katabatic jet developed over the slope. Whereas during the other four nights, although downslope flow was observed, the synoptic forcing was sufficiently strong, and no clear jet-shaped velocity profile developed. Hence, for the similarity

analyses herein only the data from the 5 *katabatic nights* were used.

Prior to analyzing the data in the context of similarity theory, optimized sector-wise planar-fit tilt corrections as described in Oldroyd et al. [2015 *in press*] were performed for each sonic anemometer using the full data set from September (see Sections 2.3 through 2.7). As discussed in Oldroyd et al. [2015 *in press*] (Sections 2.8 through 2.9), the coordinate system(s) in which the data are analyzed must be selected carefully for flows over steep terrain. Figure 4.1 shows a 2D schematic of the coordinate systems that are implemented. The horizontal-vertical coordinate system (indicated by the blue vectors in Figure 4.1) is aligned with the gravity vector, and variables in this system are indicated with a 'hat' so that $\hat{w}$ is the vertical velocity in the $\hat{z}$ direction. The slope-define coordinate system (indicated by the red vectors in Figure 4.1) is rotated by α, the terrain slope angle, such that w is the slope-normal velocity in the z direction. In addition to the orientation, the coordinate system can either implemented as fixed or rotating (where u follows the mean wind direction, as is often done for atmospheric flow). In the slope-defined coordinate system both the fixed and the rotated implementation have advantages and disadvantages depending on the variable of interest. For example, quantities associated with momentum are more easily calculated in the rotating system. In contrast, quantities that depend on the acceleration due to gravity are more easily calculated in the fixed system because on a planar slope (see arguments in Section 2.9) variables, such as the heat flux, aligned with the cross-slope direction are at 90° to the gravity vector and the buoyancy effects are zero in that direction ($g\sin(90°) = 0$). To simplify the analyses herein, both implementation schemes are used. Angle brackets around a variable indicate time averaging in the rotating scheme. For example, $< u >$ and $\langle u'w' \rangle$ are the mean streamwise velocity and momentum flux, respectively, and the primed variables indicate turbulent fluctuation from the mean. Additionally, an over-line indicates time averaging, but in the fixed scheme, such that $\bar{u}$ is a positive mean velocity for purely downslope flow, and $\overline{u'\theta'}$ is the mean along-slope heat flux. For brevity, the slope-normal and vertical heat fluxes will be same in a rotating or a fixed coordinate scheme. However the over-line notation will be used, such that $\overline{\hat{w}'\theta'}$ and $\overline{w'\theta'}$ are the mean vertical and slope-normal heat fluxes, respectively. Finally, it is worth noting that this careful distinction between coordinate systems and notation may seem laborious. However, it is important for making accurate flux calculations for the katabatic flow. For example, Equation 4.9 (below) is the buoyant production/destruction term in the turbulence kinetic energy (TKE) budget equation. If $\overline{u'\theta'}$ in Equation 4.9 were to be computed using a streamwise rotating coordinate system it would lead to an over estimation in the magnitude of its contribution to buoyancy because cross-slope components are perpendicular to gravity.

Employing the appropriate averaging time is important for analyzing field data to obtain meaningful turbulent flux calculations [Babić et al., 2012, Foken, 2008, Kaimal and Finnigan, 1994, Vickers and Mahrt, 2003, 2006]. Essentially, if the averaging time is too short, the flux calculations will not be appropriately converged, and if it is too long nonstationarity effects and larger-scale motions can contaminate the flux calculations. Additionally, the most appropriate averaging time can change with stability, wind direction (due to various topographical differences), sensor height and the particular flux being averaged. According

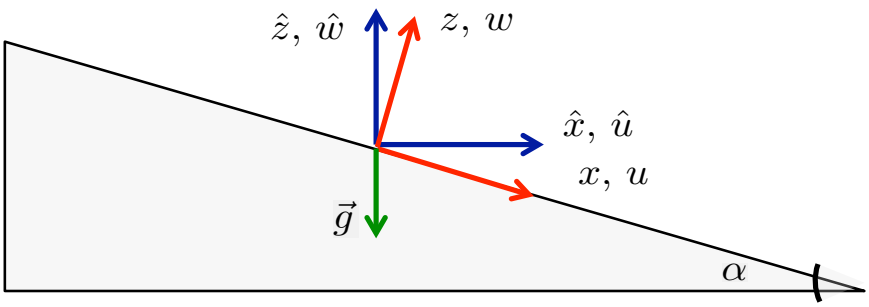

Figure 4.1 – 2D schematic of coordinate systems for sloping terrain. The blue coordinate system is the vertical-horizontal coordinate system where the vertical component is aligned with the acceleration due to gravity. Variables calculated in this system are indicated by a 'hat' (e.g., $\hat{z}$ and $\hat{w}$). The red coordinate system is the slope-defined coordinate system, where $\bar{w}$ is the mean slope-normal velocity in the z direction and $\bar{u}$ is the mean along-slope velocity. See text for more detail regarding fixed versus streamwise-defined coordinate system use.

to Vickers and Mahrt [2006], in similarity theory analyses, the issue of contamination due to larger-scale motions is of high importance not only because these large-scale motions increase random sampling error and scatter, but also because these motions are not well-related local shear or temperature gradients. To aid in selecting an appropriate averaging time, ogive [Babić et al., 2012] and multi resolution (MR) decomposition [Vickers and Mahrt, 2003, 2006] analyses were performed on the katabatic data. The summary of these averaging time analyses suggest that 10-minutes is the most consistently (between sensors, data segments, the various fluxes and the two methods) appropriate averaging time, and it was employed for all mean quantities.

4.3 Measured Mean Profiles

As stated in Section 4.1, a common characteristics of katabatic flows are the steep gradients observed within the thin jet layer. Figure 4.2 shows box plots profiles of the mean streamwise velocity, $< u >$ and virtual temperature, $\bar{\theta}$. The velocity profile (Figure 4.2A) exhibits the expected jet shape with a peak approximately at z =1 m, as indicated by the dotted green line. The virtual temperature profile (Figure 4.2B) shows a strong near-surface thermal stratification that weakens with height above the surface, approaching a zero gradient at the uppermost measurement location. This indicates the measurements nearly cover the entirety of the katabatic jet layer. This measurement setup is noteworthy as few experimental studies have probed the katabatic jet with this density of high-frequency sensors capable of probing the jet's vertical turbulence structure above *and below* the peak of the katabatic jet. One exception is a part of the ongoing Mountain Terrain Atmospheric Modeling and Observations (MATERHORN) program [Fernando and Pardyjak, 2013, Fernando et al., 2015 *in press*]. In contrast, their measurements were made for relatively shallow slope inclination angles (2°-4°) [Grachev et al.,

2015 *in press*, Jensen et al., 2015 *in press*].

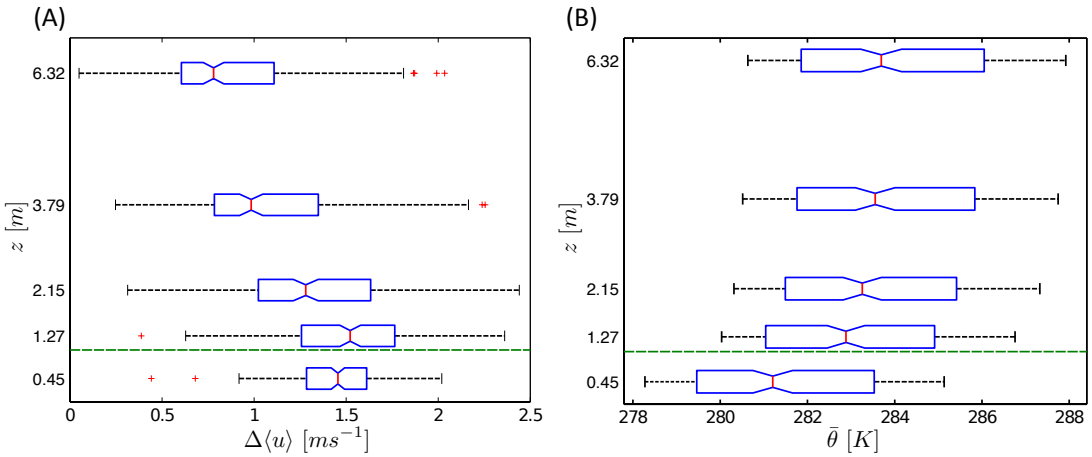

Figure 4.2 – Box plot profiles of (A) streamwise velocity and (B) virtual temperature. The dotted green line is the estimated height of the katabatic jet peak, or velocity maximum.

Figure 4.3 presents the box plot profile of the streamwise momentum flux. Here the estimated height of the jet peak corresponds to the estimated height at which the momentum flux changes sign from negative to positive with the changing sign in the velocity gradient (from positive to negative see Figure 4.2). The slope-normal and along-slope heat fluxes are shown in Figure 4.4(A) and (B), respectively. As expected, the slope-normal component of the heat flux is negative throughout the jet layer. However, an unexpected feature of the slope-normal heat flux profile is the lack of monotonicity considering the $\bar{\theta}$ profile (Figure 4.2B) is monotonic. Data from the lowest measurement location do show evidence of flux attenuation via Fourier cospectal analyses (not shown herein), but this is a relatively small fraction of the total flux and likely does not fully explain the nonmonotonic behavior. The nonmonotonicity and counter-gradient behavior will be discussed in Section 4.7, but is expected to be problematic for flux-profile similarity relations. The along-slope heat flux (4.4(B)) is mostly negative in the bulk of the katabatic jet, which corresponds to an *upslope* heat flux, based on the coordinate system definition (with positive $\bar{u}$ directed downslope). The along-slope heat flux profile is non monotonic and changes sign near the upper part of the katabatic jet layer. This heat flux component will also be discussed in more detail in Section 4.7, but it is worth noting here that the along-slope component is nearly an order of magnitude greater than the slope-normal component.

In combination, the measured flux profiles paint a complicated portrait of the mixing mechanisms occurring in the katabatic jet which is summarized conceptually in Figure 4.5. Finally, the vertical structure all of the measured fluxes (figures 4.3 and 4.4) exhibit the common characteristic of varying by far more than 10% over the thin katabatic jet layer, with rather steep gradients. Hence, no semblance of a constant-flux layer is observed, and Monin-Obukhov

similarity theory is expected to break down for the katabatic flows investigated herein.

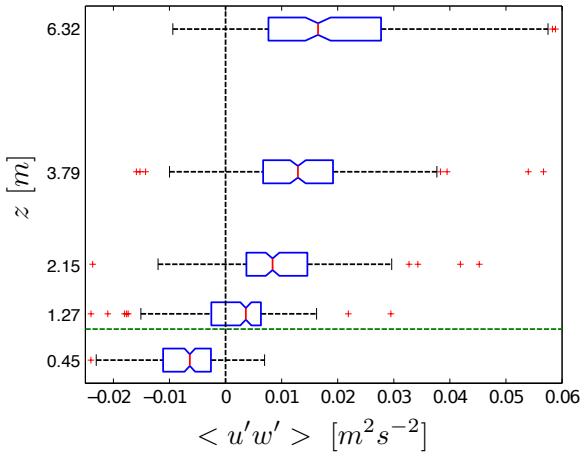

Figure 4.3 – Box plot profiles of the streamwise momentum flux. The dotted green line is the estimated height of the katabatic jet peak, or velocity maximum.

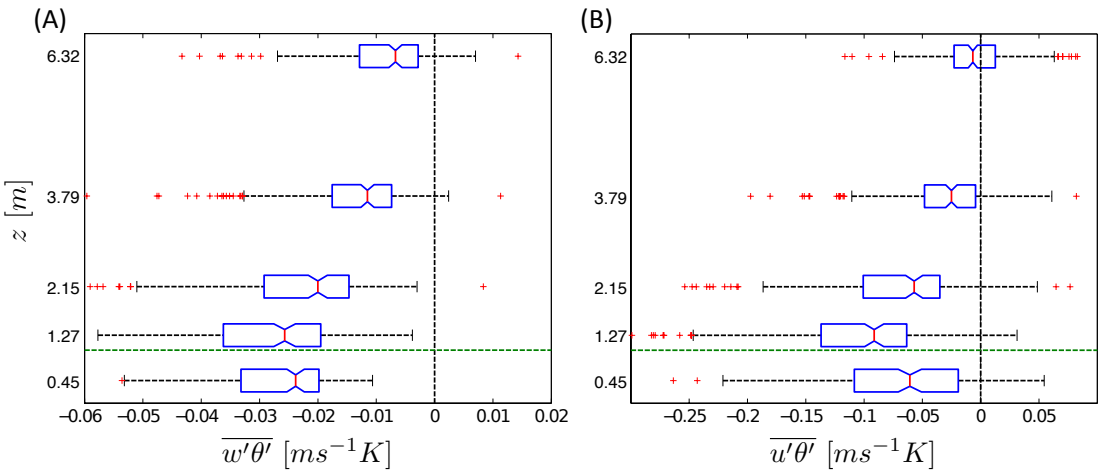

Figure 4.4 – Box plot profiles of the (A) slope-normal heat flux and (B) along-slope heat flux. The dotted green line is the estimated height of the katabatic jet peak, or velocity maximum.

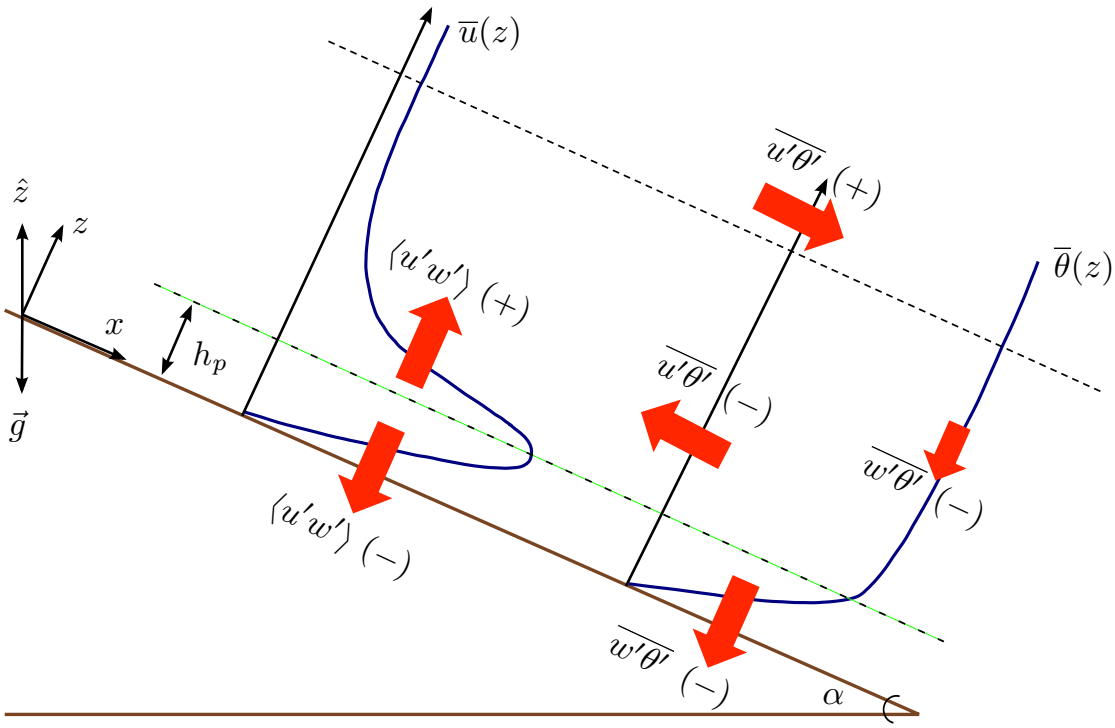

Figure 4.5 – Conceptual schematic summarizing the mean profiles, and turbulent mixing tendencies for steep slope katabatic flow.

4.4 Brief Overview of Monin-Obukhov Similarity Theory

In the context of flux-profile relations, or similarity functions that relate the turbulent fluxes of momentum and heat to the profiles of velocity and temperature, Monin-Obukhov similarity theory states that [Monin and Obukhov, 1959, Brutsaert, 2005]

$$\hat{\phi}_m(\hat{\zeta}) = \frac{\kappa \hat{z}}{u_*} \frac{\partial \langle u \rangle}{\partial \hat{z}}, \tag{4.1}$$

and

$$\hat{\phi}_h(\hat{\zeta}) = -\frac{\kappa \hat{z} u_*}{\overline{\hat{w}'\theta'}} \frac{\partial \bar{\theta}}{\partial \hat{z}}, \tag{4.2}$$

where $\hat{\phi}_m$ and $\hat{\phi}_h$ are the dimensionless gradients of the mean streamwise wind, $\langle u \rangle$, and virtual temperature, $\bar{\theta}$, respectively (reviewing the notation defined for this chapter: a 'hat' over a variable indicates the vertical-horizontal coordinate system where $\hat{z}$ is the vertical direction, and time averages are indicated by angle brackets in a streamwise-rotating coordinate system, and an over-line for a fixed coordinate system); the stability parameter, $\hat{\zeta} = \hat{z}/\hat{L}$ where $\hat{L}$ is the

Obukhov length, defined such that

$$\hat{\zeta} = \frac{\hat{z}}{\hat{L}} = \frac{\kappa \hat{z} g}{u_*^3} \frac{\overline{\hat{w}'\theta'}}{\bar{\theta}}; \tag{4.3}$$

the von Kármán constant is taken as $\kappa = 0.4$ and the friction velocity is $u_* = (\langle u'w' \rangle^2 + \langle v'w' \rangle^2)^{1/4}$. For flat terrain, a variety of relations for $\hat{\phi}_m(\hat{\zeta})$ and $\hat{\phi}_h(\hat{\zeta})$ have been empirically derived, the most historically famous of which are by Businger et al. [1971] and Dyer [1974], but many slight variations of these functions have been derived (e.g., Högström [1988], Grachev et al. [2007]), including extended stability functions (e.g., Cheng et al. [2005]) for strongly stable cases.

4.5 Local Monin-Obukhov Similarity Scaling for Steep Slope Katabatic Flow

This section focuses on local similarity scaling for the katabatic flow within the framework of Monin-Obukhov similarity theory. Nadeau et al. [2012] have evaluated the validity (or lack thereof) of local Monin-Obukhov similarity scaling for a steep slope for a single measurement height. The purpose of this section is to expand the analyses of Nadeau et al. [2012] to five measurement locations within the katabatic jet layer to determine if the locally scaled variables exhibit functional relations. Once scaled, comparisons between the behavior of the scaled field data and the traditional, flat-terrain similarity relations will be used to interpret turbulent mixing in the katabatic jet. For steeply sloping terrain it is important to distinguish whether similarity scaling variables are computed in a coordinate system aligned with the gravitational acceleration or the terrain because the difference between the vertical and slope-normal heat fluxes increase with increasing slope angle [Oldroyd et al., 2015 *in press*]. In a fixed, slope-defined coordinate system, as shown in Figure 4.1 with positive $\bar{u}$ directed downslope, the vertical heat flux is defined as $\overline{\hat{w}'\theta'} = \overline{w'\theta'}\cos\alpha - \overline{u'\theta'}\sin\alpha$, where α is the local slope inclination angle. The dimensionless gradients in Monin-Obukhov similarity theory (Equations 4.2 and 4.3) were written for the vertical reference frame. The dimensionless gradients and stability parameter transformed into the fixed the slope-define coordinate system are:

$$\phi_m(\zeta) = \frac{\kappa z}{u_*} \frac{\partial \langle u \rangle}{\partial z}, \tag{4.4}$$

and

$$\phi_h(\zeta) = -\frac{\kappa z u_*}{\overline{w'\theta'}} \frac{\partial \overline{\theta}}{\partial z}, \tag{4.5}$$

with

$$\zeta = \frac{z}{L} = \frac{\kappa z g}{u_*^3} \frac{\overline{w'\theta'}}{\overline{\theta}}. \tag{4.6}$$

Figure 4.6 shows the dimensionless gradients of streamwise velocity, $\langle u \rangle$, computed from the katabatic flow field data with local Monin-Obukhov similarity scalings and the flat-terrain stability functions by Högström [1988], Businger et al. [1971], Dyer [1974] and [Cheng et al., 2005] for comparison. This scaling framework for ϕ_m does reveal functional relations with stability. The most evident feature of Figure 4.6 is that ϕ_m changes sign depending on whether the measurement location is above or below the jet peak. Not surprisingly, this sign change in ϕ_m follows the sign change in $\partial\langle u \rangle/\partial z$ because u_* is always positive and does not track the corresponding sign change in the momentum flux seen in Figure 4.3. To analyzing how the data behave with increased stability in comparison to the flat-terrain relations, it is useful to rearrange the definition for ϕ_m (Equation 4.4):

$$u_* = \kappa z \frac{\partial \langle u \rangle}{\partial z} \frac{1}{\phi_m(\zeta)}. \tag{4.7}$$

When written in this form, $\partial\langle u \rangle/\partial z$, or the gradient, can be considered a 'potential' for mixing over a mixing length, κz, and $1/\phi_m(\zeta)$ can be viewed as a transfer coefficient, such that larger magnitudes of ϕ_m are associated with lower degrees of turbulent mixing. Through this lens, Figure 4.6 shows that both the katabatic data and the flat-terrain relations predict that turbulent mixing decreases with increasing stability (ζ), as expected. However, the ζ for which ϕ_m begins to increase more rapidly with increased stability is almost and order of magnitude higher in the katabic case. This likely means that additional turbulent mixing mechanisms are occurring over the steep slope than predicted for mixing over flat terrain. Qualitatively, Figure 4.6 shows remarkably similar trends in $\phi_m(\zeta)$ as observed in the katabatic flow measurements by Smeets et al. [1988] (in their Figure 11) andVan Der Avoird and Duynkerke [1999] (in their Figure 8) over glaciers with shallow slopes ($\sim 5°$) at Pasterze and Vatnajökull, respectively. More specifically, those studies also show that measured $\phi_m(\zeta)$ compares well with flat-terrain relations for approximately $0 < \zeta < 0.5$, and then is decreased compared to those predicted for flat terrain for stronger stabilities. This behavior is discussed again Section 4.8.

Similarly, Figure 4.7 shows the dimensionless gradients of virtual temperature, $\bar{\theta}$, computed from the katabatic flow field data with local Monin-Obukhov similarity scalings and the flat-terrain stability functions by Högström [1988], Businger et al. [1971], Dyer [1974] and [Cheng et al., 2005] for comparison. Again, it appears that a functional relation with stability exists for ϕ_h for the steep-slope katabatic flow. However, strikingly in this case, the data show almost an inverse behavior to those seen in the flat-terrain relations. As was done for $\phi_m(\zeta)$ the definition of the similarity scaling for the dimensionless virtual temperature gradient can be arranged,

$$\overline{w'\theta'} = -\kappa z u_* \frac{\partial \overline{\theta}}{\partial z} \frac{1}{\phi_h(\zeta)}, \tag{4.8}$$

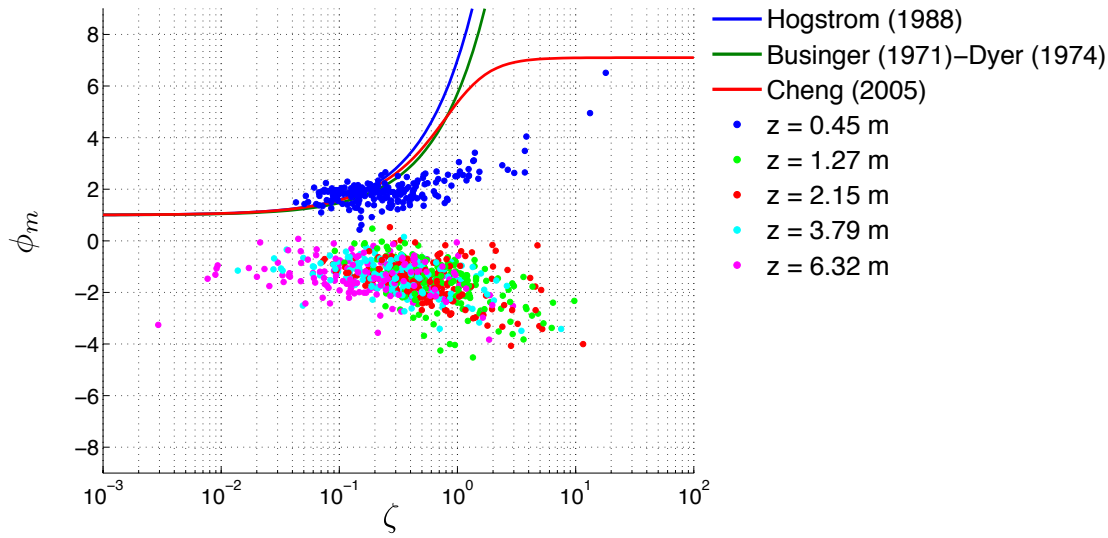

Figure 4.6 – Dimensionless gradients of streamwise velocity for the katabatic flow computed with local Monin-Obukhov similarity scalings, along with the flat-terrain stability functions by Högström [1988], Businger et al. [1971], Dyer [1974] and [Cheng et al., 2005].

such that larger magnitudes in ϕ_h are associated with lesser degrees of turbulent mixing. With this perspective, the katabtic data in Figure 4.7 reveal that more turbulent mixing is occurring over the steep slope than expected for flat terrain at moderate to high stabilities, as seen for ϕ_m. However, the katabatic data for ϕ_h also show extremely counterintuitive behavior in that they actually exhibit *increased mixing with increasing stability*. Qualitative comparisons with katabatic measurements over glaciers potentially show similar trends in $\phi_h(\zeta)$. The measurements by Van Der Avoird and Duynkerke [1999] (in their Figure 9) show a large degree of scatter and a narrow range of ζ so it is unclear if their results are more similar those presented herein or to the flat-terrain relation. However the results presented by Smeets et al. [1988] (in their Figure 11) also show ϕ_h decreasing with increasing ζ, but at again for a more narrow range of ζ than observed for the steep slope. The turbulent mixing in steep-slope katabatic flow is discussed in more detail in Sections 4.6 and 4.8.

In addition to the flat terrain relations, Łobocki [2013] and Denby [1999] have generated simulated similarity relations specifically for katabatic flow within the Monin-Obukhov scaling framework using modified Mellor-Yamada type models [Mellor and Yamada, 1982]. The Łobocki [2013] model essentially transforms the Mellor-Yamada model into a slope-defined coordinate system such that the buoyancy terms include the $\overline{u'\theta'}\sin\alpha$ component. This model was then run over a wide range of slope angles (0° to 25°) to produce a family of α-dependent similarity relations for katabatic flow (see Łobocki [2013] Figure 2). This family of $\phi_h(\zeta)$ functions all show increasing ϕ_h (decreasing mixing) with increasing stability in contrast to Figure 4.7. However, according to this Łobocki [2013] family of curves, the effect of

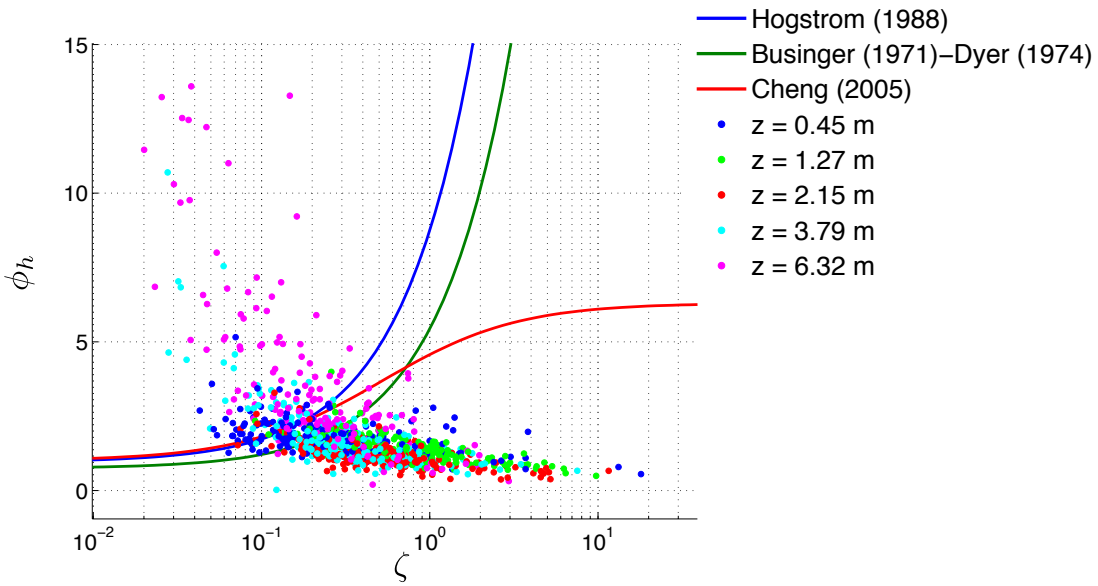

Figure 4.7 – Dimensionless gradients of virtual temperatur for the katabatic flow computed with local Monin-Obukhov similarity scalings, along with the flat-terrain stability functions by Högström [1988], Businger et al. [1971], Dyer [1974] and [Cheng et al., 2005].

increasing α is to slightly decrease $\phi_h(\zeta)$ (increase turbulent mixing).

The Denby [1999] model included slope angle dependence in various terms of the second-order closure schemes and tested the model sensitivity to two different viscous dissipation closures. Model runs were compared to measurements made for katabtic flows over glaciers and icesheets in the context of test flux-gradient similarity. Modeled ϕ_h from Denby [1999] are also characterized by more turbulent mixing (lower ϕ_h) than the flat-terrain solutions, but they plateau with increased stability. In his comparison to the glacier and ice sheet measurements, Denby [1999] states that the measurements show mostly scatter and no clear dependence on stability. However, in comparing Figure 4.7 with the Pasterze Glacier ($\alpha = 4°$) measurements (see also Smeets et al. [1988]) for $\phi_h(\zeta)$ in Figure 6(b) from Denby [1999], the glacier measurements show a similar trend of ϕ_h decreasing (turbulent mixing increasing) with stability, though with more scatter.

In addition to the measurements from the Pasterze Glacier [Smeets et al., 1988], a recent investigation of local Monin-Obukhov similariy scaling for the transitional periods [Jensen et al., 2014] also shows a trend similar to that in Figure 4.7 for $\phi_h(\zeta)$ in the stable regime. In this case, the measurements were made over a shallow mountain slope ($\alpha = 4°$) [Grachev et al., 2015 *in press*]. Hence, some observational evidence exists (even for relatively shallow slopes katabatic flow), that support the trends observed in $\phi_h(\zeta)$ for the steep alpine slope.

Since Figures 4.6 and 4.7 show functional relations in $\phi_m(\zeta)$ and $\phi_h(\zeta)$ (though with scatter), and some evidence exists that the behavior may be transferrable to other sites, functional fits

of the data were performed to propose similarity scaling functions for katabatic flow. These fits were performed using a so called *robust* least-squares regression scheme, for which extraneous data points are weighted less heavily into the fitting statistics.

Figure 4.8(A) shows the empirical fits of $\phi_m(\zeta)$ for the steep-slope katabatic flow along with binned medians of the data. In addition, Figures 4.8(B) and (C) show scatter plots for measured u_* and modeled u_* using the empirical katabatic relations and the Businger-Dyer [Businger et al., 1971, Dyer, 1974] relations (with $|\partial\langle u\rangle/\partial z|$, and calculated locally from the data, not iteratively), respectively. The Businger-Dyer [Businger et al., 1971, Dyer, 1974] relations were chosen for comparison because they (and other flat-terrain relations) are widely used as wall models in numerical simulations even for sloping terrain. The root-mean-square (RMS) differences between modeled and measured u_* for the Businger-Dyer relation is 0.063 ms^{-1} compared to 0.05 ms^{-1} for the slope relations. For a typical value ($u_* = 0.1$ms^{-1}) these RMS differences translate into a 50% error for the slope relations and 63% errors for the Businger-Dyer relation. For u_* the statistical improvement in RMS difference from using the slope relations is not huge. However, the Businger-Dyer relation tends to systematically underestimate u_*, whereas the the scatter in using the slope relations is more centered around the 1:1 line, indicating little to no bias. In visually inspecting Figure 4.6 this comparable RMS difference between model choice is not surprising. It may also help explain why using Monin-Obukhov similarity to set the mixing length in the closure model for the 1D momentum balance presented in Chapter 3 still produces reasonable results despite high momentum flux gradients. In addition, much of the data cloud in 4.6 resides in the stability range for which $\phi_m(\zeta)$ is relatively flat. If more of the data points were to lie in the more strongly stable regime ($\zeta > 0.5$) then the RMS difference using the Businger-Dyer relation would likely be a lot greater. It is possible that some conditional sampling may decrease the scatter and uncertainty in predicting u_*.

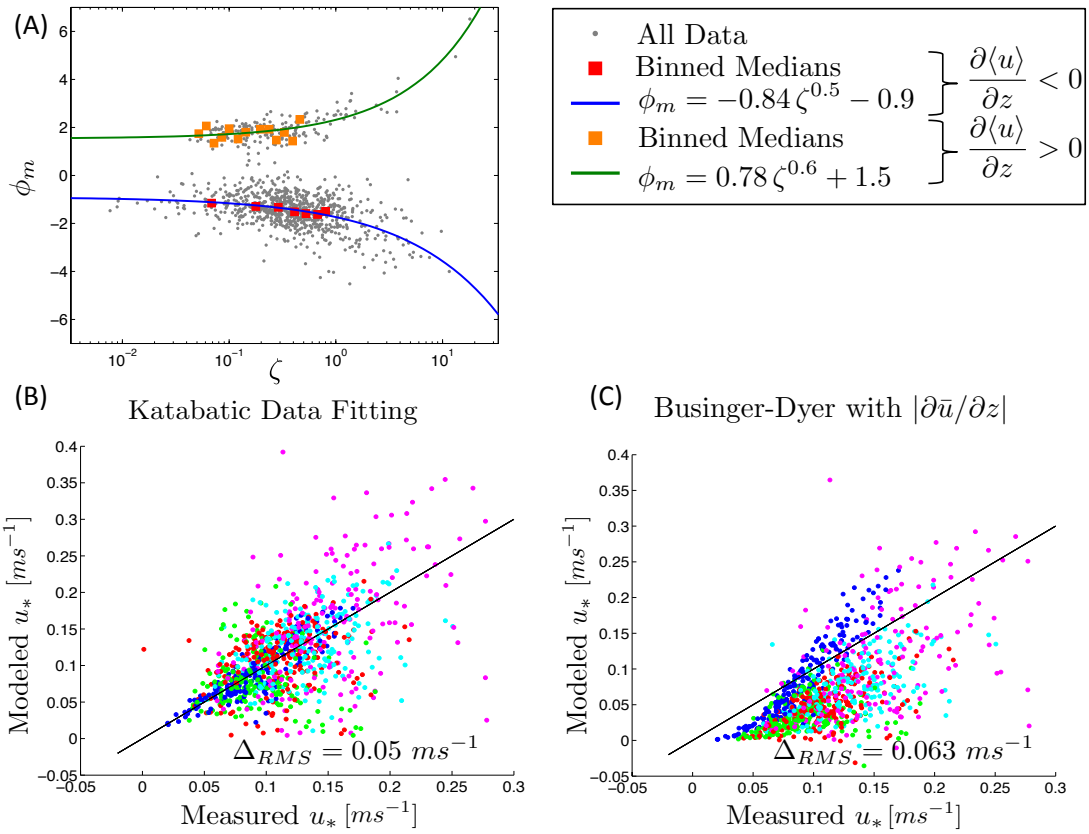

Figure 4.8 – (A) Empirically derived fits of $\phi_m(\zeta)$ for a steep-slope katabatic flow along with binned medians of the data. Scatter plots of measured u_* and modeled u_* using (B) the empirical relations and (C) the Businger-Dyer relation with $|\partial\langle u\rangle/\partial z|$. The various colors for data points in plots (B) and (C) correspond to the five sensor heights as in the legend of Figure 4.6 and the solid line represents a 1:1 correlation.

Similarly, Figure 4.9(A) shows the empirical fits of $\phi_h(\zeta)$ for the steep-slope katabatic flow along with binned medians of the data. Scatter plots, along with RMS differences for measured $\overline{w'\theta'}$ and modeled $\overline{w'\theta'}$ using the empirical relation for katabatic flow and the Businger-Dyer [Businger et al., 1971, Dyer, 1974] relation are shown in Figure 4.9 (B) and (C), respectively. In this case, the improvement in RMS difference by employing the empirical katabatic relation (Δ_{RMS} = 0.0078 ms^{-1}K) for ϕ_h over the Businger-Dyer relation (Δ_{RMS} = 0.017 ms^{-1}K) is quite significant. Assuming a typical value, ($\overline{w'\theta'}$ = 0.02 ms^{-1}K), these RMS differences translate into 39% (for the slope relation) and 85% (for the Businger-Dyer relation) differences. Again, the scatter around the 1:1 line for the empirical relation shows almost no bias, whereas the scatter in for the Businger-Dyer relation would tend to underestimate the magnitude of $\overline{w'\theta'}$ especially in the bulk of the katabatic jet. Visually inspecting Figure 4.7, shows approximately a decade of stabilities ($0.005 < \zeta < 0.05$) for which the Businger-Dyer relation might provide reasonable estimations of $\overline{w'\theta'}$. However for stabilities approaching neutral or more strongly stable, it would likely provide a gross overestimation or underestimation of the flux magnitude, respectively.

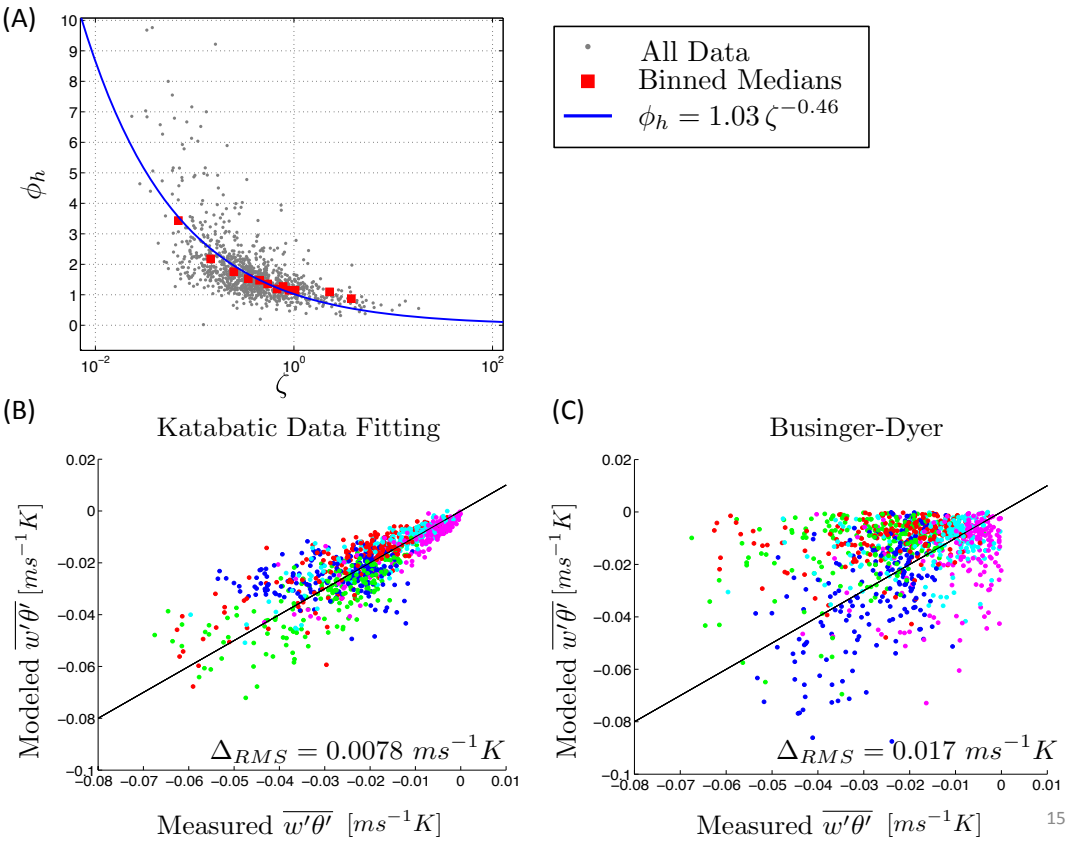

Figure 4.9 – A) Empirically derived fits of $\phi_h(\zeta)$ for a steep-slope katabatic flow along with binned medians of the data. Scatter plots of measured $\overline{w'\theta'}$ and modeled $\overline{w'\theta'}$ using (B) the empirical relation and (C) the Businger-Dyer relation. The various colors for data points in plots (B) and (C) correspond to the five sensor heights as in the legend of Figure 4.7 and the solid line represents a 1:1 correlation.

4.6 Turbulent Mixing and the Role of TKE

To better understand the phenomenon of increased turbulent mixing with increasing stability, as evidenced most notably in Figure 4.7, it is useful to examine the role of buoyancy over a steep slope. The buoyant production (+) or destruction (−) of turbulence kinetic energy (TKE) is defined as $\left(g/\bar{\theta}\right)\overline{\hat{w}'\theta'}$ [Stull, 1988]. In a fixed slope-defined coordinate system this becomes [Oldroyd et al., 2015 *in press*],

$$\frac{g}{\bar{\theta}}\overline{\hat{w}'\theta'} = \frac{g}{\bar{\theta}}(\overline{w'\theta'}\cos\alpha - \overline{u'\theta'}\sin\alpha). \tag{4.9}$$

This equation shows that the slope angle, α determines the relative contributions from the slope-normal ($\overline{w'\theta'}$) and along-slope ($\overline{u'\theta'}$) heat flux components to the vertical heat flux and buoyant production/destruction of TKE. Figure 4.10 shows box plot profiles of the vertical heat flux, $\overline{\hat{w}'\theta'}$. It shows that for the majority of the jet layer $\overline{\hat{w}'\theta'}$ is positive, indicating *production* of TKE, in spite of atmospheric stability. Recall the box plot profiles of $\overline{w'\theta'}$ and $\overline{u'\theta'}$ shown in Figure 4.4. As discussed previously, a negative $\overline{u'\theta'}$ in the fixed, slope-defined coordinate system with positive $\bar{u}$ directed down the slope corresponds to an upslope heat flux. Hence as α increases, the relative contribution from the negative, destructive component of TKE, $\left(g\cos\alpha/\bar{\theta}\right)\overline{w'\theta'}$, decreases, and the the relative contribution from the upslope, producing component of TKE $\left(-g\sin\alpha/\bar{\theta}\right)\overline{u'\theta'}$ increases. So for sufficiently steep slopes under stable conditions, surface-normal, buoyant destruction of TKE is overcome by along-slope, buoyant production of TKE, resulting in a net positive vertical buoyancy, and net production of TKE. This effect of the terrain slope tilting the 'horizontal' heat flux until TKE production was theoretically predicted to occur for steep slopes by Horst and Doran [1988] and Denby [1999]. However to our knowledge, this effect has not been shown before with measurements of katabatic flow. The buoyant production of TKE in steep-slope katabatic flow certainly helps to explain the functional behavior seen $\phi_h(\zeta)$. However, it is unclear if it accounts for all of the increased mixing observed, or if other energetics are contributing to this mixing phenomenon.

4.7 Along-Slope Heat Flux

Much less has been reported regarding the along-slope component of the heat flux in comparison to the slope-normal or vertical components. This is probably because there is little discussion regarding $\overline{u'\theta'}$ in ABL theory generally (one exception is from Wyngaard et al. [1971]), since this term in the governing equations is usually neglected in horizontal homogeneity assumptions over flat terrain. However, Horst and Doran [1988] theorize that the sign of the along-slope heat flux should change with the sign of the momentum flux at the jet peak and a recent experimental study confirms this behavior for shallow slope angles Grachev et al. [2015 *in press*]. However, in this study of steep-slope katabatic flows the observed sign change in $\overline{u'\theta'}$ occurs well above the jet peak. Potentially, other energetics such as turbulent transport are at play for the steep-slope case. In fact, the counter-gradient heat flux and

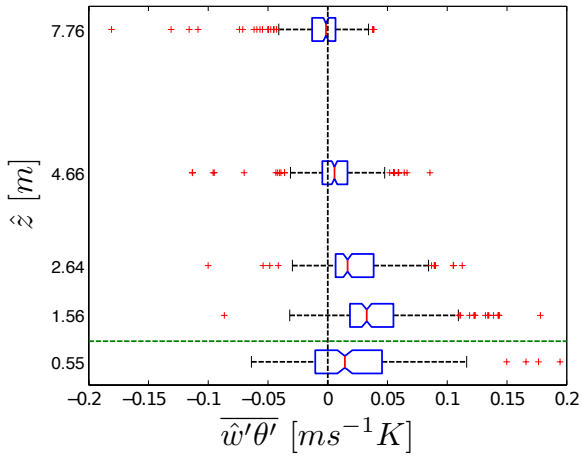

Figure 4.10 – Vertical heat flux, associated with buoyant production (+)/destruction (−) of TKE. Notice the measurement location heights, $\hat{z}$, are reported here in the vertical coordinate system. The dotted green line is the estimated height of the katabatic jet peak.

nonmonotonicity observed in profiles of $\overline{w'\theta'}$ (Figure 4.4(A)) may also suggest this. Denby [1999] suggests that turbulent transport terms are important mechanisms in the katabatic jet, especially at the jet peak where the momentum flux, shear production go to zero. However, considering the functional relations $\phi_m(\zeta)$ and $\phi_m(\zeta)$ that the katabatic data present herein show, if turbulent transport plays a role, it too should be a function of ζ. The specific roles of turbulent transport in mixing within the katabic jet are a subject of future research.

Nevertheless, since the along-slope heat flux is an important quantity in buoyant production of TKE over sloping terrain, it deserves some further investigation within the local scaling framework. In an attempt to find a functional flux-gradient scaling relation appropriate for $\overline{u'\theta'}$, many different scaling variables posed in different coordinate systems were tried, including the slope-normal virtual temperature gradient ($\partial\bar{\theta}/\partial z$), the valley scale lapse rate from ballon measurements and the along-slope virtual temperature gradient ($\partial\bar{\theta}/\partial x$) estimated from a station downslope of the tower. The only scaling for $\overline{u'\theta'}$ that produces a clear functional relation is through using the vertical coordinate system, vertical stability parameter, $\hat{\zeta}$, and vertical virtual temperature gradient, $\partial\bar{\theta}/\partial\hat{z}$, such that

$$\phi_{hx}(\hat{\zeta}) = \frac{\kappa\hat{z}u_*}{\overline{u'\theta'}}\frac{\partial\overline{\theta}}{\partial\hat{z}}. \tag{4.10}$$

With this scaling, it does not make sense to call ϕ_{hx} the dimensionless gradient of $\partial\bar{\theta}/\partial x$ or $\partial\bar{\theta}/\partial\hat{z}$. However, what Equation 4.10 does imply is that if a functional relationship does exist then $\overline{u'\theta'}$ is controlled by the local gradient of $\partial\bar{\theta}/\partial\hat{z}$.

Figure 4.11 shows the measured $\phi_{hx}(\hat{\zeta})$ as scaled by Equation 4.10 for the steep-slope katabatic flow. Akin to the TKE production term over a steep slope, $\hat{\zeta}$ now contains components of

the slope-normal and along-slope heat fluxes needed to calculate the vertical heat flux (see Equation 4.3). Therefore, most of the measured $\hat{\zeta}$ now reside in the *unstable* regime. This is again counterintuitive because $\partial\bar{\theta}/\partial\hat{z}$ remains classified as stable stratification, and care must now be taken to specify the definition of the stability parameter when discussing stability. Another interesting feature in Figure 4.11 is that the asymptotic behavior that was observed in $\phi_h(\zeta)$ to be associated with neutral ζ (as in Figure 4.7) is shifted into the stable $\hat{\zeta}$ regime. This suggests again that other (extra) energetics are at play in the katabatic jet, but that they are related to ζ or $\hat{\zeta}$.

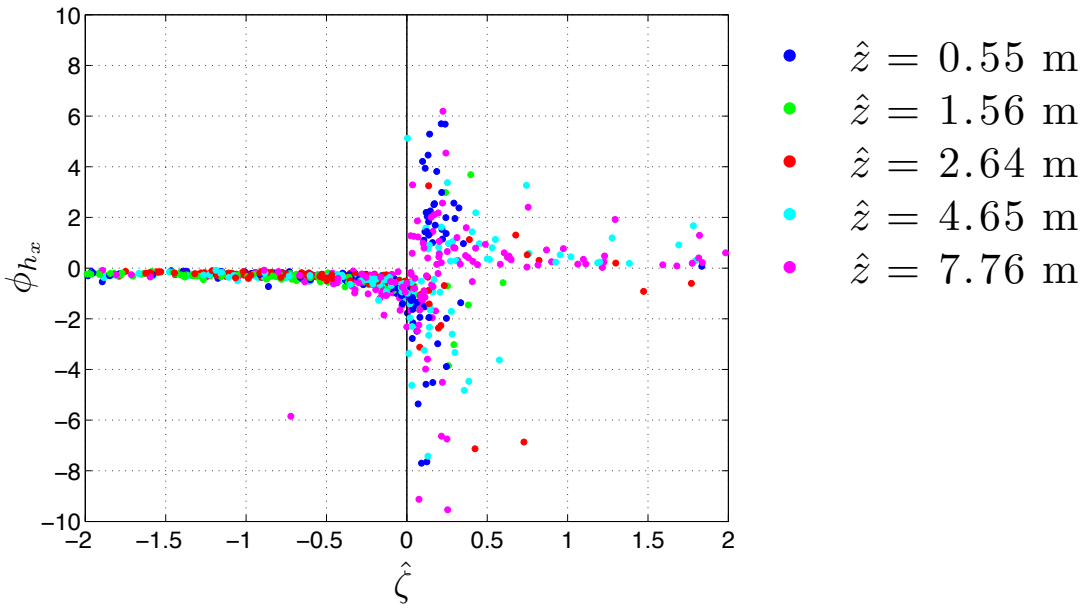

Figure 4.11 – Locally scaled along-slope heat flux, $\phi_{hx}(\hat{\zeta})$ as defined in Equation 4.10 as a function of the vertically computed stability parameter, $\hat{\zeta}$.

4.8 Future Work

It has been shown that production of TKE, despite stable stratification, occurs in the steep-slope katabatic flow. Future work should clearly address the ramifications of TKE production over a steep slope (and reduction over shallower slopes) to the surface energy budget. This is one of the more important implications of this results.

Additionally, it is unclear if turbulent transport terms also play a significant role or if this 'extra' TKE can account for: (i) all of the mixing observed in $\phi_m(\zeta)$ and especially $\phi_h(\zeta)$, (ii) the counter gradient fluxes observed in the vertical structure of the slope-normal heat flux, and (iii) the shifted asymptote observed in the local scaling for the along-slope heat flux. The observations by Smeets et al. [1988] and Van Der Avoird and Duynkerke [1999] show similar trends in $\phi_m(\zeta)$ and $\phi_h(\zeta)$ for katabatic flows over glaciers, where the slope angles are not sufficiently steep to

actually induce production of TKE (though they should still observe a reduced suppression of TKE in comparison to flat terrain with the same stratification). This implies that turbulent transport plays a significant role in increasing turbulent mixing (decreasing ϕ_m and ϕ_h) in a katabatic flow. Smeets et al. [1988] hypothesize that the deviations from flat-terrain relations observed in $\phi_m(\zeta)$ and $\phi_h(\zeta)$ for stronger stabilities come from low-frequency perturbations at higher stabilities. Högström [1990] (for flat terrain) attributed deviations from the traditional flux-profile relations to non-local turbulent transport, or 'inactive turbulence', which can distribute 'extra' energy into the horizontal components; however, these deviations are less pronounced than what is observed over the slope. Both concepts, low-frequency perturbations and non-local turbulent transport (potentially the same concept depending on the scales), were posed by the respective authors as mechanisms which occur from aloft [Smeets et al., 1988, Högström, 1990]. However, if these mechanisms were to occur from aloft, or are *detached* from the surface, then they would not be expected to have a functional relation with the local gradients, as has been shown herein for the steep, alpine slope.

Future work in the context of similarity scaling for katabatic flow should investigate the role of nonlocal turbulent transport and how it behaves at various scales, how it behaves with stability, its vertical structure, and its relative importance in budgets of TKE and $\overline{u'\theta'}$. The current hypothesis is: nonlocal turbulent transport *is* a significant mixing mechanism in katabatic jets, but instead of coming from aloft, it is associated with the katabatic jet itself, and transported along slope. If this were the case, then the transport mechanisms would be more likely to scale with the local gradients, as observed.

4.9 Conclusions

The objectives of this chapter were to evaluate local Monin-Obukhov similarity scaling for katabatic flow over a steep, alpine slope by expanding the work by Nadeau et al. [2012] to determine if clear functional relations exist within this scaling framework. Box plots profiles of the measured fluxes in the katabatic jet paint a complicated picture of turbulent exchange over a remarkably thin layer. These flux profiles are characterized by steep gradients, and non-monotonicity in the cases of the heat fluxes. Theory by Horst and Doran [1988] and observations by Grachev et al. [2015 *in press*] suggest that the sign of the along slope heat flux, $\overline{u'\theta'}$, should change with the sign change in the momentum flux $\overline{u'\theta'}$. This was not observed for the steep, alpine slope where the sign change in $\overline{u'\theta'}$ occurs in the upper part of the katabatic layer, resulting in an upslope heat flux over nearly the entire jet layer. The non-monotonicity observed in the slope-normal heat flux, $\overline{w'\theta'}$, is associated with a counter-gradient behavior below the jet peak. These characteristics observed in the heat fluxes suggest that turbulent transport may play a significant role in the katabatic jet for scalar transport, but perhaps less of a role in mixing momentum.

The measured dimensionless wind shear, $\phi_m(\zeta)$, and virtual temperature, $\phi_h(\zeta)$ deviate from the so-called 'universal' functions for flat terrain; however, they do reveal functional relations

with varying stability parameter that qualitatively compare quite well with observations by Smeets et al. [1988] and Van Der Avoird and Duynkerke [1999] of katabatic flows over more shallowly-sloped glaciers. The measured $\phi_m(\zeta)$ and $\phi_h(\zeta)$ were used to propose flux-profile similarity functions appropriate for katabatic flow. The behavior of these functions predicts that more turbulent mixing occurs in the katabatic flows than would occur over flat terrain with at the same stability for $\zeta > 0.5$. The observed $\phi_m(\zeta)$ qualitatively compares quite well to the flat terrain relations for $\zeta < 0.5$, however to compare with the flat terrain solutions the absolute value of $\partial\langle u\rangle/\partial z$ must be used in the scaling arguments because u_* is always positive. The RMS differences between measured u_* and modeled u_* for the katabatic relations posed herein and the flat-terrain relation from Businger-Dyer [Businger et al., 1971, Dyer, 1974], $\Delta_{RMS} = 0.05$ ms^{-1} and $\Delta_{RMS} = 0.063$ ms^{-1}, respectively, show only a slight statistical improvement. However, this improvement is likely to increase significantly for more strongly stable cases and more strict conditional sampling. In addition, the Businger-Dyer relation tends to systematically under-predict u_*.

Quite strikingly for the katabatic flow observations, behavior of $\phi_h(\zeta)$ decreasing with in increasing stability suggests that turbulent mixing actually increases with increasing stability. Hence, the improvement in RMS differences between measured and modeled $\overline{w'\theta'}$ by using the katabatic similarity relation ($\Delta_{RMS} = 0.0078$ ms^{-1}K) over the flat-terrain relation of Businger-Dyer [Businger et al., 1971, Dyer, 1974] ($\Delta_{RMS} = 0.017$ ms^{-1}K) is significant. In addition, the Businger-Dyer relation tends to systematically under-predict the magnitude of $\overline{w'\theta'}$ in the bulk portion of the jet layer.

Some of this increased mixing observed for the katabatic jet can be attributed to the presence of a tilted underlying surface. Analysis of the buoyancy term in TKE budget equation shows that in spite of a stability, buoyancy actually produces TKE for the steep slope katabatic flow. This production arises from the increased contribution of the upslope heat flux component to the vertical heat flux via $\sin\alpha$. For flat-terrain this contribution is zero, and for shallow slopes this contribution reduces the buoyant suppression of TKE. For steep slopes the production of TKE despite stability was theorized by Horst and Doran [1988] and Denby [1999], but to our knowledge has not previously been shown to occur with measurements. This production of TKE can explain at least some of the increased mixing observed in the katabatic flow compared to the flat terrain predictions. However, similar trends were shown in $\phi_m(\zeta)$ and $\phi_h(\zeta)$ observed by Smeets et al. [1988] and Van Der Avoird and Duynkerke [1999] for much shallower slopes, over which TKE production is not likely to occur. This again, suggests that turbulent transport terms are playing a significant role in mixing katabatic flows. However, $\phi_m(\zeta)$ and $\phi_h(\zeta)$ show clear functionalities, implying that if turbulent transport does play a significant role, it is likely related to local gradients. Investigating these hypotheses is aim of ongoing and future research into steep-slope katabatic flow. Potentially, one of the largest ramifications of this investigation is how the buoyant production of TKE over steep slopes, despite stable stratification, will ultimately affect the surface energy budget. This is a crucial topic of future research.

Bibliography

K Babić, Z Bencetić Klaić, and Ž Večenaj. Determining a turbulence averaging time scale by fourier analysis for the nocturnal boundary layer. *Geofizika*, 29(1):35–51, 2012.

W Brustaert. *Evaporation into the atmosphere, theory, history and application*. Kluwer Academic Publishers, 1982.

W Brutsaert. Land-surface water vapor and sensible heat flux: Spatial variability, homogeneity, and measurement scales. *Water Resour Res*, 34(10):2433–2442, 1998.

W Brutsaert. *Hydrology: an introduction*. Cambridge University Press, Cambridge, UK, 2005.

JA Businger, JC Wyngaard, Y. Izumi, and EF Bradley. Flux-profile relationships in the atmospheric surface layer. *J Atmos Sci*, 28(2):181–189, 1971.

Y Cheng, MB Parlange, and W Brutsaert. Pathology of Monin-Obukhov similarity in the stable boundary layer. *J Geophys Res*, 110(D6):D06101, 2005.

B Denby. Second-order modelling of turbulence in katabatic flows. *Boundary-Layer Meteorol*, 92(1):65–98, 1999.

AJ Dyer. A review of flux-profile relationships. *Boundary-Layer Meteorol*, 7(3):363–372, 1974.

HJS Fernando and ER Pardyjak. Field studies delve into the intricacies of mountain weather. *Eos Trans AGU*, 94(36):313–315, 2013.

HJS Fernando, ER Pardyjak, S Di Sabatino, FK Chow, SFJ De Wekker, SW Hoch, JP Hacker, JC Pace, T Pratt, Z Pu, WJ Steenburgh, CD Whiteman, Y Wang, D Zajic, BB Balsley, R Dimitrova, GD Emmitt, CW Higgins, JCR Hunt, JG Knievel, D Lawrence, Y Liu, DF Nadeau, E Kit, Blomquist BW, Conry P, Coppersmith RS, Creegan E, Felton M, Grachev AA, N Gunawardena, C Hang, CM Hocut, G Huynh, ME Jeglum, D Jensen, V Kulandaivelu, M Lehner, LS Leo, D Liberzon, JD Massey, K McEnerney, S Pal, T Price, M Sghiatti, Z Silver, M Thompson, H Zhang, and T Zsedrovits. The MATERHORN – unraveling the intricacies of mountain weather. *B Am Meteorol Soc*, 2015 *in press*.

T Foken. 50 years of the Monin–Obukhov similarity theory. *Boundary-Layer Meteorol*, 119(3): 431–447, 2006.

Thomas Foken. *Micrometeorology*. Springer, 2008.

AA Grachev, LS Leo, S Di Sabatino, HJS Fernando, ER Pardyjak, and CW Fairall. Structure of turbulence in katabatic flows below and above the wind-speed maximum. *Boundary-Layer Meteorol*, 2015 *in press*.

Andrey A Grachev, Edgar L Andreas, Christopher W Fairall, Peter S Guest, and P Ola G Persson. Sheba flux–profile relationships in the stable atmospheric boundary layer. *Boundary-Layer Meteorol*, 124(3):315–333, 2007.

B Grisogono and J Oerlemans. Katabatic flow: analytic solution for gradually varying eddy diffusivities. *J Atmos Sci*, 58(21):3349–3354, 2001.

U Högström. Non-dimensional wind and temperature profiles in the atmospheric surface layer: A re-evaluation. *Boundary-Layer Meteorol*, 42:55–78, 1988.

U Högström. Analysis of turbulence structure in the surface layer with a modified similarity formulation for near neutral conditions. *J Atmos Sci*, 47(16):1949–1972, 1990.

U Högström. Review of some basic characteristics of the atmospheric surface layer. *Boundary-Layer Meteorol*, 78:215–246, 1996.

TW Horst and JC Doran. The turbulence structure of nocturnal slope flow. *J Atmos Sci*, 45(4): 605–616, 1988.

D Jensen, ER Pardyjak, and SW Hoch. Monin-Obukhov similarity scaling over contrasting surfaces during the morning and evening transition. San Diego, CA, 18-22 August 2014. American Meteorology Society,16th Conference on Mountain Meteorology.

DD Jensen, ER Pardyjak, DF Nadeau, and SW Hoch. Observations of near-surface heat flux and temperature profiles through the early evening transition over contrasting surfaces. *Boundary-Layer Meteorol*, 2015 *in press*.

C Johansson, AS Smedman, U Högström, JG Brasseur, and S Khanna. Critical test of the validity of Monin-Obukhov similarity during convective conditions. *J Atmos Sci*, 58(12):1549–1566, 2001.

JC Kaimal and JJ Finnigan. *Atmospheric boundary layer flows: their structure and measurement*. Oxford University Press, 1994.

L Łobocki. Surface-layer flux–gradient relationships over inclined terrain derived from a local equilibrium, turbulence closure model. *Boundary-Layer Meteorol*, pages 1–15, 2013.

L Mahrt. Stratified atmospheric boundary layers and breakdown of models. *Theor Comp Fluid Dyn*, 11(3):263–279, 1998.

L Mahrt. Stably stratified atmospheric boundary layers. *Annu Rev Fluid Mech*, 46(1):23–45, 2014. doi: 10.1146/annurev-fluid-010313-141354. URL http://dx.doi.org/10.1146/annurev-fluid-010313-141354.

L Mahrt, D Vickers, R Nakamura, MR Soler, J Sun, S Burns, and DH Lenschow. Shallow drainage flows. *Boundary-Layer Meteorol*, 101(2):243–260, 2001.

GL Mellor and T Yamada. Development of a turbulence closure model for geophysical fluid problems. *Rev Geophys Space Phys*, 20(4):851–875, 1982.

AS Monin and AM Obukhov. Basic laws of turbulent mixing in the surface layer of the atmosphere. *Contrib Geophys Inst Acad Sci USSR151*, 24(151):163–187, 1959.

DF Nadeau, ER Pardyjak, CW Higgins, and MB Parlange. Similarity scaling over a steep alpine slope. *Boundary-Layer Meteorol*, 147(3):401–419, 2012.

DF Nadeau, ER Pardyjak, CW Higgins, H Huwald, and MB Parlange. Flow during the evening transition over steep alpine slopes. *Q J Roy Meteorol Soc*, 139(672):607–624, 2013. ISSN 1477-870X. doi: 10.1002/qj.1985. URL http://dx.doi.org/10.1002/qj.1985.

HJ Oldroyd, G Katul, ER Pardyjak, and MB Parlange. Momentum balance of katabatic flow on steep slopes covered with short vegetation. *Geophys Res Lett*, 2014.

HJ Oldroyd, ER Pardyjak, H Huwald, and MB Parlange. Adapting tilt corrections and the governing flow equations for steep, fully three-dimensional, mountainous terrain. *Boundary-Layer Meteorol*, 2015 *in press*.

IA Renfrew. The dynamics of idealized katabatic flow over a moderate slope and ice shelf. *Q J Roy Meteorol Soc*, 130(598):1023–1045, 2004.

ST Salesky and M Chamecki. Random errors in turbulence measurements in the atmospheric surface layer: Implications for monin-obukhov similarity theory. *J Atmos Sci*, 69(12), 2012.

CJPP Smeets, PG Duynkerke, and HF Vugts. Turbulence characteristics of the stable boundary layer over a mid-latitude glacier. part I: A combination of katabatic and large-scale forcing. *Boundary-Layer Meteorol*, 87(1):117–145, 1988.

CJPP Smeets, PG Duynkerke, and HF Vugts. Turbulence characteristics of the stable boundary layer over a mid-latitude glacier. part II: Pure katabatic forcing conditions. *Boundary-Layer Meteorol*, 97(1):73–107, 2000.

RB Stull. *An Introduction to Boundary Layer Meteorology*. Kluwer Academic publishers, 1988.

E Van Der Avoird and PG Duynkerke. Turbulence in a katabatic flow. *Boundary-Layer Meteorol*, 92(1):37–63, 1999.

D Vickers and L Mahrt. The cospectral gap and turbulent flux calculations. *J Atmos Ocean Tech*, 20(5):660–672, 2003.

D Vickers and L Mahrt. A solution for flux contamination by mesoscale motions with very weak turbulence. *Boundary-Layer Meteorol*, 118(3):431–447, 2006.

CD Whiteman. *Mountain Meteorology: Fundamentals and Applications*. Oxford University Press, USA, 2000.

JC Wyngaard, OR Coté, and Y Izumi. Local free convection, similarity, and the budgets of shear stress and heat flux. *J Atmos Sci*, 28(7):1171–1182, 1971.

5 Summarizing Conclusions and General Outlook

In this dissertation, turbulent exchange processes in alpine environments were investigated in juxtaposition to classical atmospheric boundary layer (ABL) theories and established practices, which were originally developed for flat, uniform and homogeneous terrain. Much of this work has focused on katabatic wind, a commonly occurring, yet physically unique flow regime that can develop via thermal forcing over sloping terrain. The occurrence of these flows is easy to predict, as they occur under conditions with clear skies, weak synoptic forcing and a stable stratification; however, for a variety of reasons they are notoriously difficult to model numerically, for example in weather prediction models. One reason in particular, is that turbulent exchanges over sloping terrain behave differently than those over flat terrain. A field measurement campaign in summertime 2011 was specifically aimed at studying the vertical structure of near-surface turbulent fluxes over a steep, alpine slope in Val Ferret, Switzerland. These measurements were used throughout this dissertation to analyze turbulent exchange in katabatic flow, as well as to address adaptations to common data treatment techniques that are required to obtain accurate flux estimates over steep and variable topography.

Chapter 1 introduced the important transport roles that turbulent exchange between the atmosphere and the underlying surface can play in the ABL. Also introduced were some of the physical complexities that mountainous environments present to ABL flows more generally, as well as to studying turbulence over complex topography. The principal physical mechanisms, and open questions associated with katabatic flow were also presented, along with their socio-economic and hydrometeorlogical pertinencies. Finally, the subsequent research objectives were outlined to address standard practices and classical theories that must be adapted or replaced to thoroughly investigate and predict ABL flows and turbulent exchange in mountainous regions.

Due to the stochastic nature of turbulence, many data processing techniques are required prior to analysis to obtain the best possible estimates of turbulent flux quantities. Chapter 2 addressed one such technique, the sector-wise planar fit (SPF) sensor tilt correction, and presented a methodology to optimize the SPF for fully three-dimensional terrain. To that end, cost functions were developed and shown to provide objective measures for selecting SPF

sector sizes and averaging times. Sensitivities in the turbulent momentum flux measured over mountainous terrain were used to quantify the possible consequences of implementing a non-optimized SPF. Particularly, selecting very small wind direction sector sizes or very long planar fit averaging times generated the largest errors in the momentum flux estimates because the subsequent data segments defining the tilt correction angles contained too much variability to produce representative streamlines. By contrast, the cost functions exhibited far fewer sensitivities to SPF input parameter for an idealized, flat site. This means that a single planar fit (as opposed to a sector-wise) is sufficient for that particular site. Chapter 2 also addressed complexities and the subsequent discrepancies found in the slope flow literature regarding the proper alignment of the buoyancy terms in the governing flow equations. We used measurements to show that the buoyancy terms in the mean momentum and turbulence kinetic energy budget equations must be adapted to rectify the misalignment with gravity when using a slope-normal/slope-parallel (SNSP) coordinate system. Moreover we showed that for sloping terrain the *apparent* slope angle changes with wind direction and that the effects of this geometrically-induced phenomenon must also be rectified in the governing equations. To address these concerns, we developed generalizing adaptations to the governing flow equations that contain additional components in the buoyancy terms, which properly account for gravitational effects regardless of the slope angle or wind direction.

Chapter 3 and Appendix A.1 presented a mechanistic study of katabatic flows to investigate the impacts of two dynamical processes which were not explicitly measured in the field experiments: the physical effects resulting from the presence of the underlying alpine grass canopy and larger-scale pressure perturbations. This study was performed via a one-dimensional mean momentum balance in consort with measurements to model the katabatic flow. Results showed that frictional and buoyant mechanisms constitute the principal momentum balance; however, contributions from the grass canopy and the modeled outer-layer pressure effects can be significant to the overall balance. More specifically, the larger-scale pressure effects were found to be more prominent under conditions with low wind speeds at the top of the katabatic layer, which are associated with high variability in wind direction. Additionally, we derived an analytical expression to estimate the jet peak height (the elevation of the velocity maximum) that revealed the presence of the grass canopy tends to reduce the jet peak height relative to a case where no grass canopy is present. Finally, the one-dimensional model was able to reproduce profiles of velocity and momentum flux that are comparable to those measured. This implies that Monin-Obukhov similarity theory, as applied in this model, is suitable for setting the stability adjusted mixing length in the turbulence closure model katabatic flow, at least over the range of stabilities tested via the measured temperature forcing. These results can be used to compliment classical wall-functions in large-scale numerical models of mountainous terrain, and aid in field experimental designs aimed at resolving the vertical turbulence structure of the katabatic jet.

Local Monin-Obukhov similarity scaling for katabatic flow was examined in Chapter 4 to investigate the governing turbulent exchange mechanisms in comparison (and in contrast) to the classical ABL theories. In contrast to those typically observed over flat terrain, the

measured turbulent fluxes exhibited a complicated vertical structure characterized by steep vertical gradients. This implies that Monin-Obukhov similarity theory is not appropriate for katabatic flows because the fluxes vary by far more than 10%. In fact, the observations showed that even local Monin-Obukhov similarity scaling for katabatic flows breaks down with respect to flux-profile relations developed for flat terrain. However, the observations exhibited clear functional relations with this scaling framework that were used to derive new, empirical flux-profile relations for katabatic flow, and which qualitatively compared well with observations obtained over glaciers of shallower slopes. These flux-profile relations indicate increased turbulent mixing in comparison to the flat-terrain relations. Furthermore, the observed slope-normal dimensionless gradients of virtual temperature, $\phi_h(\zeta)$, indicate increased mixing with increasing stability parameter, in stark opposition to conventional ABL theory. Some of this increased mixing can be attributed to the sloping terrain because positive contributions to the vertical heat flux by the along-slope heat flux (via the sine of the slope angle that is zero over flat terrain) reduce the buoyant suppression of turbulence kinetic energy (TKE) that occurs in a stable boundary layer. Moreover, for sufficiently steep slopes, as shown in this dissertation, these positive along-slope contributions overtake the negative contributions from the slope-normal component (which are also reduced via the cosine of the slope angle) to actually produce TKE via buoyancy, in spite of stability. This result, alone, has an enormous potential to significantly improve surface energy balance closures and hydrometeorological modeling for mountainous regions. Since the shallow-slope katabatic flows over glaciers exhibited similar functional trends for $\phi_h(\zeta)$, the extent to which the production of TKE accounts for all of the observed increases in turbulent mixing is unclear. Therefore, future work should explore possible contributions by non-local turbulent transport to increased mixing in katabatic flows, as well as the specific roles played the along-slope heat flux at various scales.

In summary, an urgent need for observational investigations focused on turbulent exchange processes in mountainous environments motivated this work. As shown herein, many of the classical ABL theories and data handling techniques are invalid or inapplicable over such terrain. However, to replace these traditional practices, we were able to develop new, alternative theories and techniques that are appropriate for mountainous terrain. First, the optimized SPF methodology was developed to provide a site-independent, quantitative procedure for selecting the proper sector sizes and averaging times in the SPF tilt corrections (see Chapter 2). Second, new adaptations to the governing flow equations provide generalizations that readily and correctly align gravity and the buoyancy terms for flows over sloping terrain regardless of wind direction (see Chapter 2). Third, a one-dimensional momentum balance model for katabatic flow that includes canopy and large-scale pressure effects provides an accessible platform for testing alternative, or possibly replacing traditional, wall models that link the surface conditions with atmospheric flows in large-scale numerical models of mountainous terrain (see Chapter 3). Fourth, new flux-profile relations for katabatic flow were empirically derived within the local Monin-Obukhov similarity scaling framework (see Chapter 4). Finally, we showed that the vertical turbulence structure in katabatic flows paints a far more

complicated picture of turbulent exchange in mountainous terrain than classical ABL theory would predict. An example of particular importance is shown in the measured net vertical buoyancy flux, which is positive over the majority of the katabatic layer, resulting in a net buoyant production of TKE despite stable stratification (see Chapter 4).

Overall, this dissertation has address some of the open questions regarding turbulent exchange over mountainous terrain. The vertical turbulence structure in the katabatic flow regime was the prevailing focus. However, mountainous regions present a whole host of flow regimes and multi-scale interactions needing immediate observational attention. For example many open questions remain that are related to turbulent exchange under the following mountain flow scenarios: anabatic flow regimes, transitional periods (between anabatic and katabatic regimes), and synoptic-scale and wave interactions with the turbulent surface exchanges and with each other (see also Appendix A.3). Fortunately, recent and burgeoning advancements in instrumentation and measurement techniques offer new and exciting capabilities to observe turbulence over a wide range of spatial and temporal scales. These new technologies offer practicality and promising outlooks to many mountain meteorological research needs and objectives that just a few years ago would have seemed optimistic at best. Hence with the proper attention and resources, new observational studies can begin to tackle the many open questions regarding turbulent exchanges over mountainous terrain.

A Appendices

A.1 Supporting Information for the Momentum Balance of Katabatic Flow

This appendix compiles the supplemental materials that were published online in *Geophysical Research Letters* along with the article presented in Chapter 3 having the following citation:

Oldroyd H.J., Katul G., Pardyjak E.R and Parlange M.B. Momentum balance of katabatic flow on steep slopes covered with short vegetation. *Geophysical Research Letters*, 41(13):4761–4768, 2014.

A.1.1 Summary of Supporting Information

Supporting materials include additional information about the sonic anemometer tilt corrections for the field experiment data in Section A.1.2 and the Tables A.1-A.3. More information about the field measurements from nine clear-sky nights in September of 2011 when downslope flow was observed, and that were used in conjunction with the model as described in the main article text is provided in Section A.1.3 and the corresponding Table A.4. Detailed information regarding the thermocouple temperature data is also compiled in this section. Statistical justification for the model assumption that $W = 0$ is provided in Section A.1.4. Additional figures that show the relationships between measured wind speed and wind direction statistics are Figure A.1, which repeats Figure 3b for the lowest four sensors, Figure A.2, which shows U and wind direction correlations for all sensor heights, and Figure A.3, which shows histograms of wind directions for all sensor heights.

A.1.2 Sensor Tilt Corrections

Due to terrain variably, a sector-wise planar fit tilt correction was implemented for evenly distributed 60° wind direction sectors. If a single planar fit (or double/triple rotation methods) is used, as opposed to a sector-wise approach, a bias in tilt angles for various wind directions becomes evident via scatter plots of W versus wind direction. This bias is due to deviations in the terrain from a perfect planar slope. Since according to *Wilczak et al. [2001]* , the planar fit generates a terrain-following, streamwise coordinate system, using the sector-wise planar fit approach with a sufficient number of sectors resulted in a removal of this bias and ensures that the data and model are presented in a common reference frame. Tables A.1-A.3 show the variability in tilt correction angles and planar-shift coefficients for all sonic anemometers and wind sectors. Note the mean downslope flow direct is 90° from North, so the majority of the experimental data reside in the 80° to 120° wind sector. Mean velocity and turbulent flux data within the 120° sectors located directly behind the sonic anemometers (120° - 240° from North) where flow distortion due to the tower and sensor booms is present, were excluded from the model analysis and results. However, they are included in the calculations of σ_{WD} because in a small percentage of cases the katabatic wind can come from these sectors (See also Figure A.3).

Table A.1 – Sector-wise planar fit pitch correction angles, α_w[°], for each sonic anemometer and wind direction sector specified by degrees from North.

Sector	z_1= 0.45 m	z_2= 1.27 m	z_3= 2.15 m	z_4= 3.79 m	z_5= 6.32 m
$80 < \phi \leq 120$	1.64	3.59	2.12	0.46	-1.79
$40 < \phi \leq 80$	0.11	4.02	1.10	-0.31	-0.97
$0 < \phi \leq 40$	2.52	5.79	2.54	0.83	-0.46
$320 < \phi \leq 360$	4.03	5.24	2.54	0.94	-0.60
$280 < \phi \leq 320$	5.06	4.61	3.35	1.86	-0.32
$240 < \phi \leq 280$	3.73	4.30	2.31	0.39	-0.52

Table A.2 – Sector-wise planar fit roll correction angles, β_w[°], for each sonic anemometer and wind direction sector specified by degrees from North.

Sector	z_1= 0.45 m	z_2= 1.27 m	z_3= 2.15 m	z_4= 3.79 m	z_5= 6.32 m
$80 < \phi \leq 120$	-17.56	-15.07	-14.40	-5.01	-2.83
$40 < \phi \leq 80$	-15.80	-14.56	-13.61	-4.97	-4.02
$0 < \phi \leq 40$	-15.54	-14.80	-13.71	-4.41	-3.09
$320 < \phi \leq 360$	-19.05	-14.85	-15.01	-4.98	-4.53
$280 < \phi \leq 320$	-15.95	-14.96	-14.42	-6.51	-4.48
$240 < \phi \leq 280$	-16.13	-10.03	-13.83	-3.15	-2.79

Table A.3 – Sector-wise planar fit shift coefficients, b_0 [ms^{-}1], for each sonic anemometer and wind direction sector specified by degrees from North.

Sector	z_1= 0.45 m	z_2= 1.27 m	z_3= 2.15 m	z_4= 3.79 m	z_5= 6.32 m
$80 < \phi \leq 120$	0.009	-0.006	-0.014	-0.020	-0.036
$40 < \phi \leq 80$	-0.014	0.016	0.018	0.022	0.000
$0 < \phi \leq 40$	-0.026	-0.005	-0.007	0.008	-0.007
$320 < \phi \leq 360$	-0.021	-0.018	-0.021	-0.023	-0.033
$280 < \phi \leq 320$	-0.029	-0.012	-0.019	-0.011	-0.026
$240 < \phi \leq 280$	-0.036	0.007	-0.019	-0.001	-0.022

A.1.3 Summary of Field Data

Table A.4 includes information regarding the measurements from nine clear-sky nights in September of 2011 when downslope flow was observed, and that were used in conjunction with the model as described in the main article text. It summarizes the measurements by showing nightly means of relevant velocity and temperature quantities. Therein, N_{SEG} is the number of 5-minute segments comprising the data set for each night, U is the mean velocity, $\Delta\theta_{max}$ is the maximum virtual temperature deficit, σ_{WD} is the standard deviation in wind direction, and the numbered subscripts correspond to the respective sensor heights as defined in the article text (z_1 = 0.45 m, z_2 = 1.27 m, z_3 = 2.15 m, z_4 = 3.79 m and z_5 = 6.32 m). Generally, the maximum measured mean velocity in the katabatic jet layer was at z_2 = 1.27 m. Note this measurement location is slightly above the estimated height of the jet peak, and should not be interpreted as the actual jet peak velocity. However, the nightly means of the dimensionless quantity $(U_2 - U_5)/U_5$ show that the flow exhibits no consistent jet shape in the $U(z)$ profile during the nights of Sept. 24, 29 and 30, which indicates a significant larger scale disturbance preventing a katabatic jet formation.

Thermocouples used to measure the mean air temperatures that drive the model thermal forcing were mounted at slope-normal heights of 0.53, 0.94, 1.27, 2.15, 3.79 and 6.32 m. The top four sensors were collocated with the sonic anemometer measurement paths, while the others were mounted on a near-surface array at the tower site. These temperatures were converted to virtual potential temperatures using a linear fit of humidity data (Vaisala, HMP45C) taken at two heights (2.1 and 5.3 m, slope-normal) and the mean air pressure measured inside the logger box at the site.

A.1.4 Comment Regarding the Subsidence Assumption

For the model assumption that $W = 0$ to hold locally, the katabatic jet should not accelerate (i.e. $\partial U/\partial x = 0$, or advection terms are negligible) as it moves down the slope. Otherwise, the jet would entrain ambient at air and $W \neq 0$. Since the field measurements were made from a single tower, verification that $\partial U/\partial x = 0$ cannot be determined directly from the measurements. However, by rotating the coordinate system into the mean wind, $\partial V/\partial y = 0$

Table A.4 – Summary of field data used in conjunction with the 1D model.

Day of Month	N_{SEG}	U_5 (ms^{-1})	U_2/U_5	$(U_2-U_5)/U_5$	$\Delta\theta_{max}$ (K)	σ_{WD,z_5}	σ_{WD,z_1}
14	84	1.0	1.6	0.6	1.8	49.3°	17.4°
15	60	0.7	2.3	1.3	2.2	59.8°	16.3°
16	84	1.3	1.7	0.6	2.8	50.2°	14.6°
21	84	0.6	2.3	1.3	2.0	54.0°	15.7°
23	84	0.7	2.2	1.2	1.9	52.7°	10.1°
24	60	1.5	0.9	-0.8	1.0	90.1°	56.0°
28	84	1.8	1.4	0.4	1.9	48.6°	18.4°
29	48	2.1	0.8	-0.2	0.9	69.8°	53.9°
30	72	2.9	0.8	-0.2	1.4	37.1°	22.0°

is imposed, and therefore by continuity, $\partial U/\partial x = 0$ if $\partial W/\partial z = 0$. The tower measurements show that $\partial W/\partial z = 0$ for the vast majority of the averaged segments via a t-test. Specifically, the t-test shows that for only 7% of all measurement segments the can the null hypothesis be rejected. In other words, statistically significant deviations from $\partial W/\partial z = 0$ occur in only 7% of the cases. Hence to first order, there is a high level of confidence that no significant downslope acceleration occurs locally, and that the assumption $W = 0$ holds.

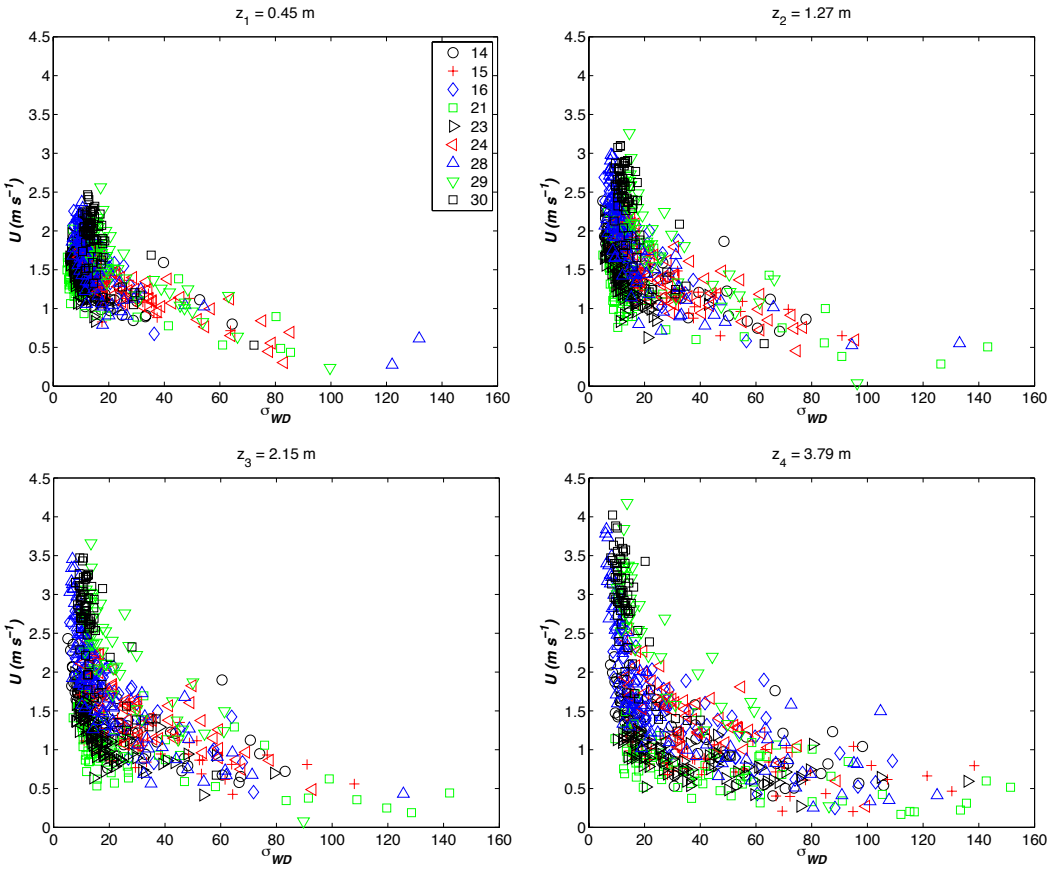

Figure A.1 – Measured U vs σ_{WD} for the lowest four measurement locations. As in the main document, the symbols correspond to the day in September. The trend of increasing σ_{WD} for decreasing U can be seen in all measurement locations. This implies that the flow is not decoupling over the katabatic layer, and that larger-scale perturbations can penetrate to the surface.

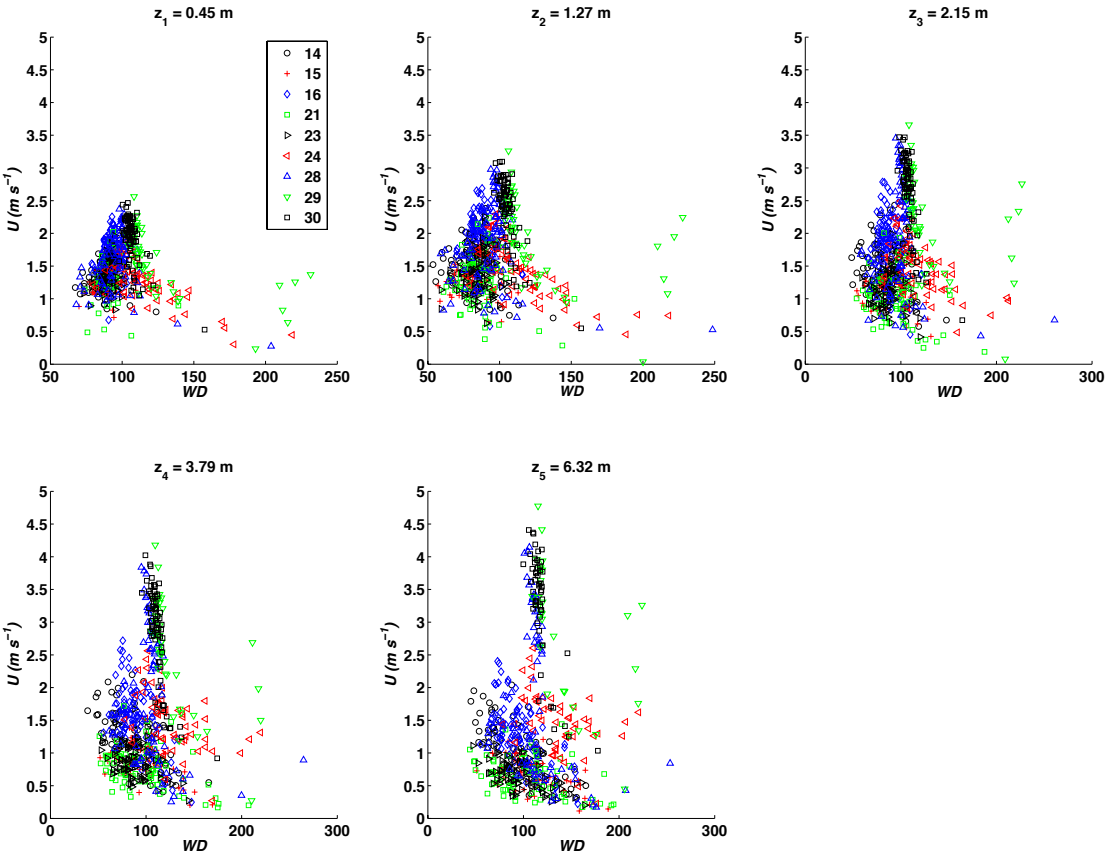

Figure A.2 – Mean velocity, U, vs absolute wind direction, WD [degrees from North], for each measurement location. Again, lower wind speeds are associated with oscillations around the main downslope direction, which is typically associated with higher wind speeds.

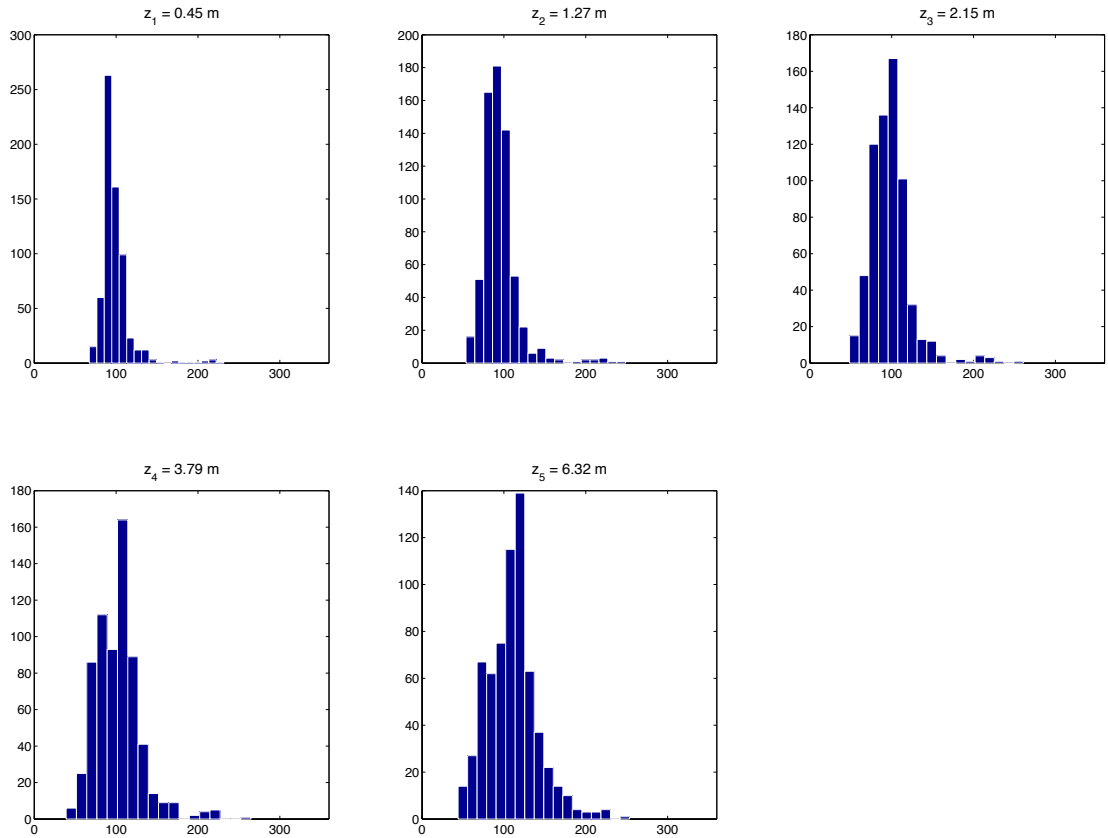

Figure A.3 – Histograms of wind direction [degrees from North] for each of the five measurement location for the nine nights of field experiment data used in the main analysis. The Gaussian distributions become more broad with height as the sensor footprint increases.

A.2 Thermal diffusivity of seasonal snow determined from temperature profiles

This appendix has been published with the following citation:

Oldroyd H J, Higgins C W, Huwald H, Selker J S, and Parlange M B. Thermal diffusivity of seasonal snow determined from temperature profiles. *Advances in Water Resources*, 55:121–130, May 2012.

Abstract: *Thermal diffusivity of snow is an important thermodynamic property associated with key hydrological phenomena such as snow melt and heat and water vapor exchange with the atmosphere. Direct determination of snow thermal diffusivity requires coupled point measurements of thermal conductivity and density, which continually change due to snow metamorphism. Traditional methods for determining these two quantities are generally limited by temporal resolution. In this study we present a method to determine the thermal diffusivity of snow with high temporal resolution using snow temperature profile measurements. High resolution (between 2.5 and 10 cm at 1 minute) temperature measurements from the seasonal snow pack at the Plaine-Morte glacier in Switzerland are used as initial conditions and Neumann (heat flux) boundary conditions to numerically solve the one-dimensional heat equation and iteratively optimize for thermal diffusivity. The implementation of Neumann boundary conditions and a t-test, ensuring statistical significance between solutions of varied thermal diffusivity, are important to help constrain thermal diffusivity such that spurious high and low values as seen with Dirichlet (temperature) boundary conditions are reduced. The results show that time resolved thermal diffusivity can be determined from temperature measurements of seasonal snow and support density-based empirical parameterizations for thermal conductivity.*

Keywords: Heat diffusion, Porous media, Snow temperature measurements, Thermal conductivity, Thermal diffusivity

A.2.1 Introduction

Snow thermal diffusivity is an important thermodynamic property in snow hydrology because it regulates heat diffusion in the snow as defined by the heat equation [Carlslaw and Jaeger, 1959]. Hence, it is an important parameter for understanding heat transfer and predicting snowmelt [Kondo and Yamazaki, 1990], and is therefore applicable to water resources management activities such as agriculture, hydropower and municipal water usages [DeWalle and Rango, 2008]. Furthermore, thermal diffusivity can be useful in improved prediction of snowmelt timing and streamflow discharge because typical snowmelt models are tuned to air temperature, and therefore, lack a full physical basis [Simoni et al., 2011]. Heat transfer

in snow occurs by conduction through the ice matrix, by conduction through air-filled pore spaces, by latent heat exchanges of water vapor (condensation and sublimation) [DeWalle and Rango, 2008] and by radiative heating [Brandt and Warren, 1993, DeWalle and Rango, 2008, Aoki et al., 2011]. In addition, convection [Sturm and Johnson, 1991, Zhekamukhov and Shukhova, 1999, Zhekamukhov and Zhekamukhova, 2002], and wind pumping [Colbeck, 1989, Clarke et al., 1987] can also play a role. However, these mechanisms are less well understood. Better temporal resolution in heat transfer studies may allow for improved understanding of these mechanisms because they occur at relatively short time scales.

Snow is a porous medium whose physical properties evolve in time, and therefore can be difficult to characterize. It continuously undergoes morphological changes in grain size and shape, density, and bonding due to metamorphism, all of which affect the snow thermal properties [DeWalle and Rango, 2008]. Thermal conductivity of snow is also anisotropic, having different values in horizontal and vertical directions [Calonne et al., 2011]. A better understanding of heat transfer processes in snow and their natural impacts requires a better understanding of how thermophysical properties vary in time [Arons and Colbeck, 1995]. Due to the labor intensity of some measurement techniques, such as the excavation of snow pits, the potential temporal and spatial resolution of snow property measurements is limited. Furthermore, some measurement techniques might actually alter the snow properties being measured by disrupting its structure [Riche and Schneebeli, 2010].

Direct determination of thermal diffusivity requires measurements (either in-situ or in extracted samples) of two quantities: thermal conductivity and snow density. Generally, density measurements require snow pit excavation and gravimetric analysis of individual samples from varying depths. Therefore, snow density measurements with high temporal resolution are difficult to obtain. For thermal conductivity, several techniques exist which vary greatly in cost, ease of implementation, accuracy and spatial and temporal resolution. Some of these methods are described in Section A.2.2, and a more rigorous summary and critique of several of the techniques was presented by Sturm et al. [1997]. Many of these methods require specialized, relatively expensive equipment in addition to requiring substantial effort to obtain measurements at high spatial and temporal resolution.

An alternative approach is to measure snow temperatures and invert the heat equation to obtain the thermal conductivity or thermal diffusivity of snow. The major advantages of this approach are that temperature is relatively inexpensive to measure and can provide many more options for spatial and temporal resolution. As an example of the inversion approach, Brandt and Warren [1997] successfully used a one-dimensional vertical finite difference scheme with Dirichlet boundary conditions (specifying temperature in time) and a stationary density profile to optimize for thermal conductivity of snow at the South Pole. However, the Brandt and Warren [1997] study is not representative of ephemeral, seasonal snow packs of hydrological importance because the diurnal solar forcing was atypical (polar night for 6 months) and snow temperatures were extremely low ($< -40°C$). In relatively warm snowpacks latent heat transfer can account for a significant portion of the overall heat transfer [Sturm et al., 1997]. Due to

these complications, it was unclear that the method used by Brandt and Warren [1997] could be successful for relatively warm snowpacks with the strong diurnal forcing experienced by seasonal snow.

For the present study the inversion approach of Brandt and Warren [1997] was extended to determine thermal diffusivity for seasonal snow with the addition of two key steps. First, Neumann boundary conditions (specifying heat flux in time, as determined by the temperature measurements) must be used for the simulation so the predicted temperatures are not artificially constrained, and second, a statistical test is integrated into the analysis to determine when there is sufficient information within the temperature profiles to converge to a unique solution. In this paper this new approach was used to find the thermal diffusivity for seasonal snow on the Plaine-Morte glacier, an important water reservoir in the Bernese Alps of Switzerland. High resolution (between 2.5 and 10 cm at 1 minute) temperature measurements were used as initial and boundary conditions to numerically solve the one-dimensional heat equation, and iteratively optimize for thermal diffusivity. The temperature measurement probe used in this study is relatively inexpensive, easy to install and allows for monitoring throughout a season. Section 2 of this paper discusses and compares some of the existing techniques to obtain the thermal diffusivity of snow. In Section 3, the experiment site and temperature measurement techniques are described. The proposed method to determine time-resolved thermal diffusivity of seasonal snow is presented in Section 4. Finally, the results and error analyses are presented and discussed along with recommendations for subsequent uses of the new measurement probe and methods for determining thermal diffusivity.

A.2.2 Thermal Diffusivity and Measurement Techniques

Thermal diffusivity is a combination of the thermal properties of a medium which govern the heat diffusion rate through that medium according to the heat equation

$$\frac{\partial T}{\partial t} = \alpha \frac{\partial^2 T}{\partial z^2}, \tag{A.1}$$

where α is the thermal diffusivity, T is temperature, z is distance (in our case vertical depth) and t is time [Carlslaw and Jaeger, 1959]. The thermal diffusivity is defined as

$$\alpha = \frac{\kappa}{\rho C_p}, \tag{A.2}$$

where κ is the thermal conductivity, ρ is the density and C_p is the specific heat capacity. Since snow is a porous media comprised of ice matrices and air-filled pores, its thermal properties are generally described as being *effective* values at averaged macro scales [Arons and Colbeck, 1998, DeWalle and Rango, 2008]. Throughout this paper thermal properties are to be considered their effective values in the vertical component, considering snow's anisotropy. Heat conduction through the solid ice matrix is the dominant heat transfer mechanism because the thermal conductivity of ice is approximately two orders of magnitude greater than

that of air [DeWalle and Rango, 2008]. Accordingly, snow microstructure, grain size, shape and intergranular bonding, strongly influence the thermal conductivity [Arons and Colbeck, 1995]. In addition, latent heat transfer can also play a significant role in relatively warm snow [DeWalle and Rango, 2008]. However, latent heat transfer is also a diffusive mechanism which occurs along a temperature gradient, so its effects can be naturally lumped into an effective thermal diffusivity [Morris, 1983, Sturm et al., 1997, Arons and Colbeck, 1998, DeWalle and Rango, 2008].

Several techniques exist for measuring thermal conductivity. One such method is to use a heated plate to study the steady-state heat flow across an extracted block of snow [Pitman and Zuckerman, 1968]. Once at equilibrium, the temperature gradient across the sample block is used to calculate the thermal conductivity. Since the snow sample is heated from one end, care must be taken to insulate the edges such that the heat transfer occurs only across the sample [Pitman and Zuckerman, 1968, Sturm et al., 1997]. In addition, the imposed temperature gradient may cause the snow sample to undergo metamorphism [Sturm et al., 1997]. Another highly technical approach for determining thermal conductivity is based on microstructure tomography (e.g. Kaempfer et al. [2005] and Calonne et al. [2011]). This methodology uses tomographic 3D images of snow microstructure and the steady-state heat transport equation to determine the effective thermal conductivity by separating the heat transfer over the ice matrix and pore spaces for a volumetric snow sample [Calonne et al., 2011]). Beyond the specialized equipment necessary for these types of analyses, the methods are relatively labor intensive and require careful extraction and storage of snow samples. Hence, obtaining measurements with high spatial and temporal resolution with this approach is impractical.

Another approach for measuring thermal conductivity uses the transient heat transfer resulting from an unsteady heat input (and often the subsequent cooling) [Blackwell, 1954, Lange, 1985]. Sturm et al. [1997] describe some of the various instrument configurations that have been used with the transient heat transfer approach, and mention that needle probe or point heat source configurations are ideal because they are less likely to disturb the snow. Generally, the needle probe consists of a thin needle of which one end is heated and the other end monitors the temperature change between the two sections. In concept, the analytical solution for heat diffusion in an infinite wire predicts that the temperature change over the needle is linearly related to the natural log of time, and the thermal conductivity is proportional to the slope of this line [Morin et al., 2010]. These heat probes have been used in cold chambers [Jaafar and Picot, 1970, Sturm and Johnson, 1992], inserted into walls of snow pits [Jaafar and Picot, 1970, Lange, 1985, Sturm et al., 1997], and naturally covered by snow fall [Morin et al., 2010]. The transient heat probe method for determining thermal conductivity provides more flexibility in terms of spatial and temporal resolution than the steady-state method. The needle probes, though small, may still significantly alter the snow structure [Riche and Schneebeli, 2010], and Calonne et al. [2011] show that thermal conductivities determined by the needle probe methods are systematically lower than those determined by other methods.

Empirical parameterizations, which relate the thermal conductivity to the snow density, have also been proposed. Sturm et al. [1997] presented a parameterization based on a comprehensive compilation of snow density and thermal conductivity measurements from several techniques and studies. Other empirical, density-based parameterizations have also been proposed by Calonne et al. [2011] (determined from tomographical, heated plate, and the needle probe techniques), Aggarwal et al. [2009] (determined by the needle probe technique), and Yen [1981] (determined from a compilation of unnumbered investigations). All of these parameterizations have a wide range of scatter, usually attributed to the differences in snow microstructure and bonding that can occur for a given snow density. Furthermore, these parameterizations require knowledge of the snow densities which, as mentioned previously, are dynamic and difficult to monitor with high temporal resolution. Often these types of parameterizations are used in various heat and mass transfer models for snow. Some examples are a catchment-scale snowmelt model [Kondo and Yamazaki, 1990], a glacier mass balance model [Rye et al., 2010], a climatological atmospheric warming study using englacial temperatures [Gilbert et al., 2010], in a near-surface model to be used by backcountry avalanche forecasters [Bakermans and Jamieson, 2009], and for comparison with a micro-structure based snow cover model [Fierz and Lehning, 2001].

Other methods that use snow temperature profiles to determine thermal diffusivity include spectral or analytical techniques. The spectral method tracks the amplitude ratio and phase shift of the diurnal temperature signal as it propagates into the snowpack [Weller and Schwerdtfeger, 1971]. This method is ideally applied over several diurnal cycles in a stationary medium and hence, is not well suited to snow because it cannot account for the transient features of the snowpack. Another inversion approach might be to use the existing analytical solutions to the initial boundary value problem that can be found in chapter 3 of Carlslaw and Jaeger [1959]. This was the initial approach used in the present study, but it was found that the analytical solution (not shown herein) was more computationally expensive to evaluate and numerically unstable (Gibb's ringing near the boundaries) than numerical solutions to the heat equation.

The method proposed here to determine thermal diffusivity of seasonal snow with high temporal resolution is a numerical inversion of the heat equation. As mentioned previously, Brandt and Warren [1997] successfully used a one-dimensional vertical finite difference scheme with Dirichlet boundary conditions to optimize for effective thermal conductivity from temperature measurements obtained at the South Pole. They used a density profile determined from a linear fit of densities measured in two snow pits separated in time by nearly one year (January 1992 and December 1992). Brandt and Warren [1997] calculate thermal conductivity on 15 minutes intervals, and report 9-day averages with error bars representing conductivities with $\pm$ 10% relative error.

Although Brandt and Warren [1997] have shown that on average, this type of method can successfully determine thermal conductivity for relatively cold snowpacks with little diurnal forcing, it is unclear that the method would be successful for typical seasonal snow packs.

Reusser and Zehe [2010] used the same method as Brandt and Warren [1997], and applied it to temperature measurements of seasonal snow in the eastern Ore Mountains near the Czech-German boarder. They used a constant snow density and assumed thermal diffusivity to be constant over periods of 1 day or 5 days. In this case, although the snow itself and the environmental conditions were seasonal, the application of the method was not representative of the morphological variations associated with seasonal snow. Furthermore, Reusser and Zehe [2010] present only one result for thermal diffusivity, $\alpha = 5\times10^{-7}$ m^{2}s^{-1} and reported that 71% of the computed thermal diffusivity values were above an upper limit of $\alpha = 1\times10^{-6}$ m^{2}s^{-1}, the approximate thermal diffusivity of ice. Zhang and Osterkamp [1995] presented a method which addresses this seemingly common artifact of spuriously high thermal diffusivities resulting from inversion methods. They proposed a finite difference method that retains higher order terms and thus requires at least five vertically aligned temperature measurements. Using this method as well as the standard finite difference method (neglecting higher order terms) both with Dirichlet boundary conditions, they determined thermal diffusivity from synthetic temperature profiles for permafrost and the soil active layer. Their comparison of these two methods showed that retaining higher order terms eliminated the spurious values that arose from the standard finite difference method. However, they also concluded that if higher order terms are retained, the temperature measurements used in the inversion must be much more accurate (as high as two orders of magnitude more depending on the spatial and temporal discretization [Zhang and Osterkamp, 1995]). Hence, this method may be impractical for use with field measurements. The present study proposes a similar heat equation inversion method for determining the thermal diffusivity of seasonal snow. However, we propose a method that naturally constrains the model such the spurious values of unrealistically high thermal diffusivity (as seen by Reusser and Zehe [2010]) are reduced through the use of Neumann (heat flux) boundary conditions.

A.2.3 Experimental Set-up

A field experiment was performed at the Plaine-Morte glacier, located in the Bernese Alps of Switzerland (46.3863° N, 7.5178° E, 2750 m elevation) from 29 January to 4 March 2008. The glacier is approximately 2 km wide, 5 km long and essentially flat, providing a relatively horizontally homogeneous snow field and atmospheric fetch.

To obtain vertical profiles of temperature within the seasonal snow on the glacier, a 2 m long, white (to reduce radiative effects) Polyamide 6 (PA6) pole was equipped with type-T ($\pm1°C$) thermocouples at 25 mm spacing prior to deployment. Thin circular grooves were machined into the pole so that when mounted, the thermocouples were flush with the surface of the pole (see the detail photo in Figure A.4). The measurement junction of each thermocouple is more than 10 cm from the point at which the wire emerges from the sensor core to assure accurate representation of the snow temperature. This pole will be referred to as the TCT probe for the remainder of the paper. The TCT probe was connected to a data logger (Campbell Scientific CR10X) by means of a 25 channel, solid-state multiplexer (Campbell Scientific AM25T). Since

the number of thermocouples sampled was limited by the number of multiplexer channels, sampled thermocouple spacing varied between 40 cm and 2.5 cm, and selection was made with the intent of having higher resolution temperature measurements near the snow surface throughout the season (maximum spacing for those used in the analysis was 5 cm). The positive horizontal grid lines in Figures A.4 and A.5 show the locations of the sampled thermocouples. Initially, the TCT probe was inserted vertically with the bottom 1 m in the snow, leaving 1 m above to measure subsequent snow accumulation. To maximize contact between the TCT probe and the snow, the TCT probe was firmly inserted with one smooth motion. Thermocouple temperatures were sampled every 1 minute.

In addition, a meteorological measurement station was erected at the site. Among the instruments sampled each 1 min were air temperature and relative humidity (Rotronic MP100A), snow height (Campbell Scientific SR50, acoustic range finder) and snow surface temperature (Apogee Instruments IRTS-P, infrared thermocouple sensor). On six occasions during the experiment, snow pits were dug and density profiles were measured by weighing samples of a known volume (100 cm^3) with a standard SLF-Davos snow density kit. The vertical extent of the snow volume sampler is 3 cm and the snow density was sampled every 5 cm in depth. Figure A.5 shows the density evolution for the upper snowpack as well as snow height relative to the TCT probe. For all analyses we imposed a coordinate system defined by the TCT probe position. Hence, the matter below the vertical zero is the lower portion of the snowpack that the TCT probe does not reach, but where density measurements were made during the first snow pit excavation.

The acoustic range finder was located a few meters from the TCT probe and hence, could have reported slightly different snow height than what existed at the TCT probe location. Therefore, the snow height was also determined by inspection of the snow temperature profiles in a manner similar to the methods of Reusser and Zehe [2010]. Figure A.4 presents an example of a 24-hour period of snow temperature profiles. Profiles are used to determine the level of the snow surface by visual inspections over a 12 or 24-hour cycle for periods of no or minor precipitation. Snow has an insulating effect such that the temperature signals in the snow lag the thermal forcing at the surface and temperatures in the air are much more rapidly mixed. The surface is located near the sensor point where the ensemble of profiles over the considered period shows the most pronounced changes in gradient (kinks). Since this study required an approximate estimate of snow height (we only use thermocouples at least 10 cm below the snow surface), this snow height estimation method was sufficient.

A.2.4 Methodology

This study used the measured temperature profiles to determine thermal diffusivity of snow by inverting the heat equation (Equation A.1). More specifically, the heat equation was numerically solved in time and space given measured initial and boundary conditions for a range of thermal diffusivities. This was done iteratively, narrowing the range of effective

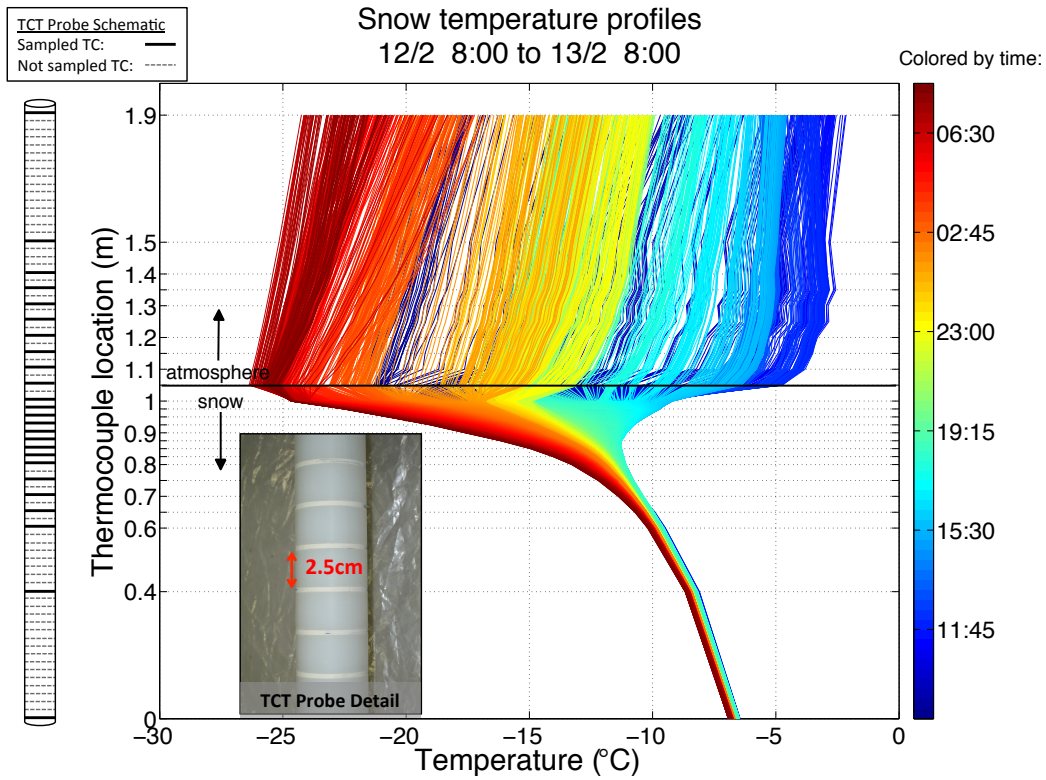

Figure A.4 – An example of a 24-hour period of snow temperature measurements for the 12th and 13th of February 2008. The horizontal grid lines indicate the relative locations of the sampled thermocouples, which are also indicated in the TCT probe schematic. The inset figure shows a detail photo of the TCT probe.

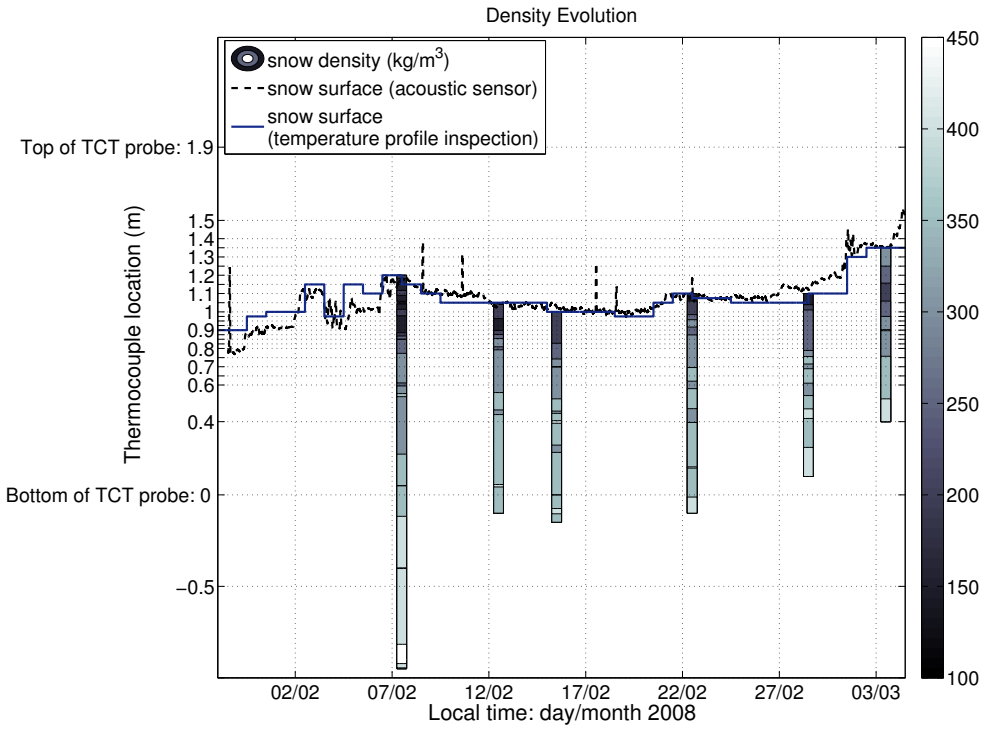

Figure A.5 – Density evolution and snow height throughout the experiment. Gravimetric density was measured every 5 cm in depth. Since the snow depth changes over the season, a convenient coordinate system is that of the TCT probe with z=0m at bottom of the probe. The horizontal grid lines indicate the relative locations of the thermocouples which were sampled throughout the experiment, with the exception of z = -0.5 m that was included for spatial referencing of the first snow pit.

thermal diffusivities until the RMS error between the measured and predicted temperatures was minimized. A flow chart describing the optimization routine is presented in Figure A.6.

The spatial domain, or specific thermocouple locations used for the modeled temperature predictions, was chosen with some competing considerations. This method determines a *bulk* thermal diffusivity over the domain simulated and so in principle, the extent of the domain should be minimized. However, having a larger number of temperature measurements in the domain allows for a better description of the physics (especially where large gradients and high degrees of curvature exist), and it provides more test points for comparing the respective RMS errors when optimizing for thermal diffusivity. The results presented herein were determined for a domain of seven internal measurement points between the top and bottom boundaries of the domain. On average the internal domain size was 25 cm and the changes in snow density over this depth range were small. The top boundary was chosen such that it is at least 10 cm below the snow surface to avoid regions where solar radiation may introduce non-linear effects to the heat transfer [Brandt and Warren, 1993, Aoki et al., 2011].

The temporal domain used to simulate temperatures was 30 minutes. Hence for each time step (every one minute) where thermal diffusivity is assigned, the RMS error is computed from the difference between the measured and predicted temperatures from 15 minutes into the past and future. Although the results are obtained for each one-minute time step, the temporal resolution of the results is 30 minutes. Increasing the temporal domain naturally reduces the variation in the results; of course it also reduces the temporal resolution. In short, we solve for the bulk thermal diffusivity in the layer defined by the spatial domain as a function of time.

To test the robustness of the method, the search range for thermal diffusivity on the first iteration was wide and coarse, testing 30 values between 1×10^{-9} m^{2}s^{-1} and 1×10^{-1} m^{2}s^{-1}. For each subsequent iteration, the search range was narrowed to test 20 values between 2 points on both sides of the value of thermal diffusivity with the lowest RMS error from the previous iteration. Iterations continued until the RMS error was changed by no more than 1×10^{-4} and the value of effective thermal diffusivity that best represents the physical processes described by the heat equation was subsequently assigned. Figure A.6(c) contains an example of the final iteration for a single time step showing a clear, sharp RMS minimum associated with a particular thermal diffusivity.

The numerical predictions of temperature, or modeled temperatures, were determined by using MATLAB's partial differential equation (PDE) solver, *pdepe*, to solve the heat equation. This function solves a system of ordinary differential equations (ODEs), integrated in time, that result from the spatial discretization of the original PDE [pde, 2011]. The initial condition was the first measured temperature profile in each 30-minute time segment, linearly interpolated to a profile with twice the original resolution (from 7 original measurement points to 14 points in the profile). Prior to calculation of the RMS error, simulated temperatures were interpolated back to the original spatial resolution of the measurements.

Neumann (heat flux) boundary conditions were used at the top and bottom of the domain.

The Fourier heat fluxes at the boundaries were determined using finite differences of the temperature nodes on the internal boundaries and the adjacent external temperature nodes to calculate the respective temperature gradients, as shown in Figure A.7. All temperatures used are temperatures within the snowpack, not air or surface temperatures. Neumann boundary conditions are critical to this method because they increase the model's sensitivity to thermal diffusivity, constraining it such that spurious spikes of unrealistically high thermal diffusivity are reduced. This is achieved naturally since the simulated temperature profiles are not artificially constrained at the endpoints as is in the case of Dirichlet type boundary conditions. Since the solution is unconstrained, the trivial, steady state solution of the heat equation is excluded and consequently, the spuriously high values of diffusivity reported in other studies are avoided. The use of Neumann boundary conditions requires at least three measurements in the temperature profiles.

A further constraint on the model was applied for each time step by implementing a t-test on the initial search range for effective thermal diffusivity (the first optimization iteration). The t-test ensures that the RMS error associated with the minimum is statistically different from at least three of the four surrounding points (for example, when plotting RMS error versus thermal diffusivity). This step tends to eliminate spurious points of unrealistically low diffusivity by eliminating scenarios when optimization is attempted over a "flat" searching range, where no statistically clear minimum exists. Figure A.6(b) contains an example of a time step when the t-test indicated statistical insignificance, and thermal diffusivity was indeterminate.

A.2.5 Results and Discussion

Time-resolved thermal diffusivities of seasonal snow determined from methods described in Section A.2.4 are presented in Figure A.8 along with a line indicating the overall median value (α =2.5×10^{-7} m^{2}s^{-1}) of thermal diffusivity. The overall mean value of thermal diffusivity (α =3.9×10^{-7} m^{2}s^{-1}) is slightly higher. The results are shown with the density-based, empirical parameterizations for thermal conductivity [$W\ m^{-1}\ K^{-1}$] of Sturm et al. [1997],

$$\begin{aligned} \kappa_{\mathrm{eff_{Stu}}} &= 0.138 - 1.01\rho + 3.233\rho^2 \quad \{0.156\,g\,cm^{-3} \le \rho \le 0.6\,g\,cm^{-3}\} \\ \kappa_{\mathrm{eff_{Stu}}} &= 0.023 + 0.234\rho \qquad\qquad\qquad\qquad \{\rho < 0.156\,g\ cm^{-3}\}, \end{aligned} \tag{A.3}$$

Calonne et al. [2011],

$$\kappa_{\mathrm{eff_{Cal}}} = 2.5 \times 10^{-6}\rho^2 - 1.23 \times 10^{-4}\rho + 0.024 \quad \{\rho\ [kg\ m^{-3}]\}, \tag{A.4}$$

Aggarwal et al. [2009]

$$\kappa_{\mathrm{eff_{Agg}}} = 0.00395 + 0.00084\rho - 1.7756e{-}6\rho^2 + 3.80635e{-}9\rho^3 \quad \{\rho\ [kg\ m^{-3}]\}, \tag{A.5}$$

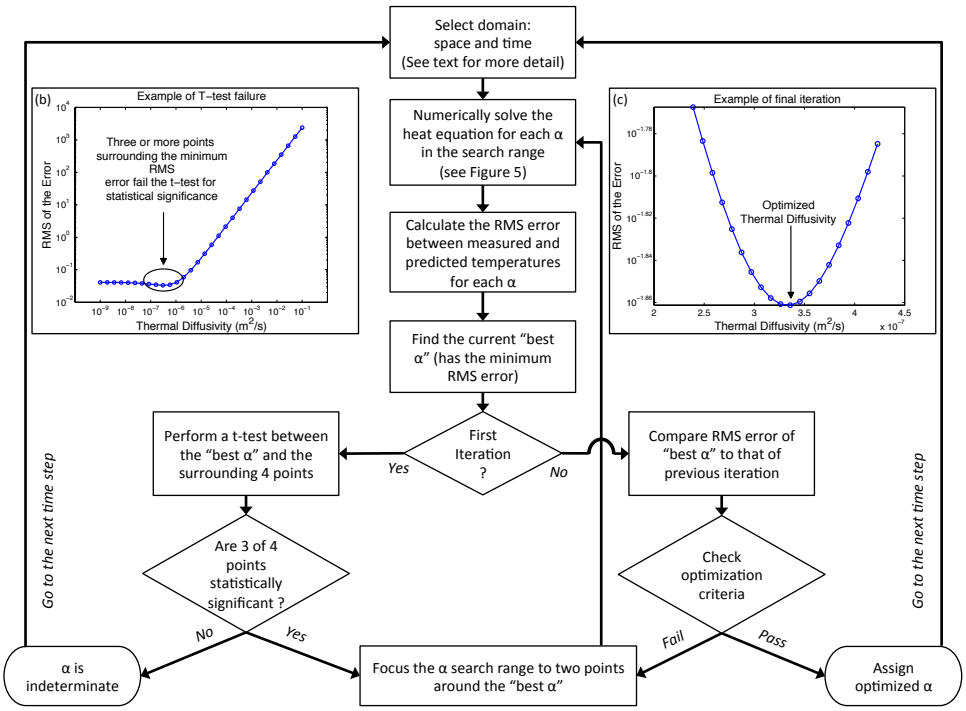

Figure A.6 – Flow chart of the method to determine thermal diffusivity, α, from temperature measurements. Inset figures include (b) an example of a time step when the optimization fails the t-test, and (c) a time step with successful optimization.

and Yen [1981]

$$\kappa_{\mathrm{eff}_{\mathrm{Yen}}} = 2.22362\rho^{1.885} \quad \{\rho\ [Mg\ m^{-3}]\}. \tag{A.6}$$

Note that the different units for Equations A.3 to A.6 are the units used in the original parameterizations in the respective publications. The densities that were measured during the six snow pit excavations and the specific heat of ice, $C_p = 2090$ J kg^{-1}K^{-1}, were used to calculate the parameterized thermal diffusivities according to the above equations for thermal conductivity. In addition, indicators of the approximate 95% confidence interval from the Sturm et al. [1997] density-based parameterization are also shown.

There is a high degree of variability in the thermal diffusivity time series. Despite the variability, the majority of the results are comparable to the density-based empirical parameterizations, and are within the bounds of the 95% confidence interval reported in the Sturm et al. [1997] parameterizations. Furthermore, only 3.8% of the thermal diffusivities are above $\alpha = 1\times10^{-6}$ m^{2}s^{-1}, the approximate thermal diffusivity of ice used as a theoretical upper limit by Reusser and Zehe [2010]. Recall Reusser and Zehe [2010] used a similar inversion technique, but with Dirichlet boundary conditions, and reported 71% of their thermal diffusivities above this limit. To quantify the improvement that imposing Neumann boundary conditions brought to the results, we also performed an inversion imposing Dirichlet boundary conditions. In the

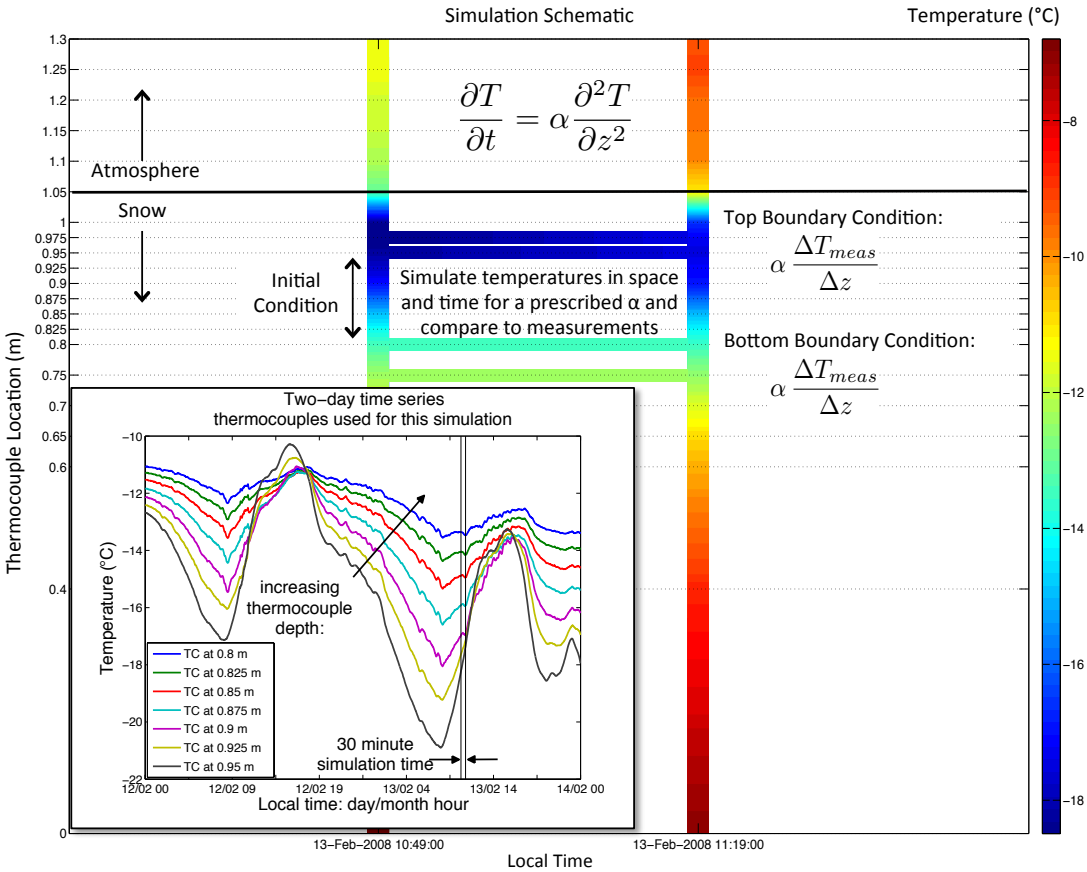

Figure A.7 – Schematic of the initial-boundary value problem used to predict temperature in space and time for the time step shown. It shows the 7 internal thermocouples used for the time step and the two thermocouples at each edge of the domain used to determine the Neumann (heat flux) boundary conditions. The inset figure shows a two-day time series of the 7 internal thermocouples used for this period.

Dirichlet case for the same temperature measurements, 17% were above $\alpha = 1\times10^{-6}$ m^{2}s^{-1}, and the diffusivity values were spread over a range of 10 orders of magnitude. Hence using Neumann boundary conditions provides a significant improvement to numerical inversion techniques for determining thermal diffusivity from temperature measurements with no extra computational expense.

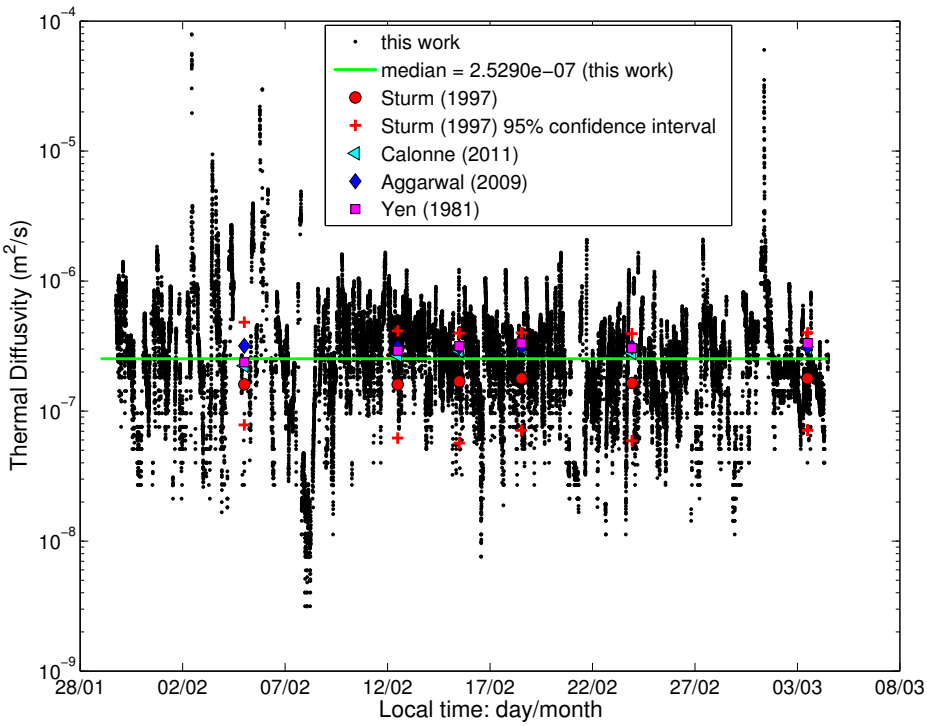

Figure A.8 – Time-resolved thermal diffusivity of seasonal snow. Results are compared to density-based empirical parameterizations described by Equations A.3 through A.6 along with marks indicating the 95% confidence interval from the Sturm et al. [1997] parameterization.

The extreme values of thermal diffusivity in Figure A.8 and the rapid rate of change toward these extremities are not likely representative physical changes in the thermal properties of the snow. To better understand this variability, additional analyses were undertaken for a segment of the temperature data between 22 and 28 February 2008. The first such analysis explores the influence of the spatial domain to determine if it was too large to be characterized by a single value of thermal diffusivity for each time step. To address question of domain size, we use the same methodology to determine thermal diffusivity, but in a tri-layered scheme by dividing the original domain into three smaller domains of three temperature measurements each: top, middle and bottom. Recall that the thermal diffusivities reported in Figure A.8 were determined using an internal domain of 7 consecutive thermocouples (starting from 10 cm below the surface and increasing in depth). Figure A.9 show how the thermal diffusivities from the tri-layered scheme compare to those determined over the larger

domain. The correlation plots (Figures A.9(b), (c) and (d)) show that the temperature signal in the top portion of the domain strongly influences the thermal diffusivity determined over the full domain because temperatures closer to the surface experience more change in time and exhibit higher gradients. All subdomains also show high degrees of variability and hence, the size of the spatial domain had little influence on the variations in the results. The tri-layer analysis also shows a trend of increasing thermal diffusivity with snow depth, which may be expected since thermal conductivity generally increases with snow density and density generally increases with snow depth.

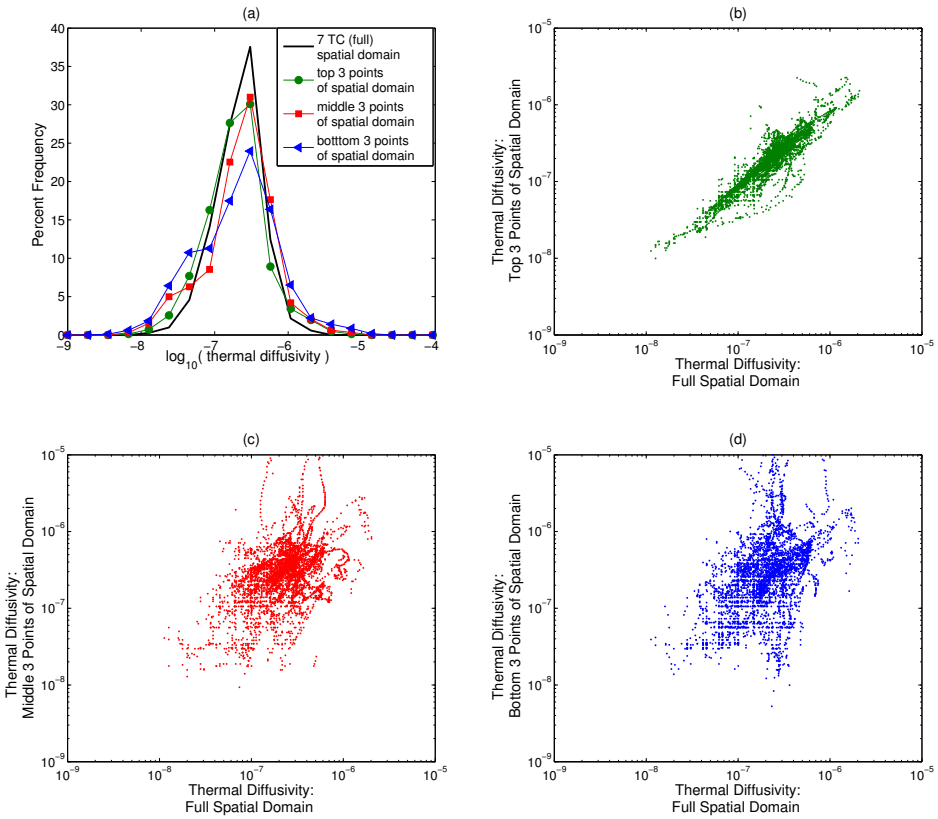

Figure A.9 – Results of the domain size analysis carried out for measurements from 22 to 28 February 2008. (a) Comparison of the PDFs for thermal diffusivity obtained using the full (7-point) spatial domain and three sublayers (3-point domains each) within the full domain. (b) Correlation of thermal diffusivity from the full domain and the top layer of the domain, (c) the middle layer of the domain and (d) the bottom layer of the domain.

The second analysis explores the possibility that uncertainty in the temperature measurements (type-T thermocouples: ± 1° C) contributes to the high variability of the determined thermal diffusivities. Since this method depends on the relative accuracy between temperature measurements (e.g. $\partial T/\partial t$ and $\partial^2 T/\partial z^2$ in the heat equation), it makes sense to assess

the effects of noise in the temperature measurements. This was done using the same method and domain used to obtain the results in Figure A.8, but by adding three different levels of Gaussian noise to the temperature measurements, indicated by the standard deviation of the noise, σ: σ = 0.25°C ($\Delta T_{error,max} \approx 1$°C), σ = 0.33°C and σ = 0.70°C. Figure A.10 shows that noise in the temperature signal has little change in the degree of variability of the results. However, this analysis shows that noise in the temperature signal tends to cause an increase in the resulting thermal diffusivity. This is likely due to the need for increased diffusion to smooth out the noise in the temperature signal.

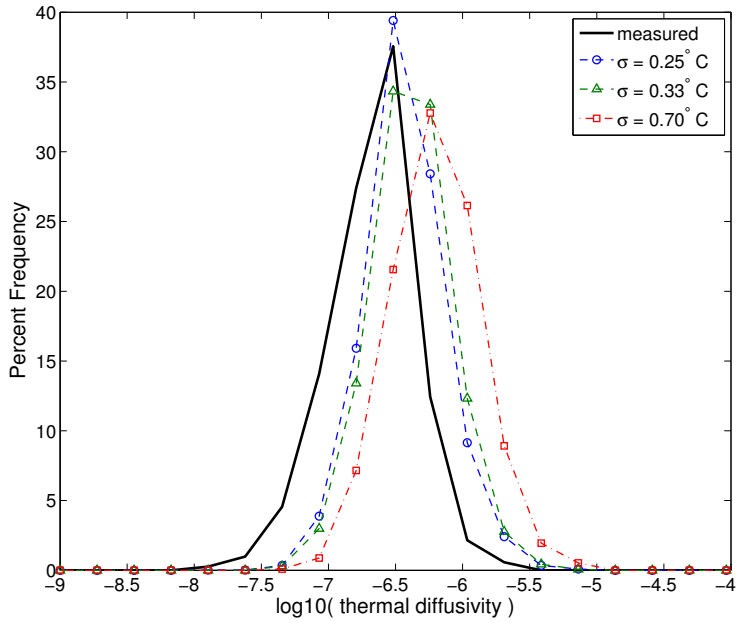

Figure A.10 – Comparison of thermal diffusivity obtained from the temperature measurements for 22 to 28 February 2008, and these temperature measurements with added Gaussian noise, where σ indicates the standard deviation of the added noise.

The third analysis explores the method's sensitivity to spatial discretization (or spatial resolution of temperature measurements) by using the same spatial domain size, but solving with half of the thermocouples used in the original results. Figure A.11 shows that decreasing the spatial discretization of the temperature measurements greatly increases the estimated thermal diffusivity, by almost two orders of magnitude in this case. Under-resolving the temperature profile leads to the underestimation of the curvature in the temperature profiles. Since the curvature is described mathematically by the $\partial^2 T/\partial z^2$ term in the heat equation (A.1), the thermal diffusivity must increase to balance the equation. Decreasing the spatial resolution also increases the chances of excluding the peak in the temperature profile (refer to Figure A.4). This analysis also shows that decreasing the spatial resolution also tends to slightly increase the range of variability of the results, but not to the degree to explain the

variability in Figure A.8.

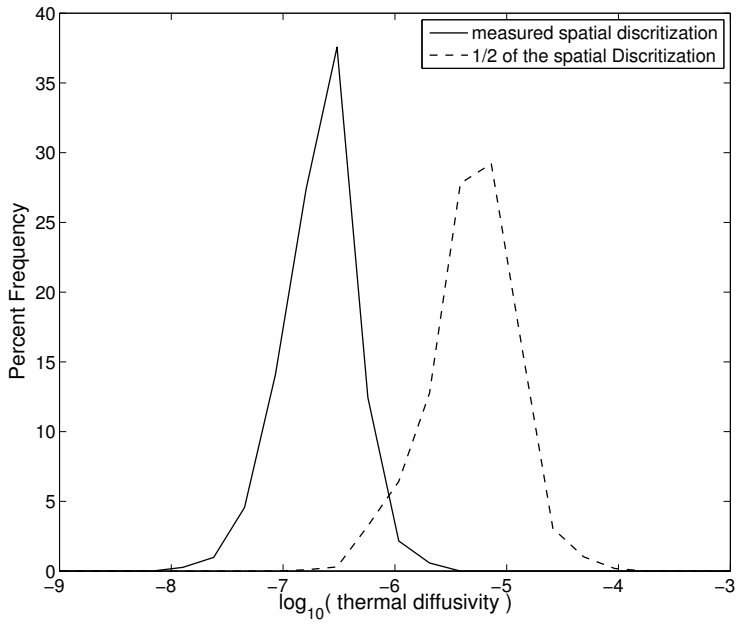

Figure A.11 – Comparison of thermal diffusivity obtained with the spatial discretization of temperature measurements from 22 to 28 February 2008, and those obtained using half the spatial discretization (temperature measurement resolution) in solving the PDE.

The final study explores the temporal domain used to generate the modeled temperatures. First, spectral analysis was performed on the time series of thermal diffusivity presented in Figure A.8. It showed timescales smaller than 30 minutes exhibit characteristics that are typically attributed to noise, thus larger time domains should tend to smooth variations. Sharp spectral filtering at the 30 minute time scale made almost no difference in the thermal diffusivity time series (data not shown). We also performed test cases of 2, 3, 6 and 12-hour temporal domains for which the variations in the resulting thermal diffusivities progressively decreased. However, the spikes and dips seen in Figure A.8 that approach $\sim 1\times10^{-6}$ and $\sim 1\times10^{-8}$ persisted. By reducing the small-scale temporal variability in these test cases, we were able to match the persistent extremes to times when the curvature in the temperature profiles switches concavity. Over a typical diurnal cycle, this occurs twice at the uppermost thermocouples, which show greater daily temperature change than those below it, switch from colder than those below to a warmer than those below, or visa versa (refer to Figure A.4 and inset of Figure A.7). This method appears incapable of solving for thermal diffusivities during these time periods, at least for temporal domains up to 12 hours.

Excluding the extreme values of thermal diffusivity produced when the temperature profiles switch concavity, the small scale temporal variations in thermal diffusivity could not be attributed (to the ability that the available information affords) to error in the temperature

measurements, discretization error or to bulk layer approximations. This level of variability on 30 minute time scales is not likely representative of time scales associated with changes of snow microstructure. The possibilities that this type of variability can be explained by non-diffusive forms of heat transfer such as wind pumping, convection, or radiation, remain open questions for future research. Since this method allows for high temporal resolution, it may prove useful in such studies, as well as studies regarding the expected temporal changes of thermal properties of snow.

A key outcome of these analyses is that the spatial resolution of the temperature measurements (or model discretization) has a greater effect on the resulting thermal diffusivities than noise in the temperature measurements. Hence, for future use of inversion-type techniques researchers should maximize the spatial resolution of the temperature measurements, as it will aid in adequately describing the curvature in the temperature profile and in capturing the peaks in the temperature profiles. In addition, high spatial resolution in the temperature measurements will provide more options for determining thermal diffusivity in various layers of the snowpack.

Use of this methodology to study the spatial variability of thermal diffusivity in large scale settings (for example, on the hydrologic catchment scale) is feasible. The proposed measurement technique, the TCT probe, was suitable, but not without flaws. For example, a snow temperature measurement technique which can guarantee no disruption to the surrounding snow, no additional heat conduction (through the poles or wires) and that the measurements remain at a fixed location, could potentially improve this type of technique, as well as other studies where snow temperatures are measured. However, since our results compare well to widely-used, density-based parameterizations we believe these factors had little effect on our results.

A.2.6 Conclusions

Thermal diffusivity is an important thermophysical property that governs the heat transfer in snow. We have proposed a technique to obtain thermal diffusivity with high spatial and temporal resolution. The method uses temperature measurements for the initial condition and Neumann (heat flux) boundary conditions, and numerically solves the heat equation to iteratively optimize for thermal diffusivity. We found that using Neumann boundary conditions reduces the seemingly common problem of spurious, unrealistically high values of thermal diffusivity that arise when Dirichlet boundary conditions are used. Since the Neumann boundary conditions impose a flux instead of a temperature (as in Dirichlet boundary conditions), the modeled temperatures are not artificially constrained at the boundaries. This provided a significant improvement over the results using Dirichlet boundary conditions, in which thermal diffusivities were spread over 10 orders of magnitude. In addition, the new method imposes a statistical t-test ensuring the measured temperature profiles contain enough information such that the optimal thermal diffusivity is unique. An added consequence of including the

t-test is that spuriously low values of thermal diffusivity are reduced.

The majority of the resulting thermal diffusivities compare well to published density-based empirical parameterizations. However, during time periods where the temperature profiles switch concavity this method behaves poorly and produces unreasonably high/low results. With the exception of these spikes/dips, variability at 30 minute time scales may indicate the presence of non-diffusive heat transfer processes such as wind pumping or convection. This method could assist in future studies of these phenomena. Using longer time intervals for the predicted temperatures naturally smooths out some of the variation in the results. However, heat transfer mechanisms and effects due to changes in the snow structure that occur on shorter time scales will be dampened out.

An important result of this study is that high spatial resolution in the temperature measurements (leading to denser discretization in the model) appears to be the most significant parameter in using this method (and most likely other inversion methods) to estimate thermal diffusivity. Lower spatial resolution will tend to result in an erroneously higher thermal diffusivity to compensate for the reduced curvature in the temperature profiles. In general, researchers should be aware of this sensitivity for future uses of inversion techniques.

Acknowledgements

We are grateful to the anonymous reviewers and the associate editor, Michael Lehning, for their thoughtful comments that substantially improved the manuscript. This research was supported with partial funding from the Swiss National Science Foundation [200021_120238/1, 200020_125092/1], the NCCR Mobile Information Communication Systems (MICS) project and Competence Center Environment and Sustainability (CCES) of ETH Domain. We are also grateful for logistical support from the Crans-Montana ski resort, and for the field assistance from the many members of the Environmental Fluid Mechanics and Hydrology (EFLUM) laboratory at EPFL.

Bibliography

10 2011. URL http://www.mathworks.com/help/techdoc/ref/pdepe.html.

RK Aggarwal, PS Negi, and PK Satyawali. New density-based thermal conductivity equation for snow. *Defence Sci. J.*, 59(2):126–130, 2009.

T Aoki, K Kuchiki, M Niwano, Y Kodama, M Hosaka, and T Tanaka. Physically based snow albedo model for calculating broadband albedos and the solar heating profile in snowpack for general circulation models. *J. Geophys. Res.*, 116(D11), 2011.

EM Arons and SC Colbeck. Geometry of heat and mass transfer in dry snow: A review of theory and experiment. *Rev. Geophys.*, 33(4):463–493, 1995.

EM Arons and SC Colbeck. Effective medium approximation for the conductivity of sensible heat in dry snow. *Int. J. Heat Mass Transfer*, 41(17):2653–2666, 1998.

L Bakermans and B Jamieson. SWarm: a simple regression model to estimate near-surface snowpack warming for back-country avalanche forecasting. *Cold Reg. Sci. Tech.*, 59(2-3):133 – 142, 2009.

JH Blackwell. A transient-flow method for determination of thermal constants of insulating materials in bulk part I – theory. *J. Appl. Phys.*, 25(2):137–144, 1954.

RE Brandt and SG Warren. Solar-heating rates and temperature profiles in Antarctic snow and ice. *J. Glaciol.*, 39(131):99–110, 1993.

RE Brandt and SG Warren. Temperature measurements and heat transfer in near-surface snow at the South Pole. *J. Glaciol.*, 43(144):339–351, 1997.

N Calonne, F Flin, S Morin, B Lesaffre, SR du Roscoat, and C Geindreau. Numerical and experimental investigations of the effective thermal conductivity of snow. *Geophys. Res. Lett*, 38(23):L23501, 2011.

HS Carlslaw and JC Jaeger. *Conduction of heat in solids*, volume 2. Oxford University Press, Oxford, UK, ed, 1959.

GKC Clarke, DA Fisher, and Waddington ED. Wind pumping: a potentially significant heat source in ice sheets. *IAHS–AISH Publication*, 170, 1987.

SC Colbeck. Air movement in snow due to windpumping. *J. Glaciol.*, 35(120):209–213, 1989.

DR DeWalle and A Rango. *Principles of snow hydrology.* Cambridge University Press, 2008.

C Fierz and M Lehning. Assessment of the microstructure-based snow-cover model snowpack: thermal and mechanical properties. *Cold Reg. Sci. Tech.*, 33(2-3):123–131, 2001.

A Gilbert, P Wagnon, C Vincent, P Ginot, and M Funk. Atmospheric warming at a high-elevation tropical site revealed by englacial temperatures at Illimani, Bolivia (6340 m above sea level, 16° S, 67° W). *J. Geophys. Res.*, 115(D10), 2010.

H Jaafar and JJC Picot. Thermal conductivity of snow by a transient state probe method. *Water Resour. Res.*, 6(1):333–335, 1970.

TU Kaempfer, M Schneebeli, and SA Sokratov. A microstructural approach to model heat transfer in snow. *Geophys. Res. Lett.*, 32:21, 2005.

J Kondo and T Yamazaki. A prediction model for snowmelt, snow surface temperature and freezing depth using a heat balance method. *J. Appl. Meteorol.*, 29(5):375–384, 1990.

MA Lange. Measurements of thermal parameters in antarctic snow and firn. *Ann. Glaciol.*, 6: 100–104, 1985.

S Morin, F Domine, L Arnaud, and G Picard. In-situ monitoring of the time evolution of the effective thermal conductivity of snow. *Cold Reg. Sci. Tech.*, 64:73–80, 2010.

EM Morris. Modelling the flow of mass and energy within a snowpack for hydrological forecasting. *Ann. Glaciol.*, 4:198–203, 1983.

D Pitman and B Zuckerman. Effective thermal conductivity of snow at -88°C,-27°C and-5°C. *SAO Special Report*, 267, 1968.

DE Reusser and E Zehe. Low-cost monitoring of snow height and thermal properties with inexpensive temperature sensors. *Hydrol. Process.*, 2010.

F Riche and M Schneebeli. Microstructural change around a needle probe to measure thermal conductivity of snow. *J. Glaciol.*, 56(199):871–876, 2010.

CJ Rye, NS Arnold, IC Willis, and J Kohler. Modeling the surface mass balance of a high arctic glacier using the ERA-40 reanalysis. *J. Geophys. Res.*, 115(F2):F02014, 2010.

S Simoni, S Padoan, DF Nadeau, M Diebold, A Porporato, G Barrenetxea, F Ingelrest, M Vetterli, and MB Parlange. Hydrologic response of an alpine watershed: Application of a meteorological wireless sensor network to understand streamflow generation. *Water Resour. Res.*, 47 (W10524):W10524, 2011.

M Sturm and JB Johnson. Natural convection in the subarctic snow cover. *J. Geophys. Res.*, 96 (B7):11657–11, 1991.

M Sturm and JB Johnson. Thermal conductivity measurements of depth hoar. *J. Geophys. Res.*, 97(B2):2129–2139, 1992.

M Sturm, J Holmgren, M König, and K Morris. The thermal conductivity of seasonal snow. *J. Glaciol.*, 43(143):26–41, 1997.

GE Weller and P Schwerdtfeger. New data on the thermal conductivity of natural snow. *J. Glaciol.*, 10:309–311, 1971.

YC Yen. Review of thermal properties of snow, ice and sea ice. Technical Report 81-10, CRRL, 1981.

T Zhang and TE Osterkamp. Considerations in determining thermal diffusivity from temperature time series using finite difference methods. *Cold Reg. Sci. Tech.*, 23(4):333–341, 1995.

MK Zhekamukhov and LZ Shukhova. Convective instability of air in snow. *J. Appl. Mech. Tech. Phys.*, 40(6):1042–1047, 1999.

MK Zhekamukhov and IM Zhekamukhova. On convective instability of air in the snow cover. *J. Eng. Phys. Thermophys.*, 75(4):849–858, 2002.

A.3 Additional Field Work

Apart from the 2011 summer slope flow experiment in Val Ferret that was used for the bulk of the analyses presented in this dissertation, several other field campaigns that were designed to investigate turbulent transport in various alpine environments were undertaken by myself and the EFLUM laboratory. These campaigns span a wide range of topics and included a variety of measurement techniques, as briefly described below. The principal funding bodies for these campaigns were the Swiss National Science Foundation (SNSF) and Competence Center Environment and Sustainability (CCES) of ETH Domain, and they could not have been completed without the amazing support of the EFLUM laboratory team members.

A.3.1 Alpine Metrology experiment; Summer 2011

This field campaign in Val Ferret, Switzerland (see Figure A.12) aimed to investigate interactions between turbulent surface exchanges and valley-scale flows, and was co-organized by Megan Daniels and Marc Calaf. The slope flow analyses presented in Chapters 2 to 4 were only a part of the larger objectives. Other primary objectives included investigating the full energy balance over sloping alpine terrain (Figure A.12B), and valley-scale circulations during intensive operating periods (IOPs) using a profiling tether-sonde and ballon (Figure A.12C) and along-slope and along-valley Doppler lidar scans (Figure A.12D).

A.3.2 Coherent Structures Over Lake Geneva; February 2012

In February 2012, most of Western Europe experienced an extreme cold and dry period as arctic air enveloped the region. This unusually cold, dry air over the relatively warm Lake Geneva produced organized fog streaks and a rare opportunity for natural flow visualization of large, coherent structures in the atmosphere (see Figure A.13A). This event inspired my collaborators, Marc Calaf and Marcus Hultmark, to mount the Doppler lidars (Figures A.13C and D) at Plage Pelican on the shore of Lake Geneva (Figure A.13B) to investigate these coherent structures. In short, proper orthogonal decomposition (POD) and spectral analysis revealed the presence of these structures and their ability to transport water aerosol (see full citation for this work in Section A.3.6 number 4: Calaf et al. [2013]).

A.3.3 Alpine Hydrometeorology and Coherent Structures Experiment; Summer 2012

This field experiment was inspired by the observed water aerosol transport by coherent structures over Lake Geneva (see Appendix A.3.2), in collaboration with Marc Calaf. The main objective of this field experiment was to measure scalar (water vapor and temperature) transport via large coherent structures in an alpine valley. The experiment site was located in a relatively flat and straight portion of the Val Ferret catchment. The setup consisted of two stations each with 2 sonic anemometers and an open-path H_2O/CO_2 gas analyzer (set

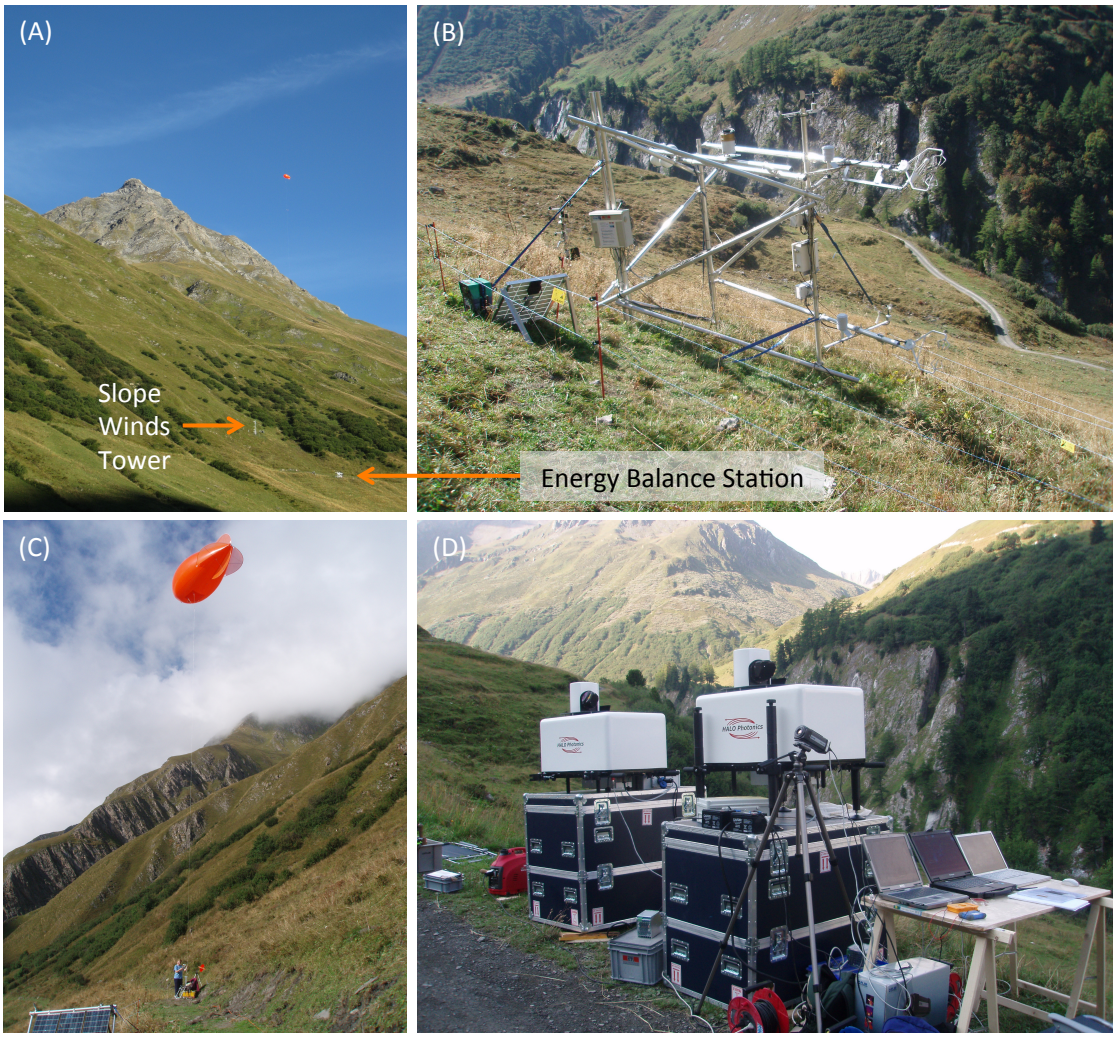

Figure A.12 – Summer 2011 alpine meteorology experiment setup showing (A) the station locations (B) the energy balance station, (C) the thither-sonde and balloon and (D) the Doppler lidars, which were positioned ≈ 100 m downslope of the two meteorological stations.

Figure A.13 – Organized fog streaks over lake geneva (A) during a cold snap event in February 2012, (B) coherent structures over Lake Geneva field experiment site, (C) Dopper lidar setup and (D) approximate lidar field of view.

up near the lower sonic anemometers on each station for eddy-covariance measurements). A Doppler wind lidar was mounted upvalley from the two stations, and the three were aligned such that the lidar measurement path passed through the lower sonic anemometer on each station (see Figure A.14). The evapotranspiration measurements from this field experiment were also used in a water balance investigation aimed at understanding the various controls on diurnal streamflow patterns in the watershed (see full citation for this work in Section A.3.6 number 2: Mutzner et al. [2015 *in review*]).

A.3.4 Alpine Meteorology Over a high-alpine Glacier; Winter 2013

The wintertime 2013 experiment site was located on Glacier Plaine Morte, a large, relatively flat, high-alpine glacier above Crans-Montana, Switzerland (see Figure A.15). This experiment was designed to incorporate measurements of turbulent exchanges above the snow, profiles of air pressure inside the snowpack and high-speed thermal imaging (the camera field of view included the lower station sonic anemometer, and the pressure poles and the upstream far field). Collaborators included Andreas Christen, Hendrik Huwald and Marc Diebold. The scientific objectives were to investigate pressure perturbations into the snowpack by turbulent motions from above, and how large-scale coherent structures affect snow surface temperature. Preliminary results of the rapid snow temperature response to winds across the galcier were presented at the American Geophysical Union fall meeting in December 2013 by Andreas Christen.

A.3.5 Steep Alpine Slope Flows, Part II; Summer 2013

The summer 2013 Val Ferret, Switzerland slope flow experiment returned to the site of the 2011 experiment. This work was done in collaboration with Andreas Christen. The objectives were to measure velocity and temperature with increased spatially resolution to examine more thoroughly the near-surface gradients (see Figure A.16B), and to use high-speed thermal imaging to investigate how relatively high-frequency surface temperature fluctuations affect turbulent exchanges in slope flows.

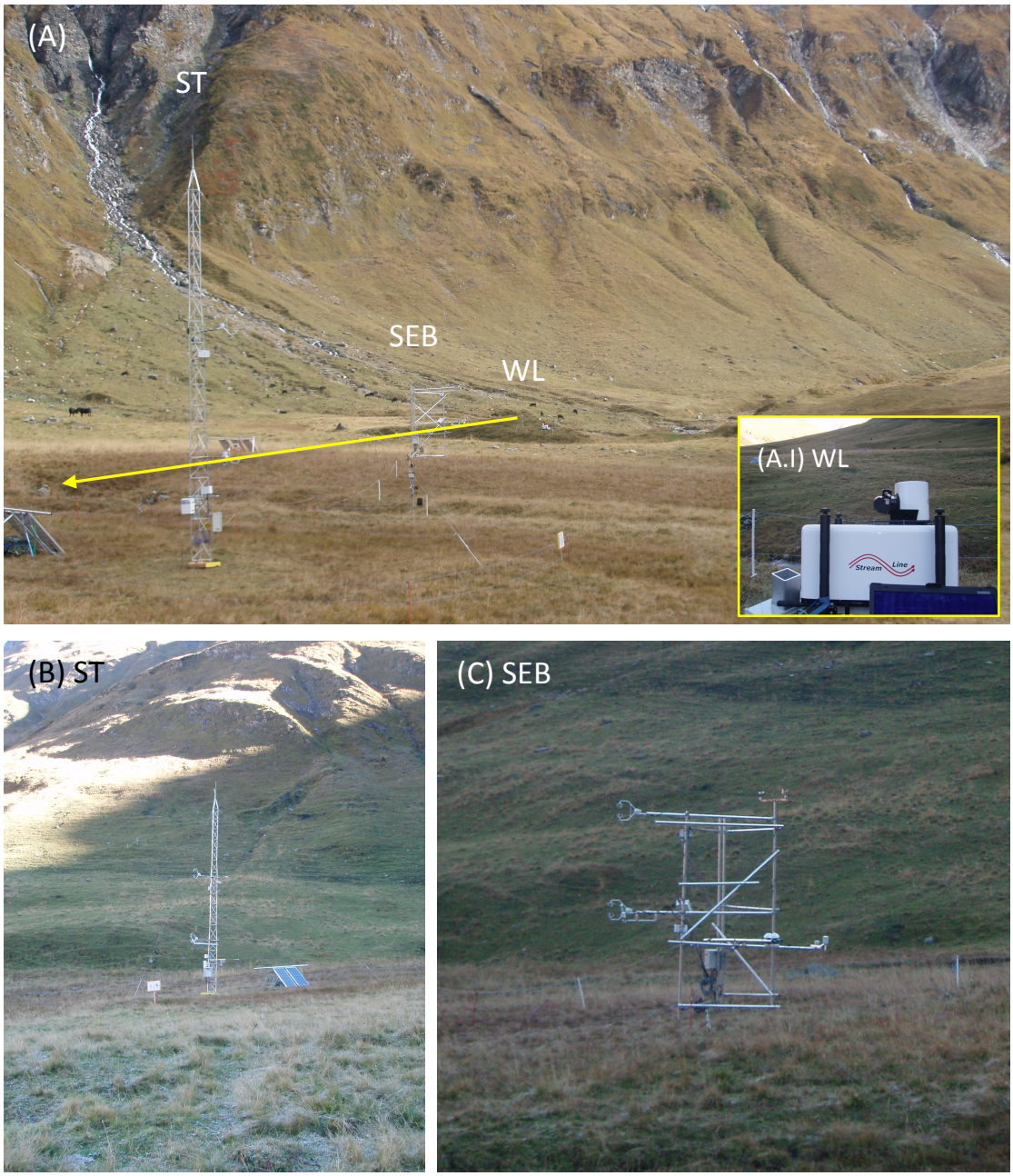

Figure A.14 – Summer 2012 alpine hydrometeorology and coherent structures field experiment setup showing (A) the lidar (WL) measurement path was aimed such that it passes inside the measurement paths of the lower sonic anemometers on both meteorological stations. The separation distance between the tower station (B ST) and the energy balance station (C SEB) is ≈ 80 m.

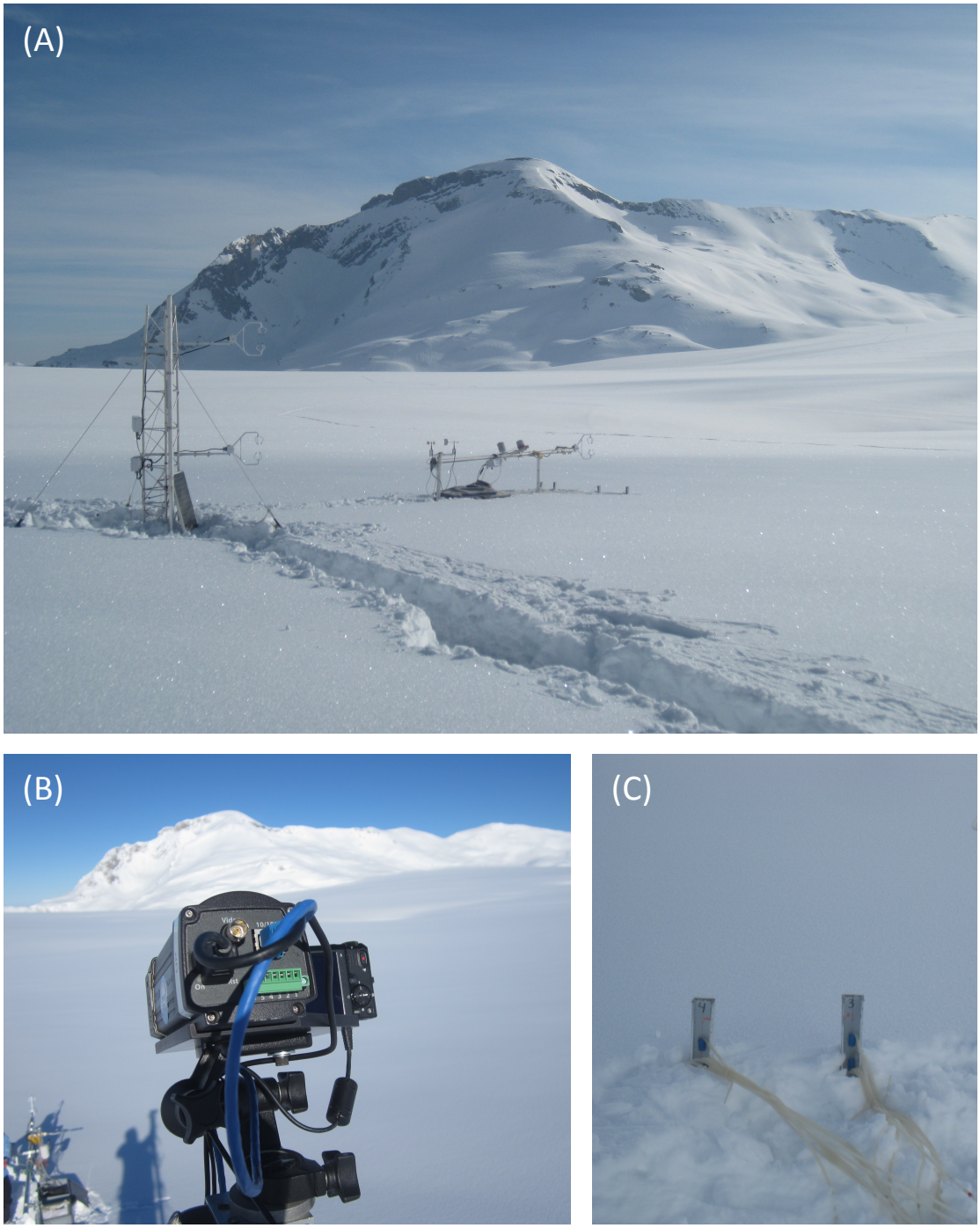

Figure A.15 – The Glacier Plaine Morte 2013 experiment (A) station setup, including (B) a high-speed thermal imaging system mounted above the tall tower (on a telescoping pole) and (C) pressure profiling probes installed in the snow.

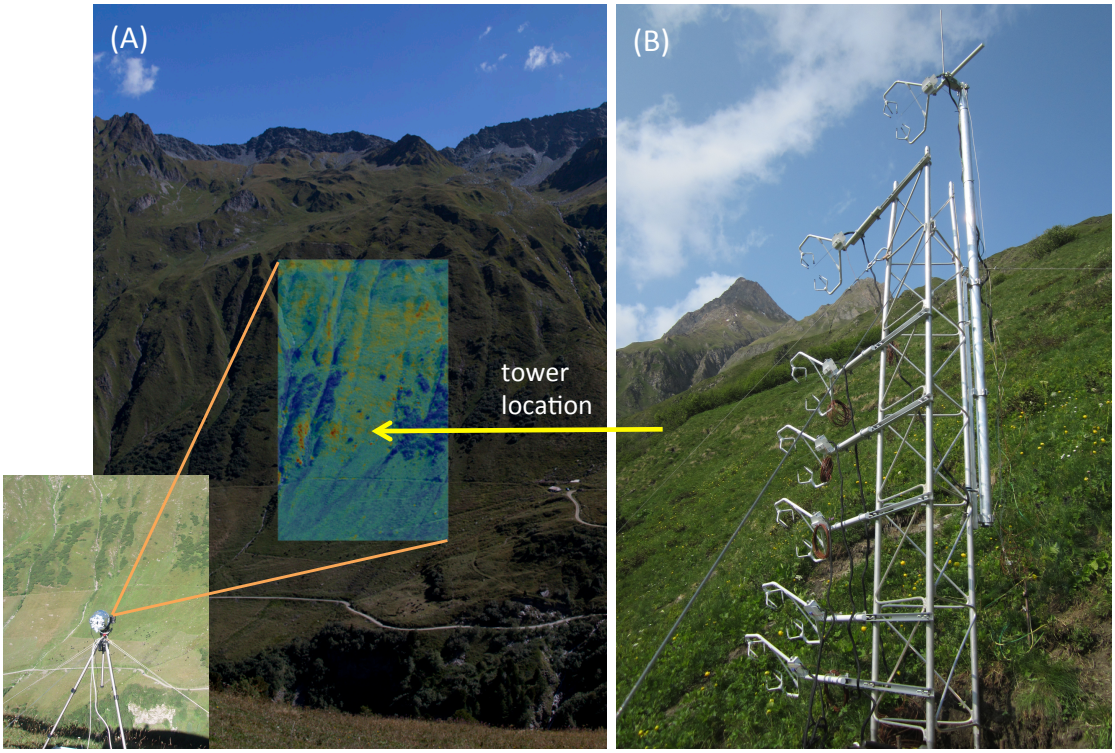

Figure A.16 – Summer 2013 steep alpine slope flow experiment setup showing (A) the infrared thermal camera, which was set up on the opposite side of the valley to capture a large portion of the slope with minimal pixel distortion, and (B) the flux measurement tower, which was configured to measure with high spatial resolution near the surface.

A.3.6 Publication List

1. H J Oldroyd, E R Pardyjak, H Huwald and M B Parlange. Adapting tilt corrections and the governing flow equations for steep, fully three-dimensional, mountainous terrain. Boundary-Layer Meteorology, 2015 *in review*.

2. R Mutzner, M Calaf, P Tarolli, H J Oldroyd, S V Weijs and M B Parlange. Controls on the diurnal streamflow cycles in a small alpine headwater catchment. Water Resources Research, 2015 *accepted*.

3. H J Oldroyd, G Katul, E R Pardyjak, and M B Parlange. Momentum balance of katabatic flow on steep slopes covered with short vegetation. Geophysical Research Letters, 41(13):4761–4768, 2014.

4. M Calaf, M Hultmark, H J Oldroyd, V Simeonov and M B Parlange. Coherent structures and the k-1 spectral behaviour. Physics of Fluids (1994-present), 25(12):125107, 2013.

5. H J Oldroyd, C W Higgins, H Huwald, J S Selker and M B Parlange. Thermal diffusivity of seasonal snow determined from temperature profiles. Advances in Water Resources, 55:121–130, May 2012.

A.3.7 Manuscripts in Preparation

1. H J Oldroyd, E R Pardyjak, C W Higgins and M B Parlange. Buoyant turbulence kinetic energy (TKE) production in steep-slope katabatic flow, 2015 *in preparation*.

2. H J Oldroyd, E R Pardyjak, C W Higgins and M B Parlange. Turbulence in katabatic flow in comparison to mechanically forced downslope flow, 2015 *in preparation*.

3. H J Oldroyd, E R Pardyjak, C W Higgins and M B Parlange. Advancing similarity theory for steep-slope katabatic flow, 2015 *in preparation*.

Holly Jayne Oldroyd

Ave. Du 24 Janvier 36, 1020 Renens, Switzerland
+41 077 449 31 45 / holly.oldroyd@epfl.ch
Birth Date: 29 December 1979, Salt Lake City, Utah USA
Citizenship: United States of America
Languages: English (mother tongue); French (basic conversational)

Education

PhD Civil and Environmental Engineering **2010-2015**
École Polytechnique Fédérale de Lausanne (EPFL), Lausanne Switzerland
Laboratory of Environmental Fluid Mechanics and Hydrology, *Supervisor:* Marc B. Parlange
Dissertation: Turbulent Transport in Complex, Alpine Environments

Master of Science in Mechanical Engineering **2006-2010**
University of Utah, Salt Lake City, Utah USA
Environmental Fluid Dynamics Laboratory, *Supervisor:* Eric R. Pardyjak
Thesis: Scalar Flux Measurements in Turbulent Pipe Flow Employing Combined Particle Image Velocimetry and Planar Laser Induced Fluorescence

Bachelor of Science in Mechanical Engineering **2001-2006**
University of Utah, Salt Lake City, Utah USA
Passed: *Fundamentals of Engineering Exam*

Associate of Science **1998-1999**
Colorado Northwestern, Rangely, Colorado USA
Athletic Scholarships: Softball and Basketball
Academic Scholarship: Presidential

Research Experience

Doctoral Candidate **2010-2015**
École Polytechnique Fédérale de Lausanne (EPFL), Lausanne Switzerland
School of Architecture, Civil and Environmental Engineering; *Supervisor:* Marc B. Parlange

- Designed and conducted several summer and winter field experiments to investigate atmospheric boundary layer flows and turbulent exchange over mountainous terrain with application to micrometeorology, hydrology and snow science.
- Developed methodologies to adapt standard field data handling techniques for fully three-dimensional terrain to improve turbulent flux estimates.

Graduate Research Assistant **2006-2010**
University of Utah, Salt Lake City, Utah, USA
Department of Mechanical Engineering; *Supervisor:* Eric R. Pardyjak

- Designed and conducted laboratory experiments to measure scalar fluxes in turbulent pipe flow to be used by researchers at Los Alamos National Laboratory for model development.

Independent Study Research Project **2005-2006**
University of Utah, Salt Lake City, Utah, USA
Department of Mechanical Engineering; *Supervisor:* Eric R. Pardyjak

- Designed and conducted a small-scale field experiment to measure pore pressure during compression in a highly-compressible, porous medium (Utah powder snow) to explore the possibilities of using fluid mechanics principles to improve ski design.

Undergraduate Research Assistant **2004-2006**
University of Utah, Salt Lake City, Utah, USA
Department of Mechanical Engineering; *Supervisor:* Eric R. Pardyjak

- Designed and developed graphical user interfaces (GUIs) for the Quick Urban Industrial Complex (QUIC-URB) and dispersion (QUIC-Plume) modeling projects.

Teaching Experience

École Polytechnique Fédérale de Lausanne (EPFL)

- Teaching Assistant: Introduction to Atmospheric Science, spring 2014: teach problem sessions and additional concepts.
- Teaching Assistant: Introduction to Fluid Mechanics, spring 2011 grading; spring 2012 teach problem sessions, develop exam questions; spring 2013 teach problem sessions, develop exam questions, maintain grades, design and implement a new laboratory component for the course.
- Co-advisor MS student project, 2011 mentor and advise: for coding, data analysis and writing.

University of Utah—Laboratory teaching Assistant

- Introduction to Fluid Mechanics, autumn 2006, 2008, Lecture for Labs, grade reports, help students with writing, proctor lab experiments and exams.
- Introduction to Heat Transfer, spring 2007, 2009, Lecture for Labs, grade reports, help students with writing, proctor lab experiments and exams.

Research Interests

- Fundamental, applied and environmental fluid mechanics and turbulence: Specifically applied to mountain hydrometeorology, micrometeorology and eco-hydrology, to improve environmental quality, resource management and numerical forecasts.
- Interdisciplinary research on complex environmental and sustainability projects that incorporate socioeconomic relevance and public policy outcomes.
- Future research aims to bridge the interface between complex mechanical/turbulent transport mechanisms and vegetation: i.e., physio-eco-hydrology.
- Additional topics of interest include applying my expertise to investigating greenhouse gas exchange, polar region research and urban hydrometeorology.

Honors and Awards

- Class of 2006 Cum Laude
- Tau Beta Pi (Engineering honor society)
- Pi Tau Sigma (Mechanical Engineering honor society)
- Phi Kappa Phi (National honor society)

Professional Affiliations

- American Meteorological Society (AMS)
- European Geosciences Union (EGU)
- American Geophysical Union (AGU)
- Complex Terrain Working Group: (co-founder and co-facilitator). Founded in July 2014 at the BLT conference in Leeds, UK to increase communication and collaboration (best practices, exemplary data sets, instrumentation, etc.) and facilitate more rapid advancement in the research field of atmospheric flows in complex environments.

Service

University of Utah:

- Engineering outreach. Fall 2006, Spring 2007.
- Undergraduate Supervisory Committee (USAC) Vice President. Fall 2005, Spring 2006.
- Engineering Day—Elementary school outreach and activities. Fall 2005.

Community:

- Science for Second graders. Spring 2009.
- Freelance, complimentary tutoring: math, engineering, physics, writing.

Summer Schools and Workshops

Unsteady Simulations for Industrial Flows: LES, DES, hybrid LES/RANS and URANS, Taught by Lars Davidson, Division of Fluid Dynamics, Department of Applied Mechanics, Chalmers University of Technology, Göteborg, Sweden, March 6-8, 2013.